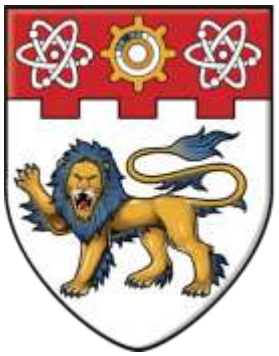

NANYANG TECHNOLOGICAL UNIVERSITY

GNSS IONOSPHERIC SCINTILLATION STUDIES IN SINGAPORE

DHIMAS SENTANU MURTI

SCHOOL OF ELECTRICAL AND ELECTRONIC ENGINEERING

2015

GNSS IONOSPHERIC SCINTILLATION STUDIES IN SINGAPORE

DHIMAS SENTANU MURTI

SCHOOL OF ELECTRICAL AND ELECTRONIC ENGINEERING

A thesis submitted to the Nanyang Technological University

in partial fulfillment of the requirement for the degree of

Master of Engineering

2015

Acknowledgment

First, I would like to thank my supervisor, Assoc. Prof. Tan Eng Leong for his guidance throughout my M. Eng candidature. His valuable advice and suggestions have contributed towards the success of this thesis.

Next, I would like to thank my team mate Dr. Heh Ding Yu for his help and guidance throughout this work.

I would like to thank the faculty and laboratory staffs at the School of Electrical and Electronic Engineering for their support and assistance. I would also like to thank Nanyang Technological University (NTU) for all the research facilities and DSO National Laboratories, Singapore for the research grant.

Table of Content

Summary

Ionospheric scintillation has been a challenge for Global Navigation Satellites System (GNSS) application especially in equatorial region. Ionosphere in around equatorial region is known to have unique characteristic. The existence of horizontal geomagnetic field and eastward electric field in this region caused equatorial ionosphere anomaly (EIA) effect, which subsequently inflicts high ionospheric activity. Singapore is located around equatorial region, which makes it an interesting place to perform research about ionospheric scintillation. Moreover year 2012-2014 is the year of high solar activity which implies higher ionosphere activity. Being susceptible to such adverse effects, GNSS which is free and continuously available can be used as ionospheric scintillation monitoring tool.

This thesis presents the analysis and studies of ionospheric scintillation in Singapore. Monthly S4 mean obtained from Global Positioning System (GPS) signal during year 2013 is presented. This analysis shows that high ionospheric scintillation happens during equinox months which are around April and September. This behavior is attributed to the close alignment of the solar terminator with magnetic meridian. Ionospheric scintillation happens mostly at night between 8pm to 12am. This is due to plasma bubble irregularities caused by $\boldsymbol{E}$ x $\boldsymbol{B}$ vertical force. $\boldsymbol{E}$ is earth electric filed and $\boldsymbol{B}$ is magnetic field.

Selected GPS scintillation events during the equinox months are presented by various scintillation parameters. Increased value of S4 (amplitude scintillation), phi60 (phase scintillation), and ROTI (rate of change of total electron content index) are shown to occur concurrently. This indicates that both signal intensity and the carrier phase of the GPS signal exhibit fluctuations while propagating through the plasma bubble irregularities of the ionosphere layer during this period. Sunspot number and solar flux are also analyzed as indicators of solar activity. Results show that in long term, during years 2009-2013, high solar activity is a factor that increases ionospheric scintillation possibility. Geomagnetic disturbance is also observed which shows that ionospheric scintillation is inhibited during geomagnetic disturbed days.

Next, the correlations of various ionospheric scintillation parameters between receivers at S2, S2.1, and Nanyang House building in Nanyang Technological

University (NTU) are calculated. These three receivers are separated by furthest distance of 1 km of each other. The correlation coefficients obtained are found to be nearly one which means that the bubble irregularities do not have significant difference in one km distance. Then, cross correlation of signal intensity between those locations are calculated to show that plasma irregularities drift toward eastward direction. Spatial distribution of scintillation is presented by sky plot which shows that scintillations are more concentrated in the south part of Singapore where the peak of Equatorial Ionization Anomaly (EIA) is located. The study of the effect of scintillation on positioning accuracy is also done. The pseudorange fluctuation is found to be proportional to S4 and phi60.

Next, ionospheric scintillation analysis using GLONASS and BeiDou which are the satellite navigation system owned by Russia and China respectively are presented as comparison. They show consistent results as those obtained by GPS with exception on the phi60 by GLONASS and total electron content (TEC) by both GLONASS and BeiDou. The former is caused by higher phase noise of GLONASS and the latter is caused by wrong TEC bias estimation performed by receiver. Analysis on L2 frequency is also presented here. Some comparison and relationship between L1 and L2 scintillation parameters are done.

For closer analysis, raw GPS signal is collected using event driven method. To effectively obtain useful raw signal, the system will record the raw signal only when high S4 detected. Matlab program is used to process the raw signal to obtain scintillation related parameters such as signal intensity, carrier to noise ratio (C/N_0), and S4.

List of Abbreviations and Symbols

Abbreviations

ADC	analog to digital converter
C/A	Coarse/Acquisition
C/N_0	carrier to noise ratio
DLL	delay locked loop
GLONASS	Globalnaya Navigazionnaya Sputnikovaya Sistema
GNSS	Global Navigation Satellites System
GPS	Global Positioning System
IGS	International GNSS Service
IMF	interplanetary magnetic field
LPF	low-pass filter
LT	local time
NBK	narrow band power
NH	Nanyang House building
NTU	Nanyang Technological University
PLL	phase locked loop
PRE	prereversal enhancement
PRN	pseudorandom noise
ROT	rate of change of total electron content
ROTI	rate of change of total electron content index
SBAS	satellite-based augmentation system
SDCCD	standard deviation of code over carrier divergence
SI	signal intensity
SSN	sunspot number
sTEC	slant total electron content

TEC	total electron content
TOW	time of week
UT	universal time
vTEC	vertical total electron content
WBK	wide band power

Symbols

S4	amplitude scintillation
Phi60	sigma phi at 60 s interval, denoting phase scintillation
E	electric field
B	magnetic field
σ_{ϕ}	sigma phi, denoting phase scintillation
I_n, Q_n	GPS tracking correlator output
I_E, I_P, I_L	early, prompt, and late tracking correlator output
∇_p	ionosphere plasma pressure gradient
g	gravity force

List of Figures

List of Tables

1. Introduction

1.1. Motivation

Communications between satellites and ground stations are becoming more important nowadays. Particular widely used application is positioning and navigation using Global Navigation Satellites System (GNSS) which includes GPS, GLONASS, Galileo, and BeiDou. As the mobile computer technology grows rapidly, GNSS positioning function cannot be separated from daily life. It is also a critical tool for military purposes.

One of the unresolved challenges that has been affecting GNSS application is ionospheric scintillation. It has been a challenge for researchers around the world to study and minimize its effect. By studying this ionospheric scintillation in Singapore its adverse effect on GNSS application and satellites to earth communication in general will be understood better.

Ionosphere in around equatorial region is known to have unique characteristic. The existence of horizontal geomagnetic field and eastward electric field in this region caused equatorial ionosphere anomaly (EIA) effect, which subsequently inflicts high ionospheric activity. Singapore is located around equatorial region, which makes it an interesting place to do research about ionospheric scintillation. Moreover year 2012-2014 is the year of high solar activity which implies higher ionosphere activity.

1.2. Objectives

By doing this research the characteristic of ionospheric scintillation in Singapore are expected to be studied. The ionospheric scintillation phenomena will be thoroughly analyzed along with its correlation with variation of temporal, seasonal, and spatial factor. Its correlation with sun activity and geomagnetic storm will also be studied. Subsequently, the effect of ionospheric scintillation on GNSS positioning will be investigated. The utilization of several GNSS constellations including GPS, GLONASS, and BeiDou as well as the new frequency GPS L2 will be done. The studies will be focused on the high solar activity period around year 2012 to 2014.

1.3. Major Contribution of the Thesis

This thesis has achieved several contributions summarized as follows.

The studies on ionosphere scintillation behavior have been done using GNSS in Singapore. These studies complement the previous studies about equatorial ionosphere scintillation that have been done in several other locations worldwide. To the best knowledge of the author, this work is also the first thorough ionospheric scintillation research done in Singapore. This work also involves the utilization of BeiDou and GPS second frequency L2c which are also relatively new means for such study.

This thesis provides thorough information about the behavior of ionospheric scintillation in Singapore which includes the temporal and seasonal pattern, spatial correlation, and the effect natural phenomena such as solar activity and geomagnetic storm. The effect of such scintillation into satellite availability and positioning accuracy are also provided. By using this information, many kinds of satellite to earth communications in Singapore can be utilized more wisely to avoid the adverse effects.

This work is a starting point for future work on GNSS receiver design that is robust to ionospheric scintillation in Singapore. It can be extended to support certain applications that need high accuracy and reliability such as airplane and unmanned aerial vehicle (UAV) navigation especially during taking off and landing. This can also be combined with other work on other challenges such as multipath mitigation in urban area.

1.4. Organization of the Thesis

Chapter 1 of this thesis gives the introduction of this work. The motivation and objectives of this research are presented here. The major contributions given by this thesis are also presented.

Chapter 2 shows the overview of literature survey done on various areas related to the ionospheric scintillation studies. The ionosphere layer and how scintillation happens are explained here. The ionosphere condition in Singapore is also presented. Some background about Global Navigation Satellite System (GNSS) as the mean of scintillation monitoring and also some parameters that can be obtained are presented.

Chapter 3 presents the main results of the ionospheric scintillation analysis using GPS in Singapore. The temporal, seasonal, and spatial variations of scintillation in Singapore are presented here. The effect of solar activity and geomagnetic storm is also discussed. Lastly, the effect of such scintillation to GPS positioning is shown.

Chapter 4 presents the ionospheric scintillation analysis obtained by GLONASS and BeiDou. Its comparison with GPS work in previous chapter is provided. This chapter also shows the use L2 frequency signal and its relationship with L1 frequency.

Chapter 5 presents the event triggered data collection method to record raw baseband GPS signal. The processing of the raw signal using software defined GPS receiver into meaningful scintillation parameter is then discussed.

Chapter 6 gives the overall conclusion of this thesis and also the possible future research based on this work.

2. Literature Survey

2.1. Ionospheric Scintillation

Ionosphere is ionized atmosphere layers located between altitudes 50 km to 500 km approximately, which can vary depending on the longitude and latitude. It is a region of the upper atmosphere where charged particles occur because of sun radiation. Ionosphere consists of 3 layers with approximate height as follows [1]:

- D-layer (60 km – 90 km)
    - High recombination, low ionization
    - High absorption of radio waves lower than ~10 MHz
- E-layer (90 km – 120km)
    - Reflective to frequency radio waves lower than ~10 MHz
    - Absorption in frequency higher than ~10 MHz
- F-layer (120 km – 500 km)
    - High ionization and electron density
    - Facilitates sky wave propagation of radio waves over long distance due to its reflective property to frequency lower than < ~30 MHz
    - Main source of ionospheric scintillation on global navigation satellite system which lay on frequency ~1.1 – 1.7 GHz

This ionized atmosphere layers gives some effects to radio waves passing through it. It changes the signal velocity, group delay, refraction, amplitude variations, and phase variations. These effects are functions of carrier frequency, solar activity, magnetic latitude, time variations, and elevation and azimuth of the satellite [2], [3].

Ionosphere scintillation is electron density fluctuation within the ionosphere that causes random fluctuation of radio waves in amplitude and phase. Random refraction and diffraction happen in the ionosphere because of the electron density fluctuation. It is most common in equatorial and polar regions. Global Navigation Satellite System (GNSS) is susceptible to the effects of such scintillation.

Figure 2-1 which is taken from [2] depicts the effects of ionosphere on communication. Ionosphere causes code delay, carrier advance, and Faraday rotation on the radio wave between satellite and earth. Besides that, amplitude and phase

variation will also occur when scintillation happens. Ionosphere layer also reflects the radio wave between transmitter and receiver station on earth.

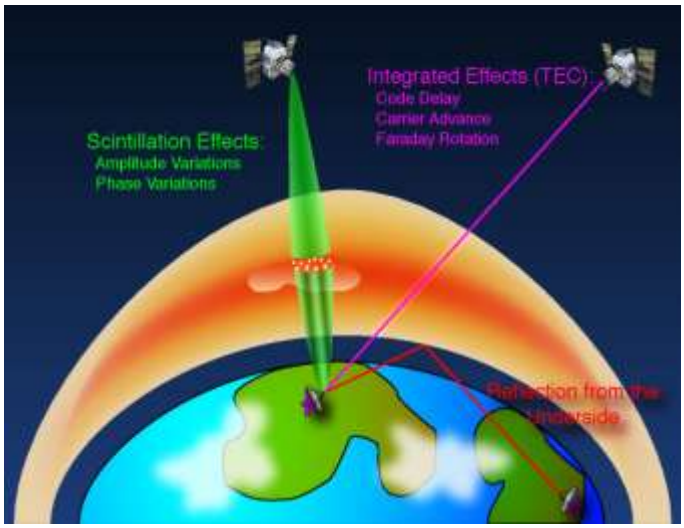

Figure 2-1 Ionosphere effects on communication

Ionospheric scintillation is initiated by ionosphere instability. The instability is driven by gravitational Rayleigh–Taylor (GRT) mechanism which is characterized by a situation similar to a heavy fluid resting on a light fluid. Figure 2-2 which is adapted from [4] shows schematic diagram of the Rayleigh-Taylor instability and its effect. Recombination happens faster in lower layer because of gravity effect. Lower layer of ionosphere with lower density moves up and forms bubbles which are electron depleted region [2], [5].

At equatorial region ionospheric scintillations vary with latitudinal factor. Scintillations are minimum at the magnetic equator and are maximum at around 15^{o}-20^{o} north and south magnetic latitudes which are the peaks of the equatorial ionization anomaly (EIA). Scintillation lasts from sunset until shortly after midnight. It has strong seasonal dependence with April and September which is equinox period is typically the worst [2].

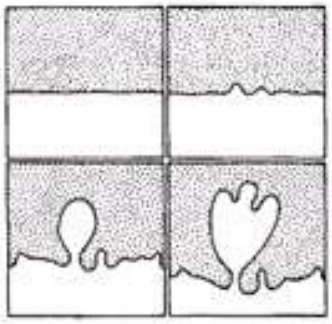

Figure 2-2 Sequential sketches of the Rayleigh–Taylor instability. A heavy fluid is initially supported by a transparent light fluid [4]

2.2. Equatorial Ionization Anomaly (EIA)

At day, zonal electric field exists at eastward direction caused by equatorial F-Region dynamo effect. Figure 2-3 shows the schematic diagram of the zonal electric field component and its relationship to the charge densities at the solar terminators [1].

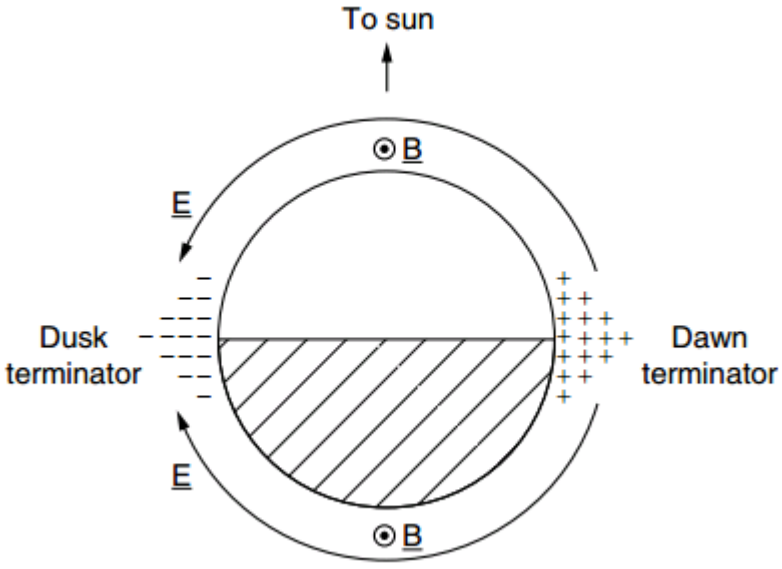

Figure 2-3 Zonal electric field component at day and night

Eastward electric field is coupled with geomagnetic field to produce ***E x B*** upward force shown in Figure 2-4 [1]. Under the upward force the F region plasma is lifted up to higher altitudes. The plasma in the higher altitude then diffuses under pressure

gradient (∇_p) and gravity force (g) to both sides of the magnetic equator leading to accumulation of large ionization densities at magnetic latitudes around 15^0 - 20^0 north and south. This mechanism results in latitudinal variation of ionization density distribution, characterized by the two ionization crests with a minimum centered at the magnetic equator which is known as the equatorial ionization anomaly (EIA) [5], [6].

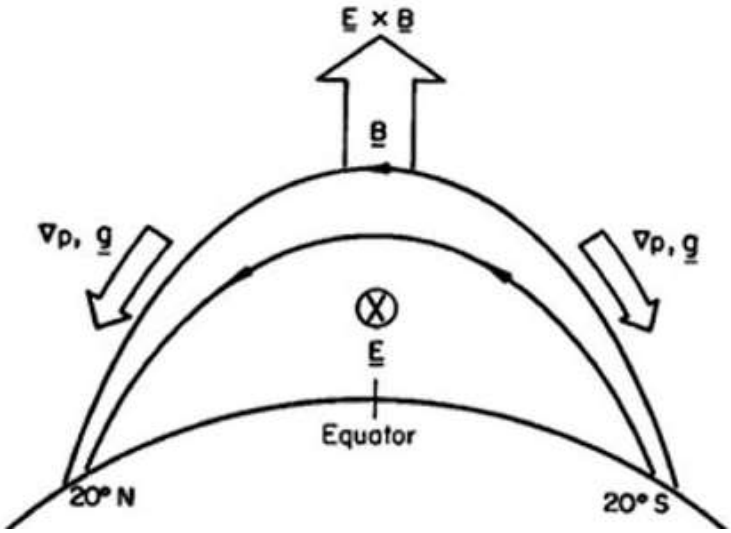

Figure 2-4 Electric Field and Magnetic Field of Earth at Equator

2.3. Global Navigation Satellite System

Global Navigation Satellite System (GNSS) involves constellations of satellites orbiting at about twenty thousand kilometers altitude over the earth surface. It is continuously transmitting signals that enable users to determine their three-dimensional position with global coverage [7]. GNSS consist of several satellite navigation systems:

- Global Positioning System (GPS) [8]
  - by USA
  - fully operational, 32 satellites available
- Global Orbiting Navigation Satellite System or Globalnaya Navigatsionnaya Sputnikovaya Sistema (GLONASS) [9] [10]
  - by Russia
  - fully operational, 24 satellites available

- Galileo [11]
  - by European Union
  - not fully operational, currently only 2 satellites available
  - 30 satellites are expected to be operational in 2019
- Compass or BeiDou [12] [13]
  - by China
  - not fully operational, only 12 satellites are available on 2012
  - 35 satellites are expected to be operational in 2020
- Satellite-based augmentation system (SBAS)
  - system that supports wide-area or regional augmentation through the use of additional satellite-broadcast messages

In this study GNSS especially GPS which are fully operational are mainly used as the source of ionospheric scintillation data. GPS will be studied more deeply about its signal structure and processing steps from raw baseband signal into ionospheric scintillation information. Many detailed information about GPS can be found in [14], [15], [16], [17], [18].

GPS uses code division multiple access (CDMA) to differentiate signals from many satellites which functions as ranging code as well. GPS signal consists of two ranging codes: the Coarse/Acquisition (C/A) code, which is freely available to the public, and the restricted Precision (P) code, which is reserved for military use. The C/A code is a 1023 bits sequence called pseudorandom noise (PRN code), transmitted at 1.023 Mbit/s.

The total length of P code is $2.35469592765 \times 10^{14}$ transmitted at 10.23 Mbit/s. Thus, if the P-code were allowed to continue without being reset, each P code would continue without repetition for slightly more than 38 weeks. In effect, this overall period has been subdivided so that each of 37 possible GPS satellites gets a 1-week period code, which is non-overlapping with that of any other satellite [14].

Detailed satellites' information is delivered to receiver by navigation message which is modulated on top of both the C/A and P(Y) ranging codes at 50 bit/s. The navigation message consists of three main components. The first part contains the GPS date and time, plus the satellite's status and an indication of its health. The second part contains ephemeris data providing the orbital information which allows the receiver to calculate the position of the satellite. The last part is the almanac, contains information and status concerning all the satellites, their rough locations and PRN numbers.

Ranging codes and navigation message are modulated onto a carrier frequency. At the initial launching of GPS two frequencies, L1 and L2 are used. L1 frequency is centered at 1575.42 MHz while L2 frequency is centered at 1227.60 MHz. The C/A code is transmitted on the L1 frequency as a 1.023 MHz signal using a bi-phase shift keying (BPSK) modulation technique. The P(Y)-code is transmitted on both the L1 and L2 frequencies as a 10.23 MHz signal using the same BPSK modulation in quadrature with the C/A. Currently GPS is undergoing modernization by adding L5 frequency. Figure 2-5 shows the modulation of GPS L1-C/A signal, obtained from [19].

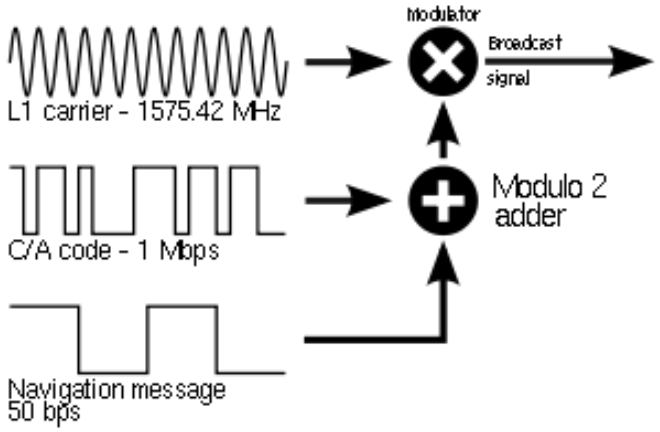

Figure 2-5 GPS L1-C/A broadcast signal

2.4. Ionospheric Scintillation Parameters

Several parameters are needed to quantify the ionospheric scintillation effect. Some parameters that can be obtained from GNSS receiver are S4 (amplitude scintillation), σ_{ϕ} or phi60 (phase scintillation), slant total electron content (sTEC), vertical total electron content (vTEC), ROT, and ROTI.

Amplitude scintillation is quantified by the S4 parameter which is defined as the square-root of the normalized variance of signal intensity over a given interval of time [20]. S4 higher than 0.2 is commonly used to indicate that amplitude ionospheric scintillation event is happening [21] [22][23]. This 0.2 threshold can be dependent on the receiver used. Based on our observation using PolaRxS receiver, 0.2 is suitable to differentiate between quiet situation and ionospheric scintillation events.

Figure 2-6 shows the typical S4 during scintillation day from all GPS satellites obtained by PolaRxS receiver with the threshold line. At around 13.00-16.00 GPS time, amplitude scintillation is detected as S4 exceeds 0.2.

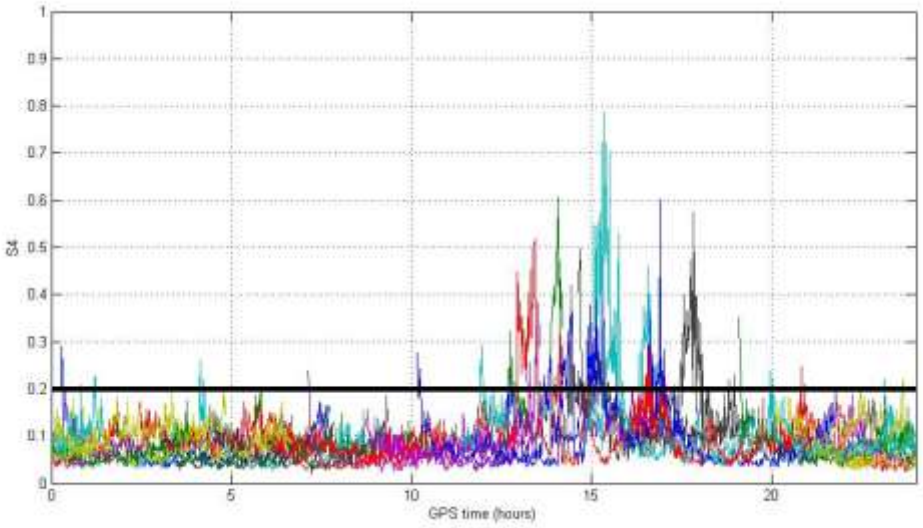

Figure 2-6 Typical one day GPS S4 obtained by PolaRxS receiver, and 0.2 threshold line in black color

$$S4 = \sqrt{\frac{\langle SI^2 \rangle - \langle SI \rangle^2}{\langle SI \rangle^2}} \qquad \textbf{(2.1)}$$

where SI is the signal intensity or power and $\langle . \rangle$ denotes the expected (or average) value over the interval of interest (60 seconds). S4 is commonly estimated over an interval of 60 seconds.

The S4 defined in (2.1) can have significant values simply due to ambient noise. Based on [20], assuming that the raw intensity data rate is 50 Hz and it has a single-sided noise bandwidth of 25 Hz, if the 60 second average of carrier-to-noise density ratio (C/N_0) is known, the predicted S4 due to ambient noise is

$$S4_{N_0} = \sqrt{\frac{100}{C/N_0}\left[1 + \frac{500}{19C/N_0}\right]} \qquad \textbf{(2.2)}$$

After removing the noise, the revised value of S4 is

$$S4 = \sqrt{\frac{\langle SI^2 \rangle - \langle SI \rangle^2}{\langle SI \rangle^2} - \frac{100}{C/N_0}\left[1 + \frac{500}{19C/N_0}\right]} \qquad \textbf{(2.3)}$$

Phase scintillation is usually quantified by the standard deviation of detrended carrier phase from signals received from satellites given by

$$\sigma_{\emptyset} = \sqrt{\langle d\emptyset \rangle - \langle d\emptyset \rangle^2} \qquad \textbf{(2.4)}$$

where $d\emptyset$ is the detrended carrier phase and $\langle . \rangle$ denotes the expected (or average) value over the interval of interest. Most people calculate σ_{ϕ} every interval of 60 seconds which makes it named phi60. In this work phi60 higher than 0.1 is used to indicate that phase scintillation is happening. Figure 2-7 the typical phi60 during scintillation day from all GPS satellites obtained by PolaRxS receiver with the threshold line. At around 13.00-16.00 GPS time, phase scintillation is detected as phi60 exceeds 0.1.

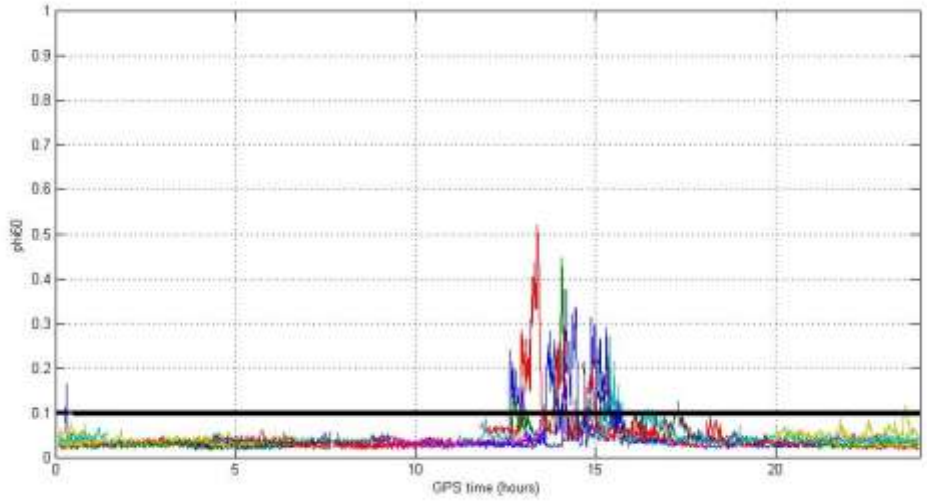

Figure 2-7 Typical one day GPS phi60 obtained by PolaRxS receiver, and 0.1 threshold line in black color

The purpose detrending is to separate scintillation from noise, multi-path and other impacts. The method used for detrending is passing the carrier phase through a high-pass filter, which removes all low frequency effects below its frequency cut-off. A sixth-order Butterworth high pass filter with 0.1-Hz cut off frequency has been used

for detrending of the 50-Hz phase outputs to remove the satellite-receiver dynamics and other slowly changing errors [20].

"sTEC" is the total electron content along the raypath between satellite and receiver. It can be converted to vTEC which is the vertical component of TEC at the ionosphere piercing point by using mapping function given by [24]. ROT is the TEC rate of change per minute. Reference [25] defines rate of TEC index (ROTI) based on the standard deviation of ROT as shown below

$$ROTI = \sqrt{\langle ROT^2 \rangle - \langle ROT \rangle^2} \qquad \textbf{(2.5)}$$

ROTI can be used to predict the presence of ionosphere irregularities. However, the quantitative relationship between ROTI and S4 varies due to variations of the ionospheric projection of the satellite velocity and the ionospheric irregularity drift [26].

2.5. Ionospheric Scintillations Studies by Global Navigation Satellite System (GNSS)

Several studies on ionospheric scintillation using GNSS especially GPS have been done by researches both in equatorial and high latitude regions. GPS provides free and continuously observable signal with wide coverage over the ionosphere. References [20] and [27] present the initial work on ionospheric scintillation monitoring using low cost, modified GPS receiver. High performance commercial GPS C/A code receiver for ionospheric scintillation parameter estimation is presented here. These modifications include high-speed processing of carrier phase and signal power measurements to obtain phase and amplitude scintillation parameters, and the addition of a high quality oven-controlled crystal oscillator (OCXO) as the receiver's frequency reference. Further developed ionosphere scintillation monitoring receivers: PolaRxS and GSV4004 are presented in [28] which include multi GNSS constellations and multi frequencies. Some work on software based GNSS receiver for scintillation studies is shown by [29] which enable us to have more flexible RF front end and fully digital signal processing.

Ionospheric scintillation phenomena vary with latitude, longitude, and time factor. Previous works using GNSS or GPS to study ionospheric scintillation in around equatorial region show that this signal perturbation is most prominent during night time after sunset. This is shown by the results in Chiang Rai and Bangkok, Thailand [30] [31], Bandung and Pontianak, Indonesia [32], Malaysia [21], Guilin [22], Brazil [28], and India [33]. Season or month in the year is also a factor that determines the occurrences of scintillation. Observations in India [33], Malaysia [21], Indonesia [32], Bangkok [31] show that during equinox months, around March, April, September, and October, scintillation happened most frequently. In Brazil, the highest ionospheric scintillation occurred during December [34].

In high latitude near polar region, ionospheric scintillation is affected more by magnetic activity rather than sun activity. Reference [35] and [36] reported that scintillation occurrence is higher during geomagnetic disturbed days than during quiet day. Also, the scintillation occurrence has a seasonal pattern, with peaks during summer and equinoctial months. A comparison with the interplanetary magnetic field (IMF) components B_y and B_z showed a strong association of scintillation occurrence with southward IMF B_z conditions. It is also shown that in high latitude region phase fluctuation is more likely to occur compared to amplitude scintillation [37].

3. Singapore Ionospheric Scintillation Analysis

3.1. Ionospheric Scintillation Monitoring Data Collection

Septentrio PolaRxS GNSS receiver is used for the main ionospheric scintillation data collection in this research. This receiver is able to work with multi frequency and multi satellites constellations in GNSS including GPS L1 and L2, GLONASS L1 and L2, Galileo, Compass or BeiDou, and SBAS. PolaRxS receiver tracks the available satellites constellations and logs the output data continuously. Various ionospheric scintillation parameters such as S4 and phi60 are provided every 60 seconds. In this work, GPS data are mainly used for the ionospheric scintillation analysis. Some comparison results using GLONASS and BeiDou are also presented.

Currently three Septentrio PolaRxS receivers are logging data at three locations in NTU campus: block S2, block S2.1, and Nanyang House building, shown in Figure 3-1. The first and second receivers are located nearby in south spine academic complex block S2 and S2.1 respectively. The distance between the two receivers is 80m. The first receiver has been logging data since April 2012 while the second receiver started in July 2013. The third receiver is located in Nanyang House which is around 1 km apart from the first receiver. It started logging data in December 2013. Data collected by the receiver in block S2 is mainly used in this thesis, while the data from block S2.1 and Nanyang House are added for comparison and spatial analysis.

Figure 3-1 Receivers locations in NTU

The receiver system shown in Figure 3-2 is located on the rooftop of block S2. It is designed to be operated remotely. High capacity hard disks are attached to the PC to save the continuously recorded data. The system is connected to internet to control it remotely. Whenever power failure happens, the emergency power supply and remote power control can maintain the operability of the system. Septentrio multi frequency GNSS antenna shown by Figure 3-3 is used to capture the RF signal.

All the information about ionospheric scintillation and GNSS navigation message are logged into septentrio binary format (SBF) file. The structure of such format is explained in the manual provided by Septentrio [38]. These logged files are then further processed to get more detailed ionospheric scintillation data mainly by sbf2ismr program [39].

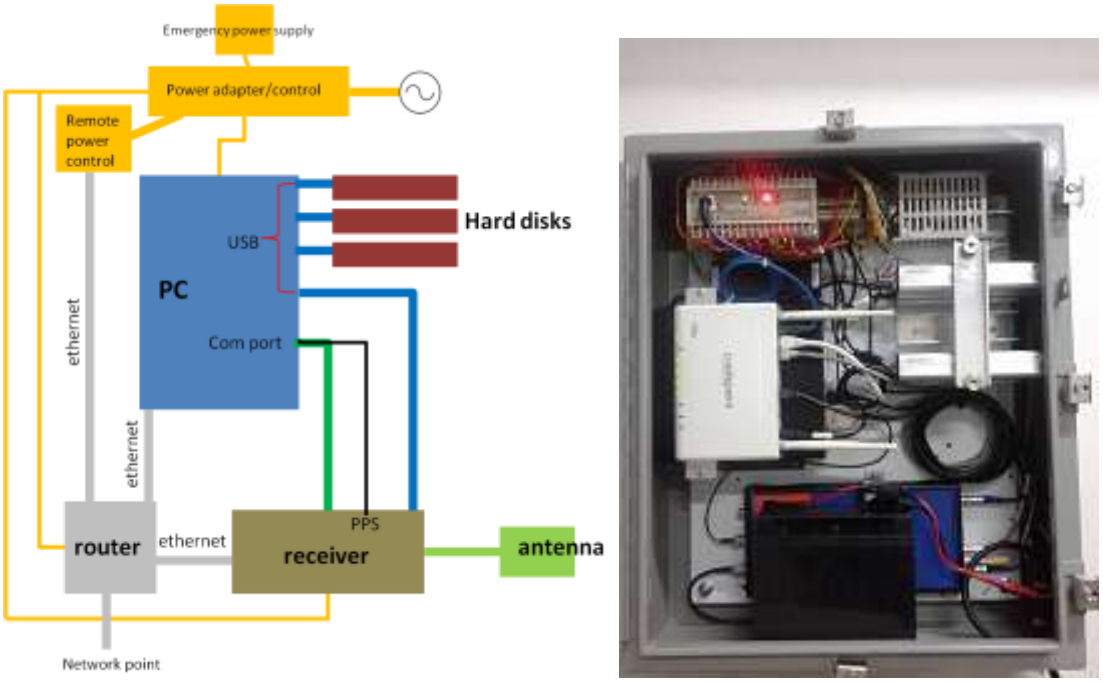

Figure 3-2 Ionospheric scintillation receiver configuration

Figure 3-3 Septentrio GNSS antenna

Besides the Septentrio receiver, we also use GNSS data provided by the International GNSS Service (IGS). IGS is a voluntary federation of more than 200 worldwide agencies that pool resources and permanent GPS & GLONASS station data. The IGS provides high quality data and products as the standard for Global Navigation Satellite Systems (GNSS) in support of earth science research, multidisciplinary applications, and education.

One IGS station named NTUS is available in Singapore which is located at NTU School of Civil and Environmental Engineering. In this station, LEICA GRX1200 GG PRO receiver is used. It provides data of GPS and GLONASS at L1 and L2 frequencies in RINEX format. Pseudorange, carrier phase, and signal to noise ratio are available every 30 seconds since year 1992 to present. This data can be processed to obtain S4 and TEC to support the observation provided by Septentrio receiver, especially for long term analysis.

Our receivers and IGS NTUS station cover wide area of ionosphere over Singapore. NTU is located at 1.34^0N 103.68^0E geographic coordinate. The magnetic coordinate is 8.46^0S 176.10^0E, which is obtained by a conversion tool provided in [40]. Collected data from GNSS are limited at minimum elevation angle = 20^0 to minimize multi path effect. To get the covered ionosphere region above Singapore the following mapping function based on thin layer model of ionosphere given by [24] is used.

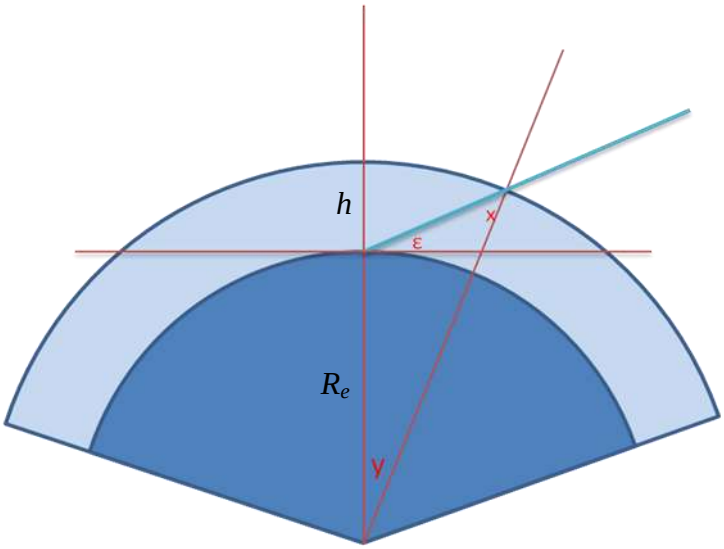

Figure 3-4 Thin layer model of ionosphere

$$\cos(x) = \left(1 - \left(\frac{R_e \cos \varepsilon}{R_e + h}\right)^2\right)^{0.5} \qquad (3.1)$$

where x, ε, and y are the angles shown in Figure 3-4. R_e is the earth radius which is 6371 km and h is ionospheric height estimation which is 400 km. $\varepsilon=20^0$ as the minimum elevation angle is used. By using (3.1) y which is the latitude different between receiver position and its maximum ionosphere coverage is calculated and obtained to be $y=7.85^0$.

Figure 3-5 shows the ionosphere region above Singapore covered by our receivers. It is shown by the blue shaded circle. This area is bounded by 9.15^0N latitude in the north and 6.55^0S in the south, both in geographic coordinate.

Figure 3-5 Ionosphere area covered by GNSS receiver in Singapore

Singapore is located in equatorial region. Therefore, the ionosphere over Singapore is under influence of EIA. Figure 3-6 shows the IRI-2012 latitudinal (magnetic coordinate) total electron content (TEC) model over Singapore taken in April 2013. It shows the TEC trough in the magnetic equator and two crests in the north and south of equator. Our receiver's latitude coverage is shown by the blue shaded area, which includes the trough and crest of EIA.

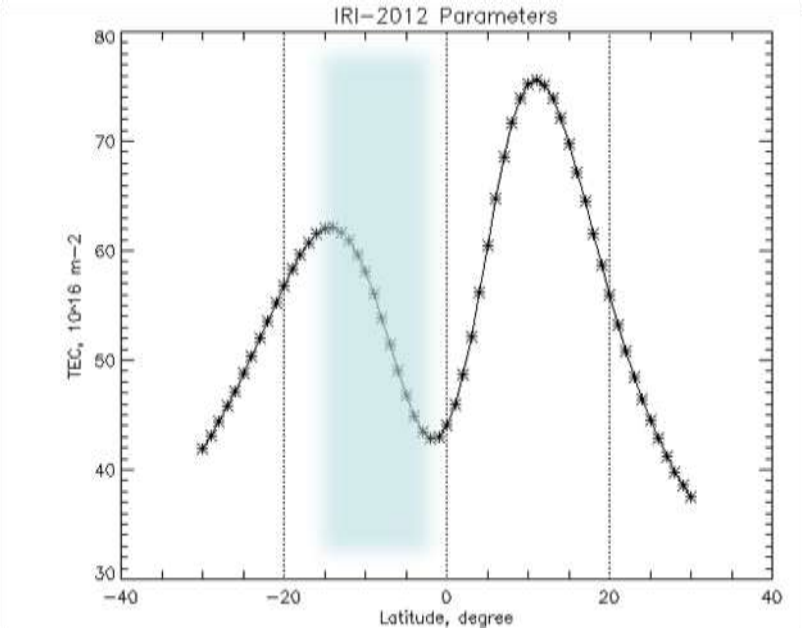

Figure 3-6 IRI-2012 TEC Model on April 2013 in Singapore

3.2. Monthly Ionospheric Scintillation Average

The monthly S4 average of GPS satellites obtained from receiver at block S2 are computed where the S4 is averaged over all visible GPS satellites in every minute. The visible satellites are only limited to those having elevation angle more than 20 degrees to filter out fluctuation due to multipath effects. Although Singapore has no seasons, the months are categorized into equinox, 'winter', and 'summer' months, following the earth northern hemisphere. The equinox months consist of March, April, September and October, 'winter' months consist of January, February, November and December and lastly, 'summer' months consist of May, June, July and August.

Figure 3-7 shows the monthly S4 average of visible GPS satellites during the equinox months of March, April, September and October 2013. The *y* and *x* axes for each subplot represent the day (1^{st} to 30^{th} or 31^{st}) and local time (8 a.m. to 8 a.m. next day) in each month. It can be observed that in equinox months, relatively high S4 average of larger than 0.2 is present in reasonably high number of days. This indicates high number of scintillation events during these months, which may be attributed to the close alignment of the solar terminator with magnetic meridian [41]. This result agrees with previous study done in India which was conducted in low latitude zone [42].

Diurnally, these scintillation events occur mostly around local time of 8 p.m. to 12 a.m, which is during the post sunset period. This is attributed to the eastward prereversal enhancement (PRE) electric field. PRE is the enhancement of the eastward electric filed that happen right after sunset due to atmosphere activity [1]. The enhanced eastward electric field is coupled with the earth's geomagnetic field to produce stronger upward vertical force derived from $\boldsymbol{E} \times \boldsymbol{B}$. The upward vertical force results in steep gradient of ion and electron densities between upper and lower layer, thereby producing plasma bubble irregularities arising from Rayleigh-Taylor instability process.

Figure 3-8 plots the monthly S4 average of visible GPS satellites during the 'winter' months of January, February, November and December 2013. The S4 average is relatively low in these months, indicating fewer scintillation events. Nevertheless, there exist certain days in which some day time scintillation events can be observed, occurring mostly before 6 p.m. Figure 3-9 plots the monthly S4 average of visible GPS

satellites during the ‘summer’ months of May, June, July and August 2013. These months are also relatively quiet with fewer scintillation events. Overall, the observations here are quite consistent with the observations derived from nearby countries around equatorial region such as Malaysia [21] and Indonesia [32].

Figure 3-10 and Figure 3-11 show the same plot for phi60 and ROTI respectively during equinox months of year 2013. They show the same pattern as the S4 which has high magnitude at night after sunset. This suggests that in Singapore S4, phi60, and ROTI generally happen concurrently, which differs with some observations done in high latitude region. In high latitude near polar region, phase fluctuation is more likely to occur compared to amplitude scintillation [35] [37]. This is caused by improper phase detrending process that was used on those high latitude ionospheric scintillation observations [43]. At high latitude, typical values of ionospheric irregularity drift are higher compared to those in equatorial region, especially during geomagnetic storm. This causes higher Fresnel frequency which requires higher detrending cut off frequency. Neglecting this factor will lead to overestimated phase scintillation which sometimes observed as phase scintillation without amplitude scintillation [43].

March

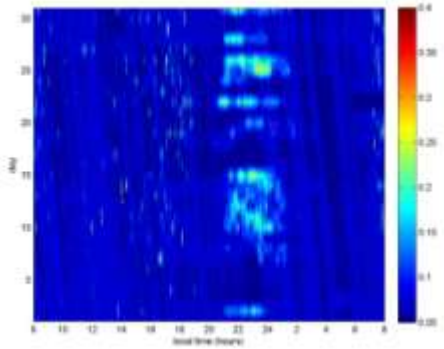

April

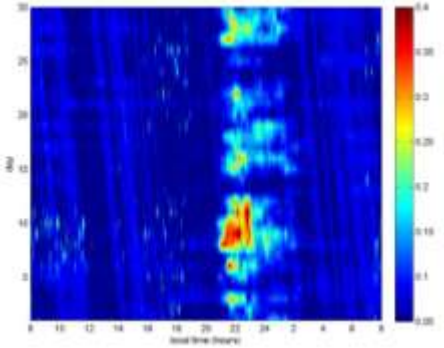

September

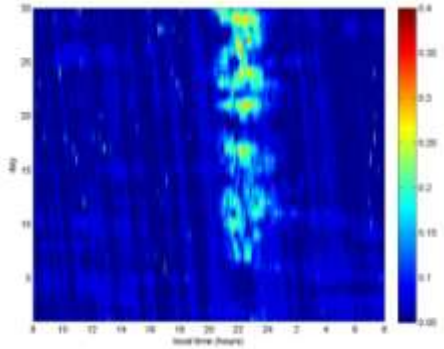

October

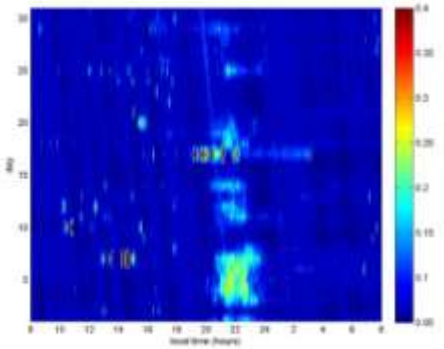

Figure 3-7 Monthly S4 average during equinox months of year 2013

January

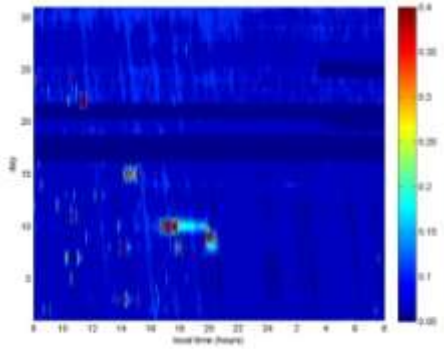

February

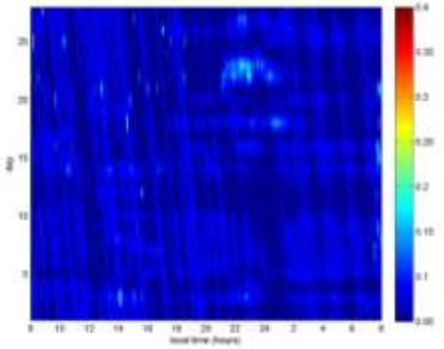

November

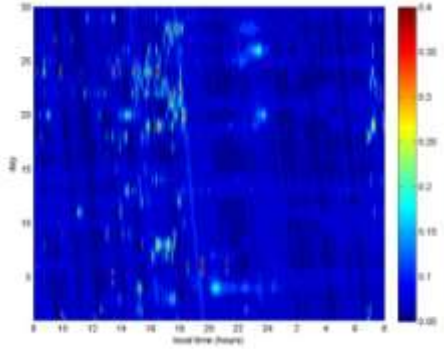

December

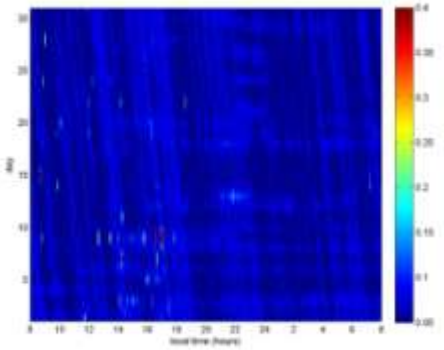

Figure 3-8 Monthly S4 average during winter months of year 2013

May

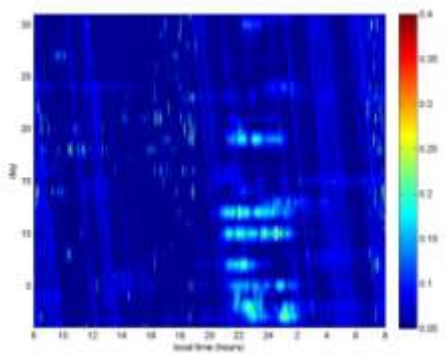

June

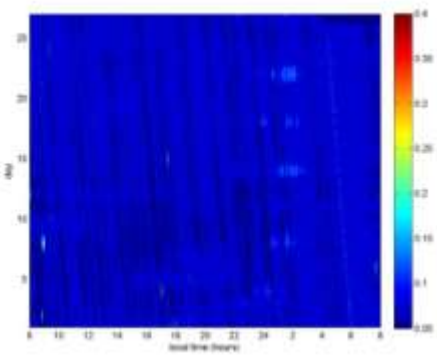

July

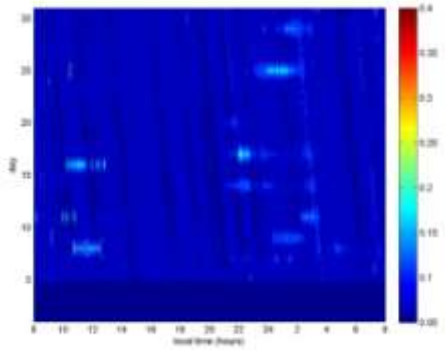

August

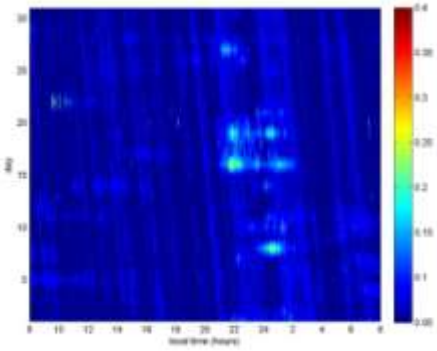

Figure 3-9 Monthly S4 average during summer months of year 2013

March

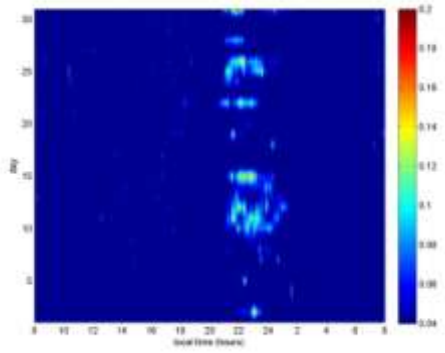

April

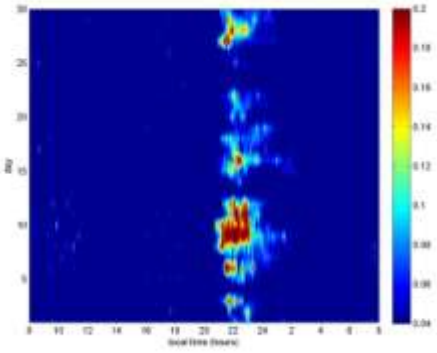

September

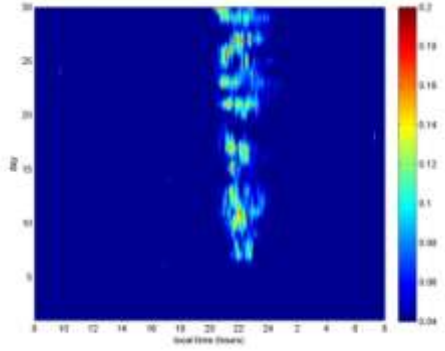

October

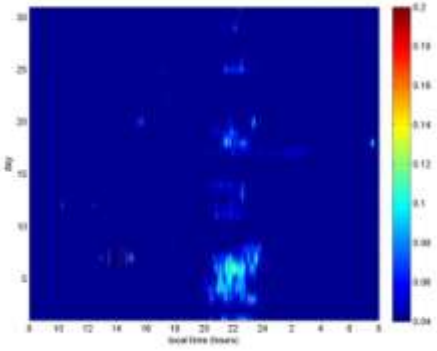

Figure 3-10 Monthly Phi60 average during equinox months of year 2013

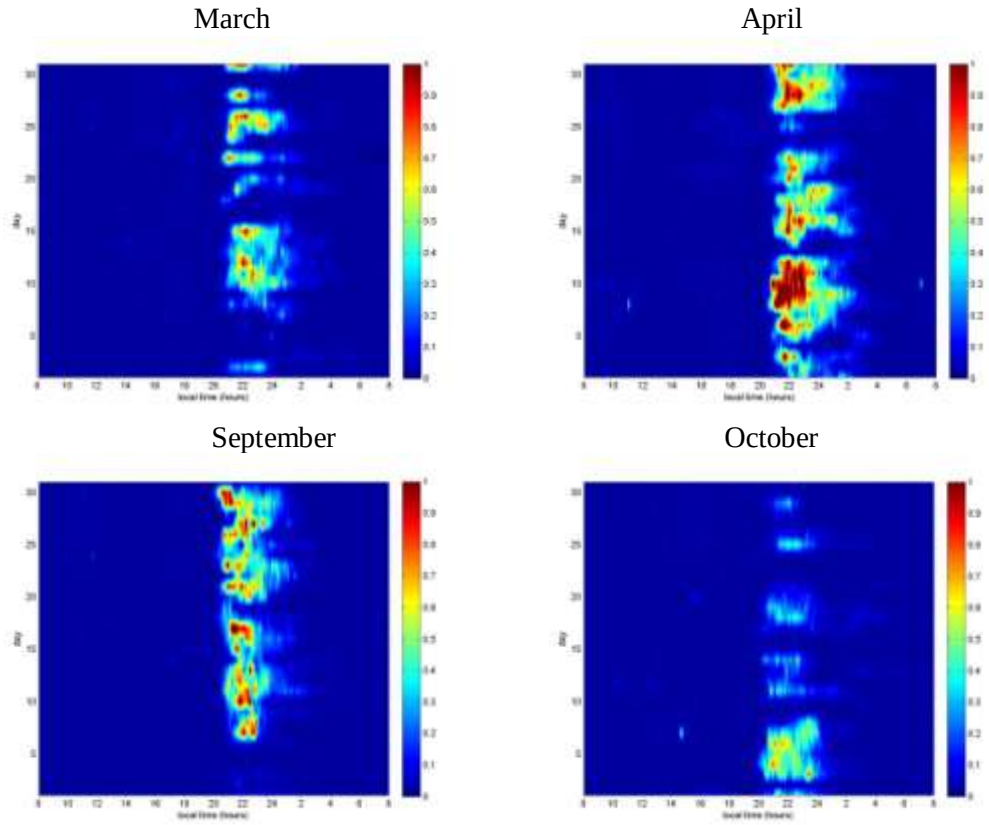

Figure 3-11 Monthly ROTI average during equinox months of year 2013

3.3. Number of Occurrence of GPS Scintillation Events

In this section we identify the number of occurrence of scintillation events throughout years 2012 and 2013 based on GPS scintillation parameters S4, phi60, and ROTI separately. An amplitude scintillation event is identified if S4 value is higher than 0.2 for at least 10 minutes. Separately for phi60, a phase scintillation event is identified if its value is larger than 0.1 for at least 10 minutes. Lastly, scintillation is identified if ROTI is larger than 0.5 as used in [44] for the same amount of time. Ten minutes minimum length is used to exclude false observation or insignificant scintillation from our analysis. Recorded data with satellite's elevation angle less than 20 degree are also excluded to minimize false scintillation event caused by multi path effect.

32 GPS satellites are used here. Data available from the receiver in S2 is starting from March 21st 2012 until end of 2013. If the scintillation parameters of any of the 32 GPS satellites meet the aforementioned conditions, it is counted as one scintillation event. Note that the counting will be performed for each S4, phi60, and ROTI separately.

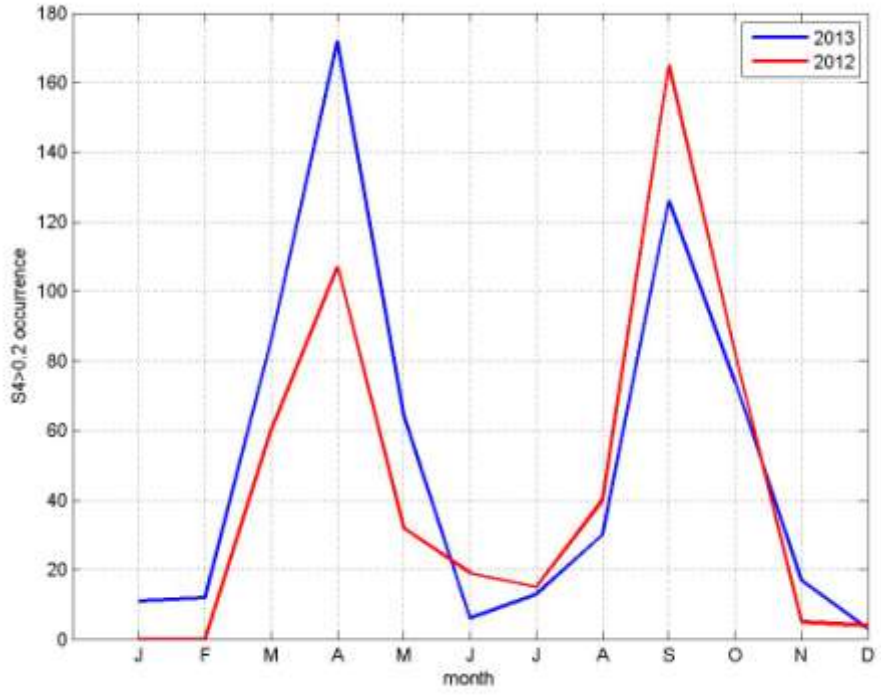

Figure 3-12 Monthly occurrence of S4>0.2

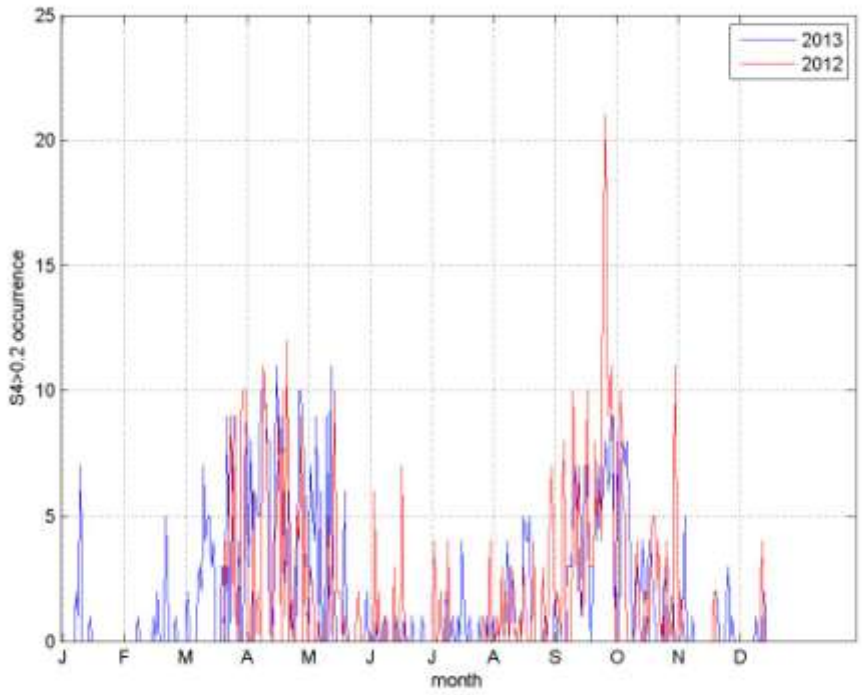

Figure 3-13 Daily occurrence of S4>0.2

Figure 3-12 shows the monthly occurrence of amplitude scintillations identified by S4 larger than 0.2 throughout years 2012 and 2013. It can be seen that for both years, the months April and September exhibit the highest number of occurrence of amplitude scintillations. On the other hand, Figure 3-13 shows the daily occurrence of S4 larger than 0.2 for the same period. Similarly, we also observe high occurrence of amplitude scintillations congregating around the months of April/May and September/October.

Table 3-1 S4>0.2 occurrence in 2012

2012	1	2	3	4	5	6	7	8	9	10	11	12	13	14	15	16	17	18	19	20	21	22	23	24	25	26	27	28	29	30	31	total
January	0	0	0	0	0	0	0	0	0	0	0	0	0	0	0	0	0	0	0	0	0	0	0	0	0	0	0	0	0	0	0	**0**
February	0	0	0	0	0	0	0	0	0	0	0	0	0	0	0	0	0	0	0	0	0	0	0	0	0	0	0	0	0	0	0	**0**
March	0	0	0	0	0	0	0	0	0	0	0	0	0	0	0	0	0	0	0	0	4	2	6	9	1	9	0	0	9	10	10	**60**
April	1	0	0	6	0	2	1	0	11	10	7	1	0	0	4	6	9	0	10	1	12	0	2	0	0	5	4	9	0	6	0	**107**
May	0	3	2	0	0	1	0	0	0	0	5	1	0	10	2	2	2	0	1	0	0	0	0	0	1	2	0	0	0	0	0	**32**
June	0	0	6	0	2	0	0	0	1	0	0	0	3	0	0	0	7	0	0	0	0	0	0	0	0	0	0	0	0	0	0	**19**
July	0	4	0	0	2	0	0	0	4	0	0	0	0	0	0	0	0	0	0	0	0	0	0	0	0	0	1	0	0	4	0	**15**
August	0	0	1	0	3	0	2	1	0	3	2	0	0	1	0	3	1	0	0	0	4	0	0	0	0	3	0	0	4	7	5	**40**
September	1	2	1	0	8	5	0	0	0	10	6	2	7	3	1	3	10	3	3	3	8	5	6	4	15	21	11	9	11	7	0	**165**
October	0	8	10	6	5	0	0	0	0	1	4	2	0	0	2	2	0	4	5	5	2	4	0	1	0	4	0	1	0	11	5	**82**
November	0	2	1	0	0	0	0	0	0	0	0	0	0	0	0	0	0	0	2	0	0	0	0	0	0	0	0	0	0	0	0	**5**
December	0	0	0	0	0	0	0	0	0	0	0	4	0	0	0	0	0	0	0	0	0	0	0	0	0	0	0	0	0	0	0	**4**

Table 3-2 S4>0.2 occurrence in 2013

2013	1	2	3	4	5	6	7	8	9	10	11	12	13	14	15	16	17	18	19	20	21	22	23	24	25	26	27	28	29	30	31	total
January	0	0	0	0	0	0	0	2	1	7	0	0	0	0	1	0	0	0	0	0	0	0	0	0	0	0	0	0	0	0	0	**11**
February	0	0	0	0	0	0	0	1	0	0	0	0	0	0	0	1	0	2	0	0	0	5	2	0	0	0	1	0	0	0	0	**12**
March	0	2	0	0	0	0	2	3	2	7	4	5	5	3	4	0	0	0	3	3	0	9	0	3	9	9	0	4	0	0	9	**86**
April	8	3	8	0	6	5	5	10	10	10	8	8	0	0	8	11	6	9	5	2	4	6	1	0	3	1	10	10	8	7	0	**172**
May	0	7	5	4	9	0	6	0	0	9	0	11	2	2	0	0	0	0	6	1	0	0	0	0	0	0	0	0	0	2	0	**64**
June	0	0	0	1	0	0	0	1	0	0	0	0	0	1	0	0	0	1	0	0	0	1	0	0	0	0	1	0	0	0	0	**6**
July	0	0	0	0	0	0	0	2	0	0	1	0	0	1	0	4	2	0	0	1	0	0	0	0	1	0	0	0	1	0	0	**13**
August	1	0	0	0	0	0	1	4	0	3	1	0	0	1	0	5	4	4	5	0	0	0	0	0	0	0	1	0	0	0	0	**30**
September	2	0	0	0	0	0	3	3	3	5	7	6	3	1	5	7	7	2	0	3	8	4	7	5	6	8	7	6	9	9	0	**126**
October	8	0	7	8	7	8	6	2	0	0	3	2	2	4	0	0	4	4	2	1	0	0	0	0	3	0	0	1	2	0	0	**74**
November	0	0	1	5	0	0	0	1	0	0	0	0	0	0	0	0	0	0	2	2	1	0	0	0	1	3	0	1	0	0	0	**17**
December	0	0	0	0	0	0	0	0	1	0	0	0	2	0	0	0	0	0	0	0	0	0	0	0	0	0	0	0	0	0	0	**3**

Table 3-1 and Table 3-2 show a more detailed number of occurrences of S4 larger than 0.2 for years 2012 and 2013, respectively. For both years, highest occurrences of amplitude scintillations are observed in months April and September.

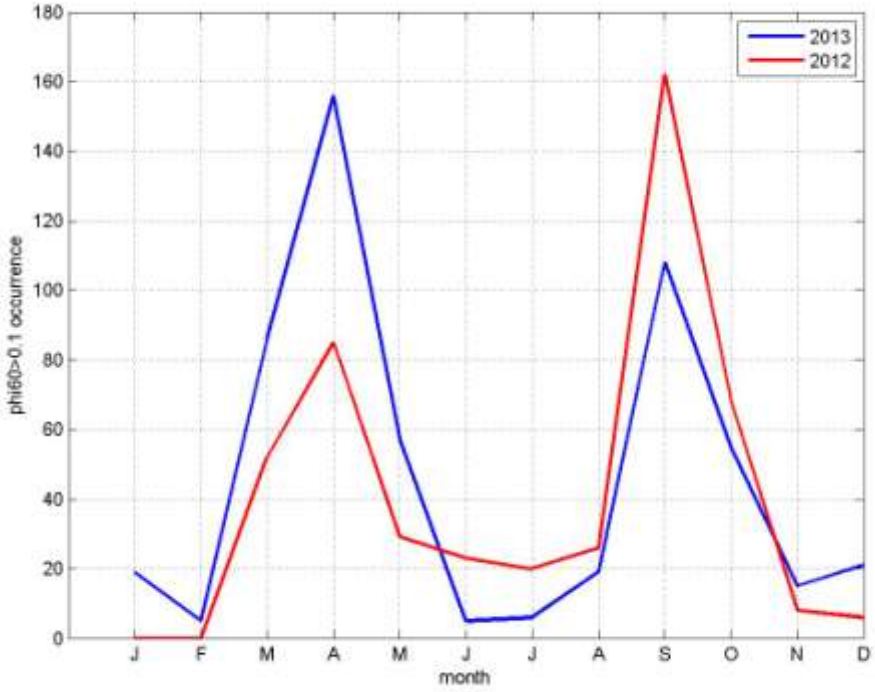

Figure 3-14 Monthly occurrence of Phi60>0.1

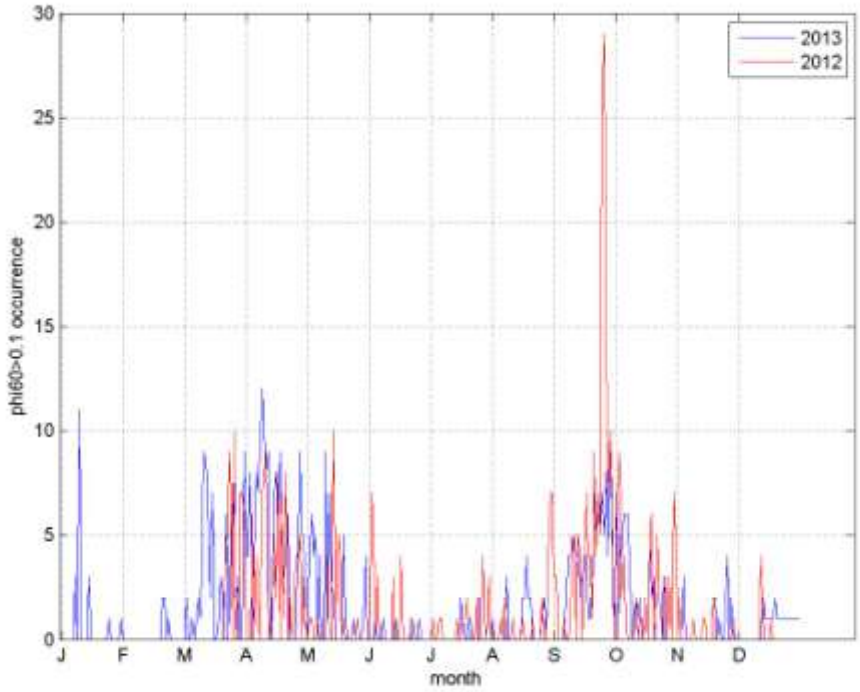

Figure 3-15 Daily occurrence of Phi60>0.1

Figure 3-14 and Figure 3-15 now show the monthly and daily occurrence of phi60 larger than 0.1 for years 2012 and 2013. Similar to amplitude scintillation, the months of April and September of both years also exhibit the highest occurrences of phase scintillations.

Table 3-3 phi60>0.1 occurrence in 2012

2012	1	2	3	4	5	6	7	8	9	10	11	12	13	14	15	16	17	18	19	20	21	22	23	24	25	26	27	28	29	30	31	total
January	0	0	0	0	0	0	0	0	0	0	0	0	0	0	0	0	0	0	0	0	0	0	0	0	0	0	0	0	0	0	0	0
February	0	0	0	0	0	0	0	0	0	0	0	0	0	0	0	0	0	0	0	0	0	0	0	0	0	0	0	0	0	0	0	0
March	0	0	0	0	0	0	0	0	0	0	0	0	0	0	0	0	0	0	0	0	2	4	7	9	0	10	0	0	7	7	6	52
April	0	0	0	6	0	4	1	0	7	8	9	0	0	0	5	2	8	0	7	1	8	0	2	0	1	4	4	5	0	3	0	85
May	0	1	1	0	0	1	0	0	0	0	4	0	0	10	1	4	5	0	1	0	0	0	0	0	0	1	0	0	0	0	0	29
June	0	7	5	0	3	0	0	0	0	0	0	0	3	0	0	0	4	0	0	0	0	0	1	0	0	0	0	0	0	0	0	23
July	0	1	0	0	1	1	0	0	0	0	0	0	0	1	0	0	1	1	2	1	1	0	0	2	0	0	4	1	0	3	0	20
August	0	0	0	0	1	0	2	0	0	0	1	0	0	0	0	1	0	0	0	0	1	0	0	0	0	2	0	0	4	7	7	26
September	3	3	0	0	0	1	0	0	1	5	4	0	5	4	0	2	7	4	4	1	9	4	7	5	26	29	14	7	10	7	0	162
October	0	7	9	2	4	1	0	0	0	1	2	0	1	1	0	2	0	5	6	0	2	5	1	1	0	3	0	3	0	7	5	68
November	0	2	0	0	0	0	0	0	1	0	0	0	0	1	1	0	0	0	2	0	0	0	0	0	0	0	0	0	1	0	0	8
December	0	0	0	0	0	0	0	0	0	0	0	4	1	0	0	0	1	0	0	0	0	0	0	0	0	0	0	0	0	0	0	6

Table 3-4 phi60>0.1 occurrences in 2013

2013	1	2	3	4	5	6	7	8	9	10	11	12	13	14	15	16	17	18	19	20	21	22	23	24	25	26	27	28	29	30	31	total
January	0	0	0	0	0	0	0	3	0	11	0	0	0	0	3	0	0	0	0	0	0	0	0	0	1	0	0	0	0	0	1	19
February	0	0	0	0	0	0	0	0	0	0	0	0	0	0	0	0	0	0	0	0	2	2	0	1	0	0	0	0	0	0	0	5
March	0	2	0	0	1	0	1	2	1	7	9	8	5	2	7	0	0	1	3	2	0	6	0	3	6	8	0	3	0	0	9	86
April	4	4	8	0	4	8	7	9	12	10	8	9	0	1	7	8	6	9	5	3	4	6	0	0	0	0	5	9	5	5	0	156
May	0	4	6	4	5	0	4	0	0	9	1	7	3	2	0	0	0	0	5	1	0	0	0	1	0	0	0	0	1	4	0	57
June	0	0	0	1	0	0	0	1	0	0	0	0	0	1	0	0	0	0	0	0	0	1	0	0	0	1	0	0	0	0	0	5
July	0	0	0	0	0	0	0	0	0	0	0	0	0	0	0	2	1	0	0	1	0	0	0	0	2	0	0	0	0	0	0	6
August	1	0	0	0	0	0	0	3	0	0	0	0	0	0	0	2	2	4	2	2	0	0	0	0	0	1	2	0	0	0	0	19
September	0	0	0	0	0	0	2	4	4	4	5	4	4	2	3	4	4	1	1	3	7	5	7	5	7	5	8	4	9	6	0	108
October	7	0	5	4	6	6	6	3	0	0	2	1	2	0	0	0	0	5	2	3	0	0	0	0	3	0	0	0	0	0	0	55
November	0	0	0	3	0	0	0	0	0	0	0	0	0	0	0	0	0	0	2	2	0	1	0	0	1	4	0	2	0	0	0	15
December	0	0	0	0	0	0	0	0	0	0	0	0	2	1	1	1	1	1	2	1	1	1	1	1	1	1	1	1	1	1	1	21

Table 3-3 and Table 3-4 show a more detailed number of occurrence of phi60 larger than 0.1 for years 2012 and 2013, respectively. For both years, highest occurrences of phase scintillations are again observed in equinox months April and September.

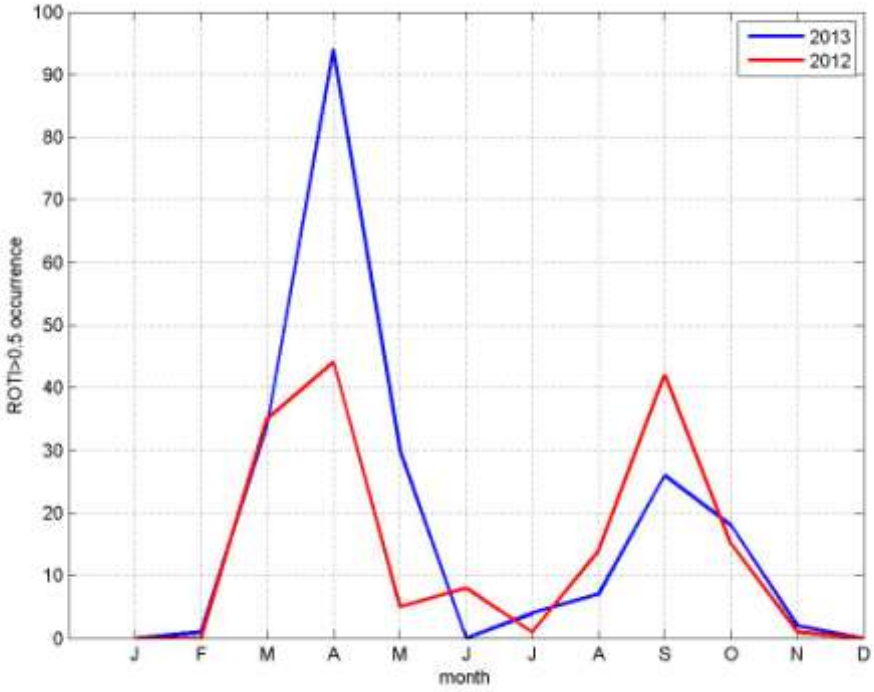

Figure 3-16 Monthly occurrence of ROTI>0.5

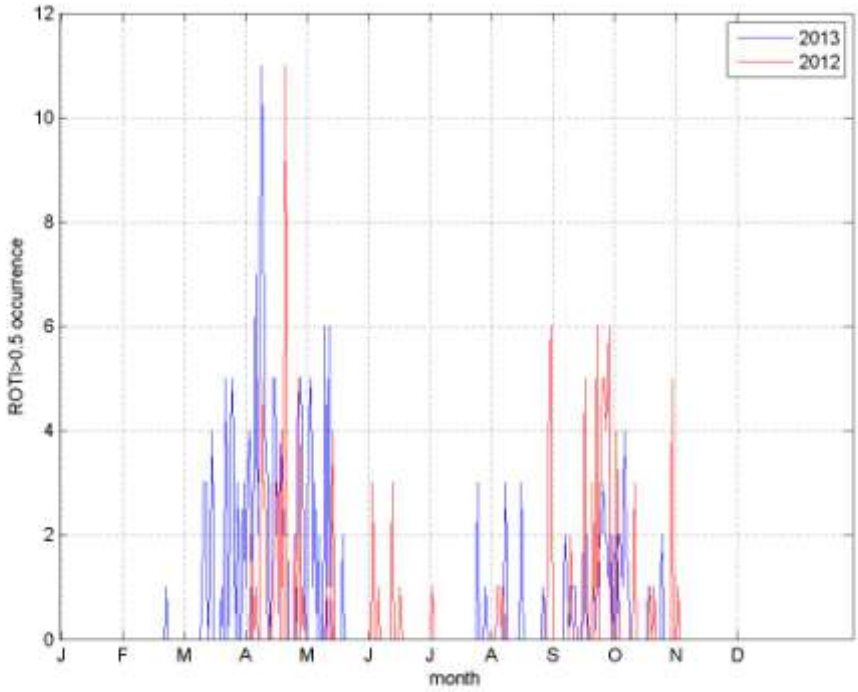

Figure 3-17 Daily occurrence of ROTI>0.5

Figure 3-16 and Figure 3-17 now show the monthly and daily occurrences of ROTI larger than 0.5 for years 2012 and 2013. Similar to amplitude and phase scintillation, the equinox months of April and September of both years exhibit the highest number of high ROTI occurrences which indicate high TEC fluctuation.

Table 3-5 ROTI>0.5 occurrence in 2012

2012	1	2	3	4	5	6	7	8	9	10	11	12	13	14	15	16	17	18	19	20	21	22	23	24	25	26	27	28	29	30	31	total
January	0	0	0	0	0	0	0	0	0	0	0	0	0	0	0	0	0	0	0	0	0	0	0	0	0	0	0	0	0	0	0	0
February	0	0	0	0	0	0	0	0	0	0	0	0	0	0	0	0	0	0	0	0	0	0	0	0	0	0	0	0	0	0	0	0
March	0	0	0	0	0	0	0	0	0	0	0	0	0	0	0	0	0	0	0	0	0	0	0	0	0	0	0	0	0	0	0	0
April	0	0	0	2	0	1	0	0	5	3	3	0	0	0	1	3	3	0	4	0	11	0	0	0	0	2	0	5	0	1	0	44
May	0	0	0	0	0	0	0	0	0	0	1	0	0	4	0	0	0	0	0	0	0	0	0	0	0	0	0	0	0	0	0	5
June	0	0	3	0	0	1	0	0	0	0	0	0	3	0	0	0	1	0	0	0	0	0	0	0	0	0	0	0	0	0	0	8
July	0	1	0	0	0	0	0	0	0	0	0	0	0	0	0	0	0	0	0	0	0	0	0	0	0	0	0	0	0	0	0	1
August	0	0	0	1	1	0	1	0	0	0	0	0	0	0	0	0	0	0	0	0	0	0	0	0	0	0	0	0	0	5	6	14
September	0	0	0	0	0	0	0	0	0	2	0	0	0	0	0	1	5	1	0	0	3	0	6	0	4	5	5	4	6	0	0	42
October	0	4	1	0	0	0	0	0	0	0	3	0	0	0	0	0	0	0	1	0	1	0	0	0	0	0	0	0	0	5	0	15
November	0	1	0	0	0	0	0	0	0	0	0	0	0	0	0	0	0	0	0	0	0	0	0	0	0	0	0	0	0	0	0	1
December	0	0	0	0	0	0	0	0	0	0	0	0	0	0	0	0	0	0	0	0	0	0	0	0	0	0	0	0	0	0	0	0

Table 3-6 ROTI>0.5 occurrence in 2013

2013	1	2	3	4	5	6	7	8	9	10	11	12	13	14	15	16	17	18	19	20	21	22	23	24	25	26	27	28	29	30	31	total
January	0	0	0	0	0	0	0	0	0	0	0	0	0	0	0	0	0	0	0	0	0	0	0	0	0	0	0	0	0	0	0	0
February	0	0	0	0	0	0	0	0	0	0	0	0	0	0	0	0	0	0	0	0	0	0	1	0	0	0	0	0	0	0	0	1
March	0	0	0	0	0	0	0	0	0	1	3	3	0	1	4	0	0	0	0	1	0	5	0	1	5	4	0	3	0	0	3	34
April	1	3	4	0	2	7	2	6	11	8	4	3	0	1	5	5	2	3	4	2	2	2	0	0	0	0	4	5	5	3	0	94
May	0	4	5	1	3	0	2	0	0	6	0	6	1	0	0	0	0	0	2	0	0	0	0	0	0	0	0	0	0	0	0	30
June	0	0	0	0	0	0	0	0	0	0	0	0	0	0	0	0	0	0	0	0	0	0	0	0	0	0	0	0	0	0	0	0
July	0	0	0	0	0	0	0	0	0	0	0	0	0	0	0	0	0	0	0	0	0	0	0	0	3	0	0	0	1	0	0	4
August	0	0	0	0	0	0	0	3	0	0	0	0	0	0	0	3	0	0	0	0	0	0	0	0	0	0	1	0	0	0	0	7
September	0	0	0	0	0	0	2	1	0	1	1	1	0	0	0	0	2	0	0	0	3	0	1	2	2	3	2	2	1	2	0	26
October	2	0	2	2	1	4	2	1	0	0	0	0	0	0	0	0	0	1	1	0	0	0	0	0	2	0	0	0	0	0	0	18
November	0	0	0	1	0	0	0	0	0	0	0	0	0	0	0	0	0	0	0	0	0	0	0	0	0	0	0	1	0	0	0	2
December	0	0	0	0	0	0	0	0	0	0	0	0	0	0	0	0	0	0	0	0	0	0	0	0	0	0	0	0	0	0	0	0

Table 3-5 and Table 3-6 show a more detailed number of occurrence of ROTI larger than 0.5 for years 2012 and 2013, respectively. For both years, highest occurrence of TEC fluctuation is again observed in months April and September.

To conclude for this section, ionospheric scintillation peak usually happen in around April and September (equinox) for both years 2012 and 2013, which is indicated by high S4, phi60, and ROTI.

3.4. Selected Ionospheric Scintillation Events

For closer analysis, selected GPS scintillation events during the equinox months in year 2013 are done. The events of S4 values larger than 0.2 with considerably long duration are first identified. It is then plotted along with other scintillation parameters such as phi60 and ROTI for the same duration and PRN. Also plotted are the vTEC, C/N_0 of the signal, satellite elevation angle, and the rate of change of TEC (ROT). Figure 3-18 and Figure 3-19 show the plots of various scintillation parameters, on 31 March 2013 of satellite PRN 23 and 9 April 2013 of satellite PRN 20. It can be seen that high S4 is generally accompanied by high phi60, indicating that amplitude and phase scintillations usually occur concurrently. Besides that, we also observe fluctuations in the ROT and high ROTI during this period, which shows the presence of plasma bubble irregularities in the ionospheric layer. Evidently, both signal intensity and the carrier phase of the GPS signal exhibit fluctuations during this period, which signifies propagation through the plasma bubble irregularities of the ionosphere layer.

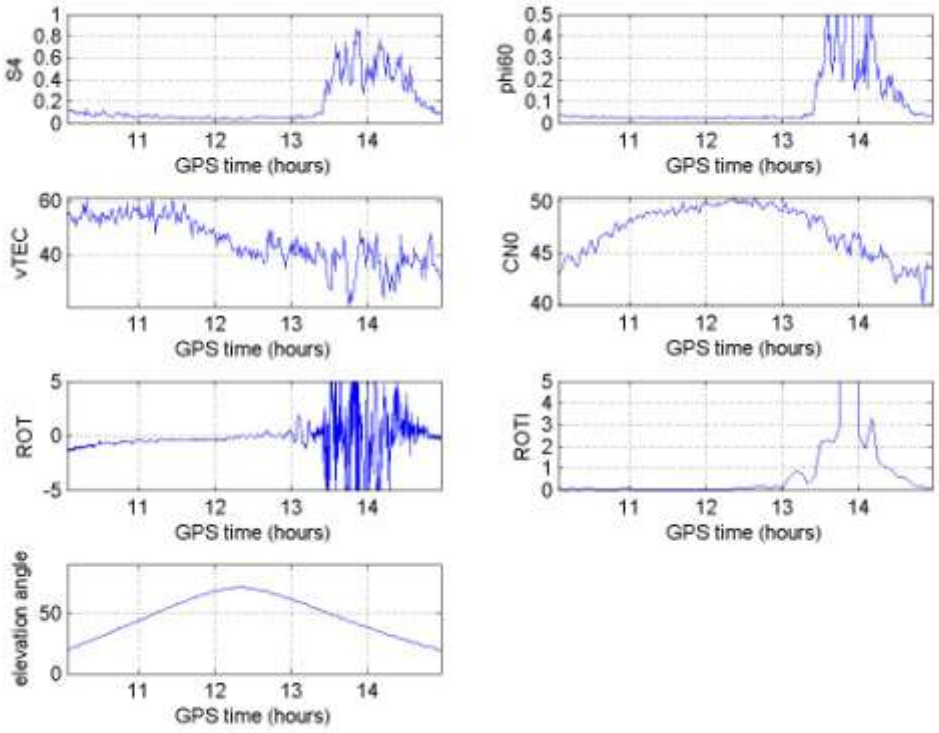

Figure 3-18 Scintillation parameters on 31 March 2013 of PRN 23

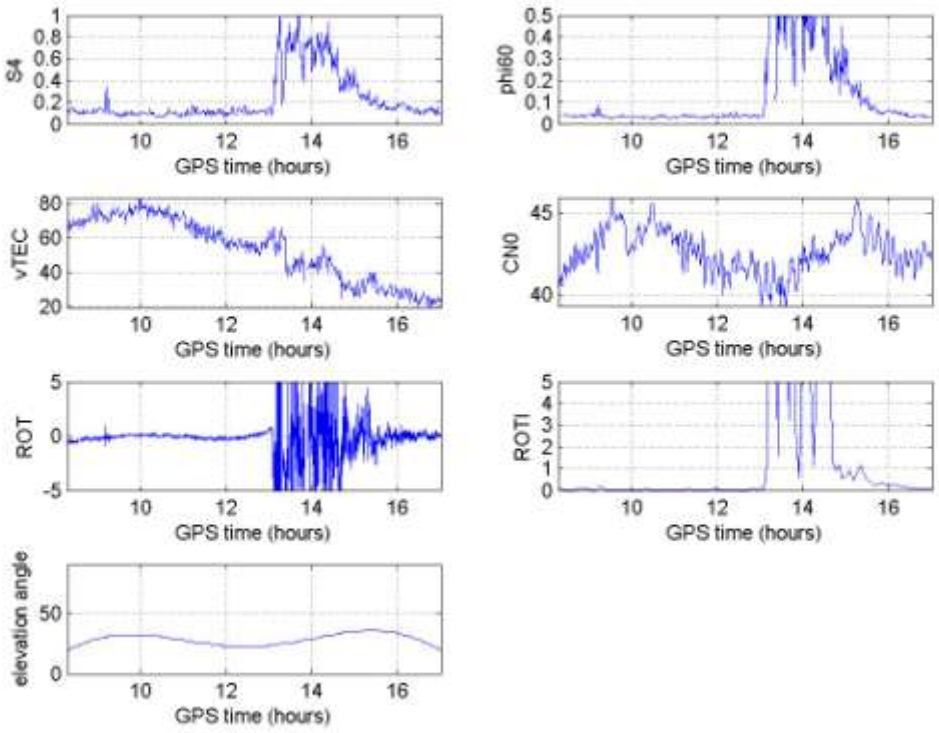

Figure 3-19 Scintillation parameters on 9 April 2013 of PRN 20

3.5. Histogram of the GPS Satellites with Scintillation at Night

Ionospheric scintillation can reduce the accuracy of GNSS positioning and can even prevent the receiver from locking into satellites. At least four visible satellites are needed to obtain position information by GPS. Severe ionospheric scintillation that affects too many satellites will leave not enough number of usable satellites for position calculation. Based on our observation, in Singapore typically around six GPS satellites are always visible all the time. This means that when more than two satellites are suffering from severe ionospheric scintillation at a time, it is likely that GPS receiver cannot obtain position solution due to lacking of satellites number.

In this section the histogram of the number of GPS satellites suffering from scintillation is presented. This analysis gives us the probability estimation of the number of satellites that suffer from scintillation every time. This analysis is done for night time during equinox months when scintillations commonly happen. S4>0.2 is

used to determine that ionospheric scintillation is happening. S4 is obtained every minute. For each minute the number of satellites with S4>0.2 is counted.

Figure 3-20 and Figure 3-21 show the histogram of the occurrence percentage of concurrently scintillation afflicted GPS satellites at night during equinox months in year 2012 and 2013. Night is defined as time period begins at 6 pm and ends at 6 am the next day. Night scintillation is expected to be more frequent than day scintillation. Equinox months is chosen as ionospheric scintillation is most severe in this period. Besides that, the same data from June and July 2013 which are non equinox month are also presented as comparison in Figure 3-22.

Among those presented equinox months, the April 2013 data shows the highest percentage of more than two satellites suffering from scintillation. The receiver sees all satellites without scintillation for 73.8 % of the time. The occurrence of only one satellite affected by scintillation is 11.88% of the time. Two satellites are seen with scintillation at 6.35% of the time. Subsequently, three, four, five, six, seven, and eight concurrently afflicted satellites happen at 3.81%, 2.40%, 1.16%, 0.43%, 0.13%, and 0.04% of the time respectively. Hence, the occurrence of more than two satellites affected by scintillation is 7.93% of the time.

In April 2012, the occurrence of more than two satellites affected by scintillation is lower, only 3.65%. This is because in year 2012 the solar activity is still ascending and hasn't reached its peak in around year 2013 or 2014. Higher solar activity increases the possibility of ionospheric scintillation. Nevertheless, this occurrence in April 2012 is still much higher compared to the non equinox data shown in Figure 3-22. In June and July 2013, the occurrence of more than two satellites affected by scintillation is nearly zero, only 0.01% and 0.07%. The effect solar activity and solar cycle will be further analyzed in chapter three of this thesis.

For closer analysis, Figure 3-23 shows the histogram of the occurrence percentage of concurrently scintillation afflicted GPS satellites at 20.00-02.00 local time during April 2013. High ionospheric scintillation is typically concentrated in this time span. The occurrence of only one satellite affected by scintillation is 19.63% of the time. Two satellites are seen with scintillation at 12.45% of the time. Subsequently, three,

four, five, six, seven, and eight concurrently afflicted satellites happen at 7.56%, 4.75%, 2.28%, 0.83%, 0.25%, and 0.06% of the time respectively. Hence, the occurrence of more than two satellites affected by scintillation is 15.73% of the time.

In conclusion, it has been shown that at 20.00-02.00 local time, the occurrence concurrently scintillation afflicted GPS satellites can reach 15.73%. This result shows that during this time span the GPS applications, especially those which need continuous tracking are likely to be affected by ionospheric scintillation. Further analysis involving tracking and positioning performance of GPS receiver during scintillation is needed to comprehensively study the adverse effect of such scintillation.

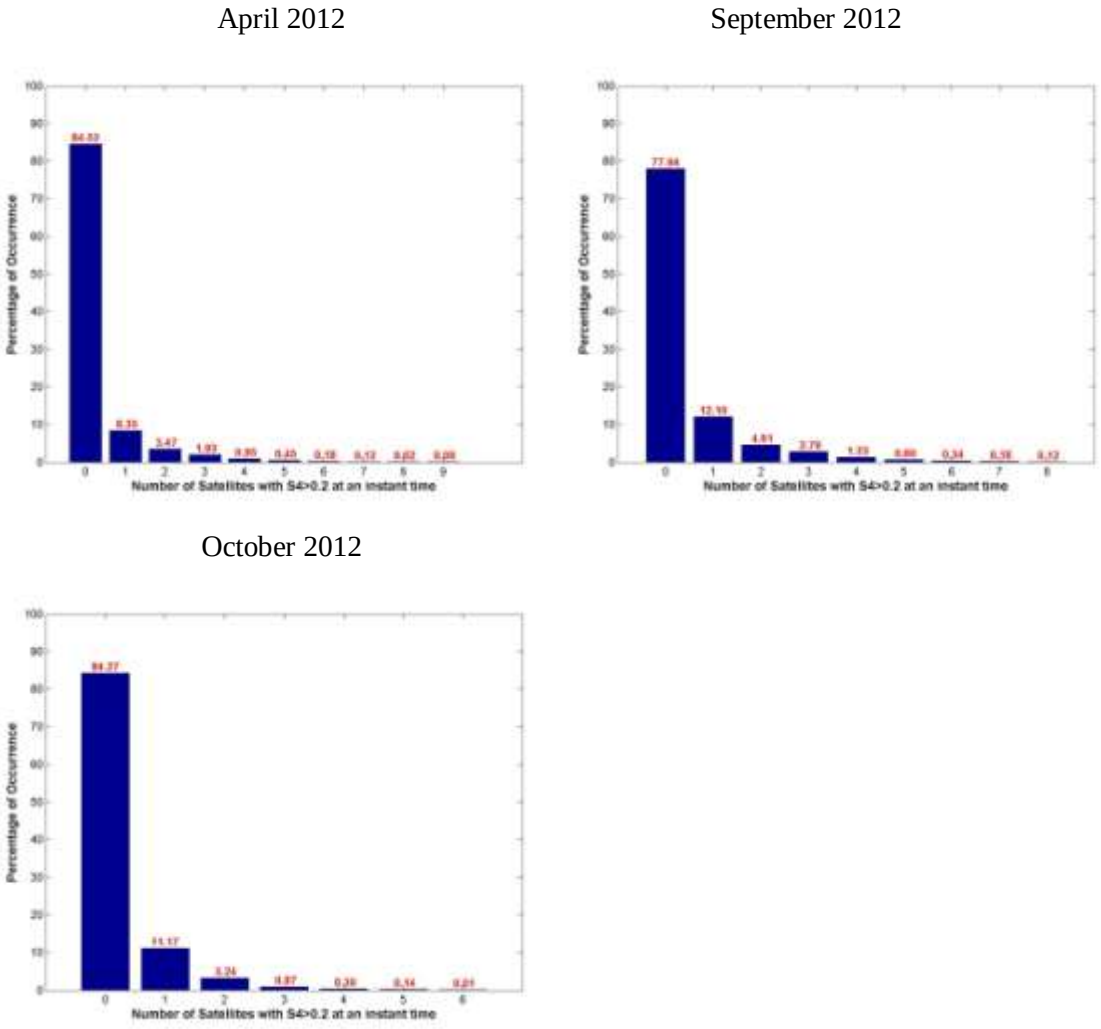

Figure 3-20 Distribution of the number of concurrently scintillation affected GPS satellites at night during equinox months of year 2012

March 2013 April 2013

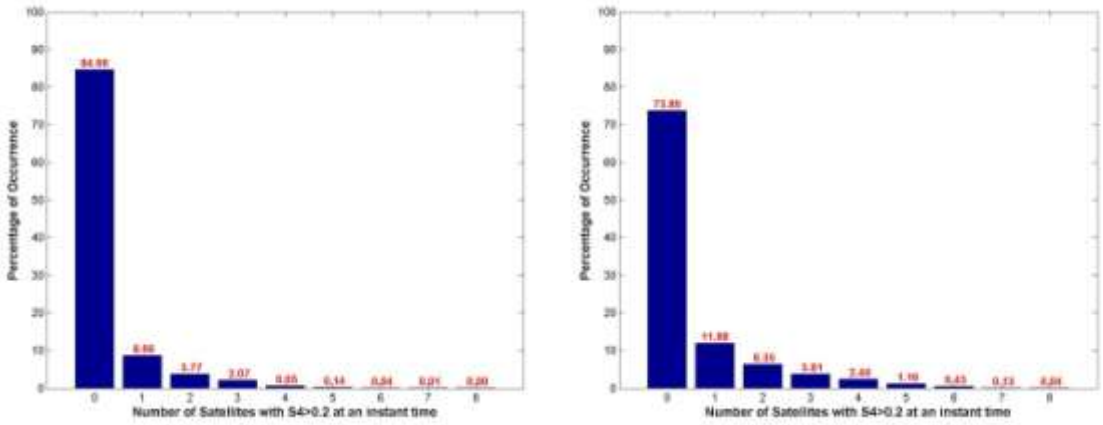

September 2013 October 2013

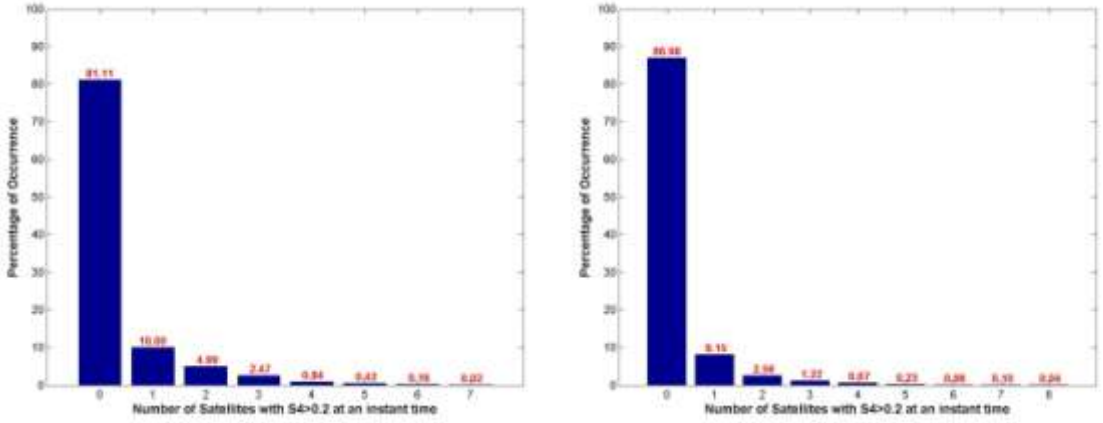

Figure 3-21 Distribution of the number of concurrently scintillation affected GPS satellites at night during equinox months of year 2013

June 2013 July 2013

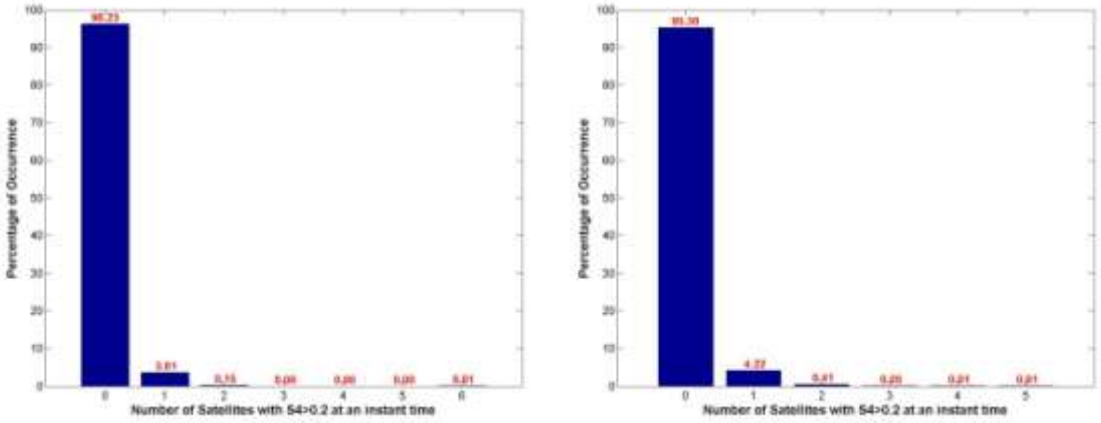

Figure 3-22 Distribution of the number of concurrently scintillation affected GPS satellites at night during non equinox months of year 2013

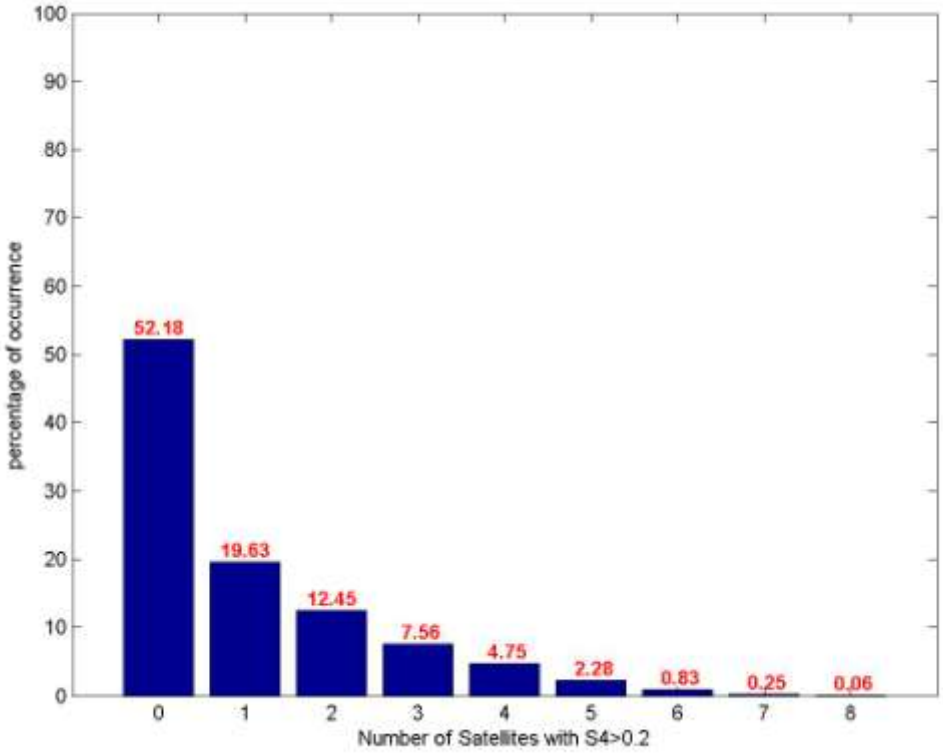

Figure 3-23 Distribution of the number of concurrently scintillation affected GPS satellites at 20.00-02.00 local time during April 2013

3.6. Comparison among S2, S2.1, and Nanyang House Location

3.6.1. Comparison of S4, Phi60, and ROTI

In this section, we try to compare the scintillation parameters recorded from receivers in S2, S2.1, and Nanyang House. As shown by the map in Figure 3-1, the distance between S2 and S2.1 is around 80 meter, while the distance between S2 and Nanyang House is 1.01 km. Figure 3-24 to Figure 3-33 show some comparisons of the scintillation parameters obtained from those receivers. Ten selected scintillation events are plotted. Results show a very close recorded scintillation parameters between the 3 receivers, even though the furthest distance is at 1 km apart. This suggests that the plasma irregularities within the ionosphere during the scintillation events are in larger scales of more than 1 km. Note that in Figure 3-32, it is shown that no data is available at around 11.30 – 13.30 GPS time. During this period, the particular satellite elevation angle is lower than 20^0 so it is not included on this analysis to reduce multipath issue.

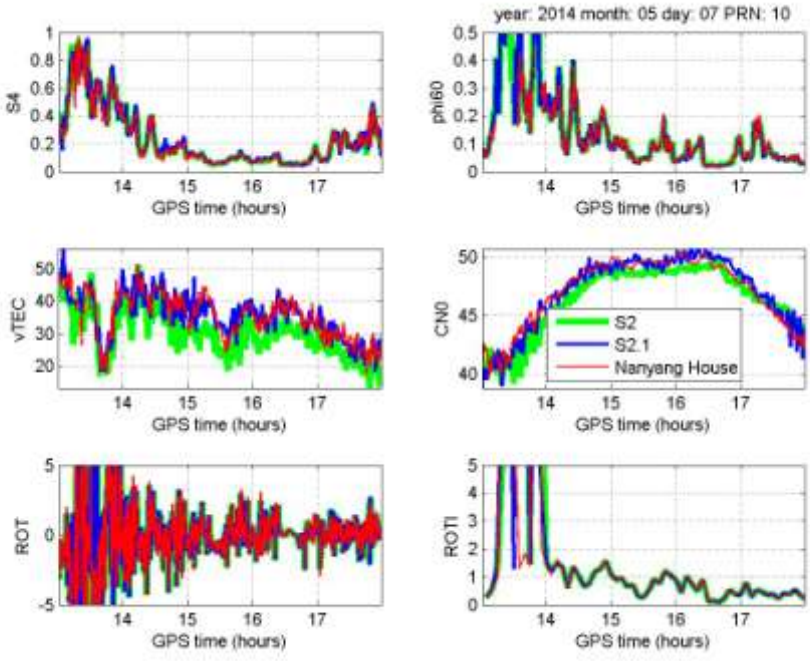

Figure 3-24 Scintillation parameters of receivers at S2, S2.1, and Nanyang House on 7 May 2014, PRN 10

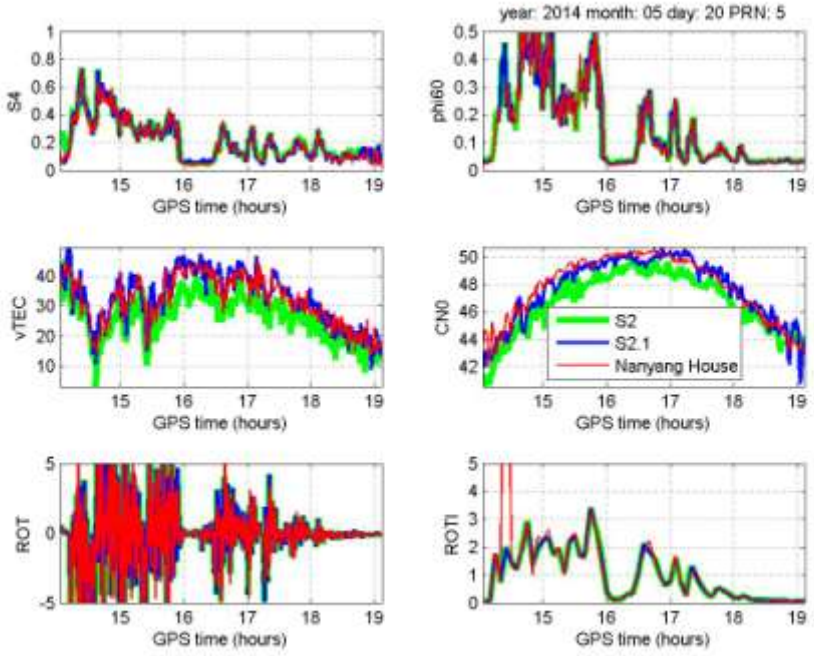

Figure 3-25 Scintillation parameters of receivers at S2, S2.1, and Nanyang House on 5 May 2014, PRN 5

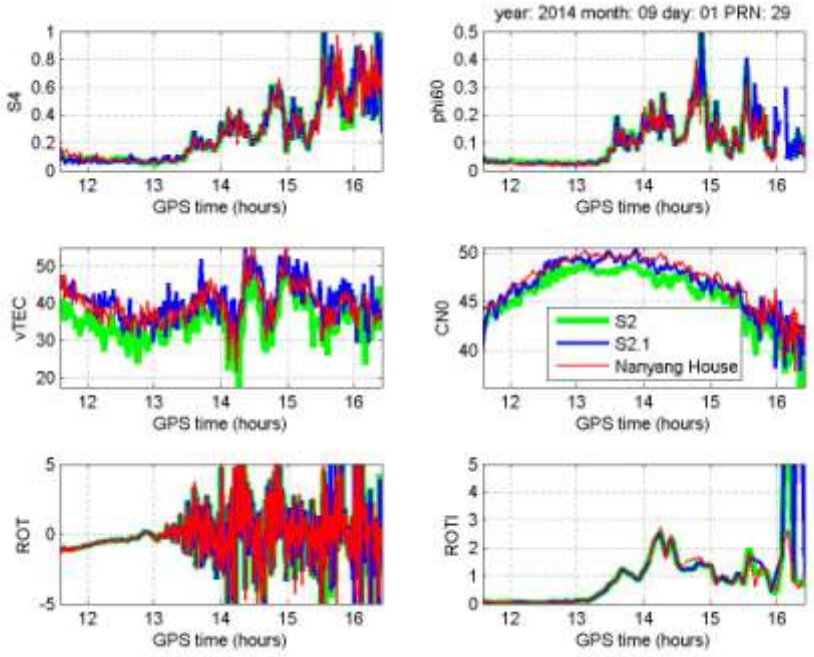

Figure 3-26 Scintillation parameters of receivers at S2, S2.1, and Nanyang House on 1 September 2014, PRN 29

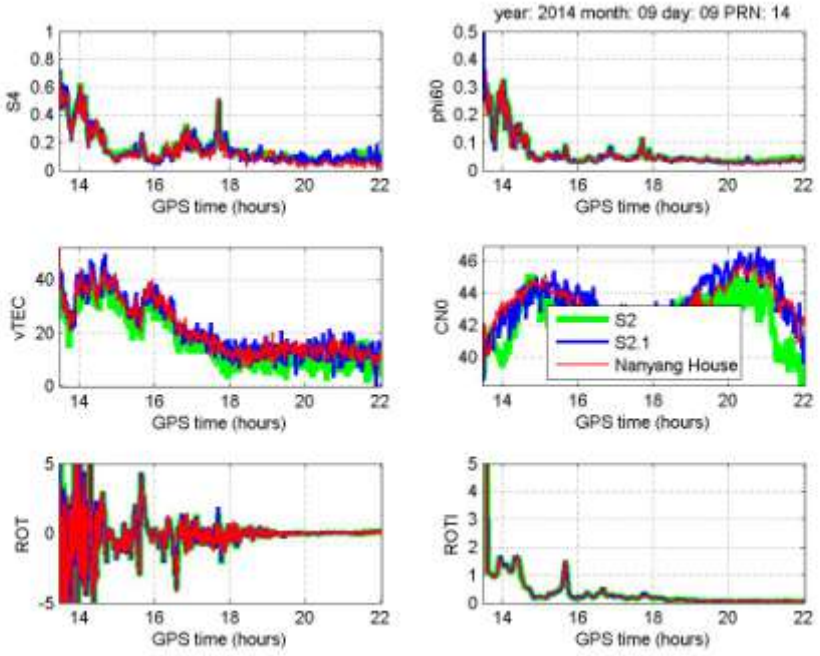

Figure 3-27 Scintillation parameters of receivers at S2, S2.1, and Nanyang House on 9 September 2014, PRN 14

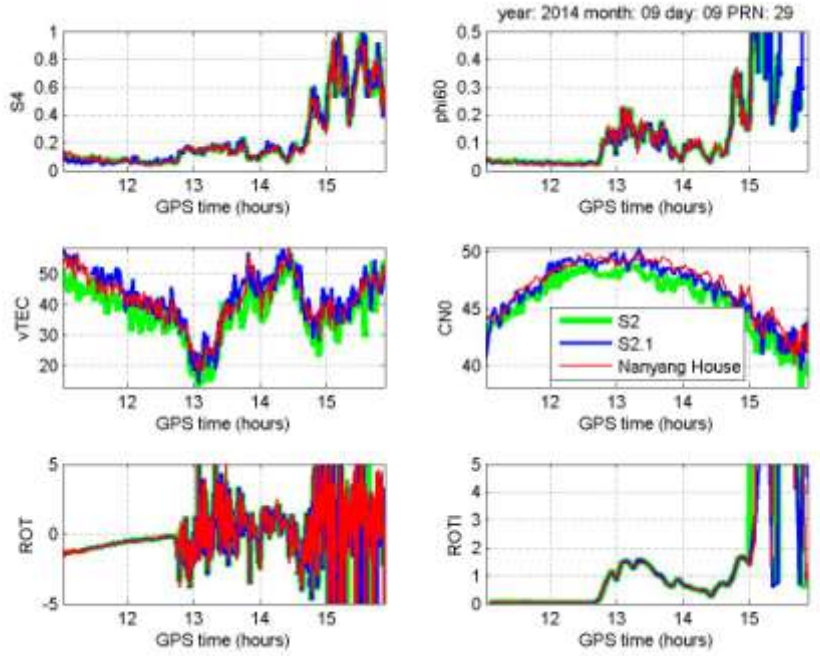

.

Figure 3-28 Scintillation parameters of receivers at S2, S2.1, and Nanyang House on 9 September 2014, PRN 29

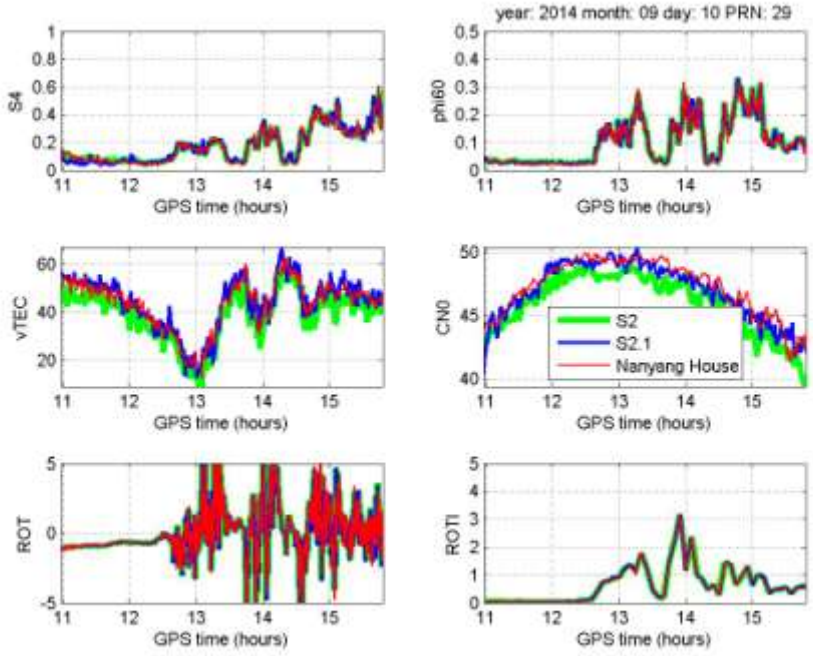

Figure 3-29 Scintillation parameters of receivers at S2, S2.1, and Nanyang House on 10 September 2014, PRN 29

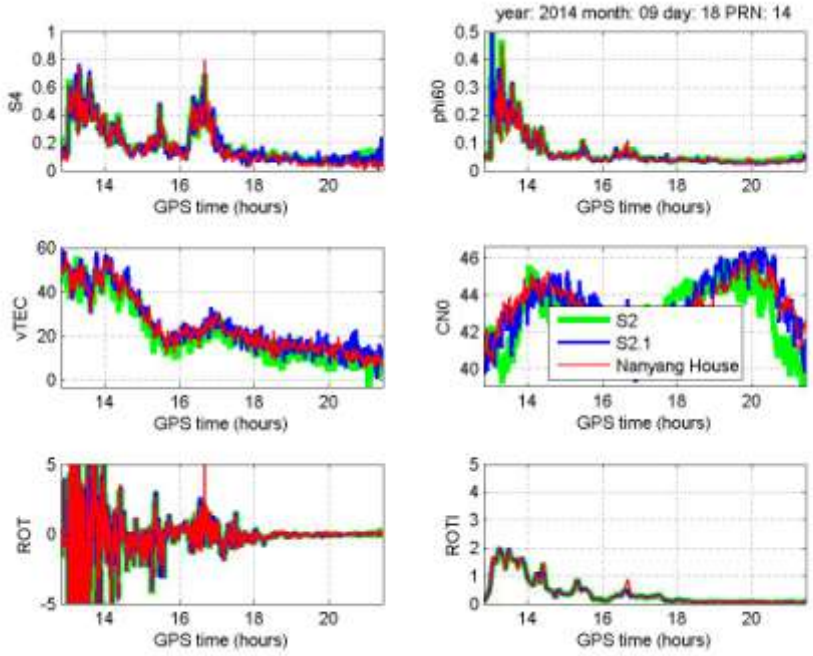

Figure 3-30 Scintillation parameters of receivers at S2, S2.1, and Nanyang House on 18 September 2014, PRN 14

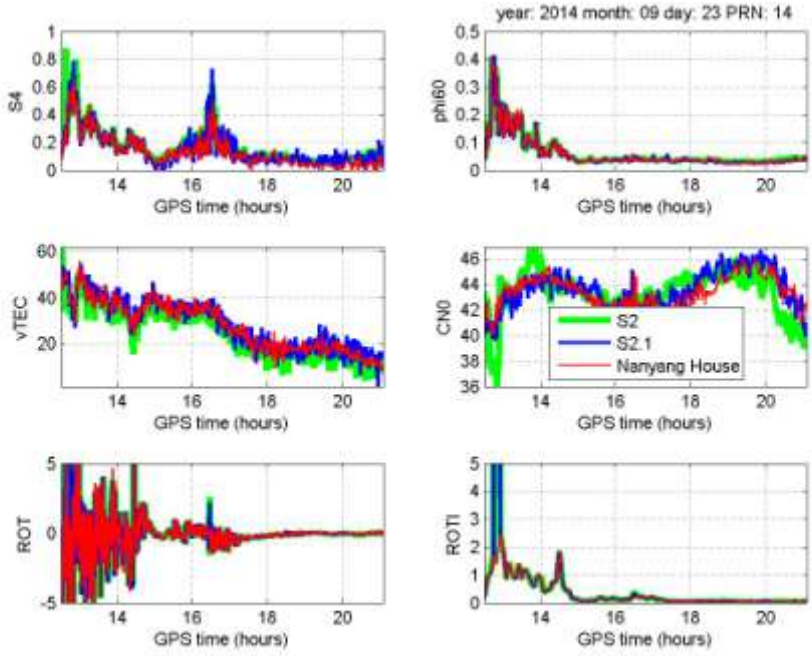

Figure 3-31 Scintillation parameters of receivers at S2, S2.1, and Nanyang House on 23 September 2014, PRN 14

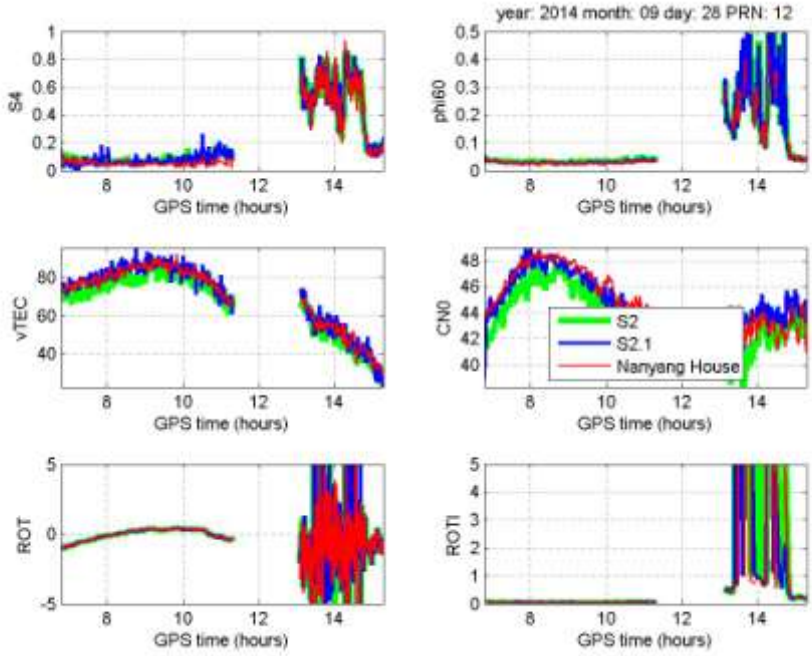

Figure 3-32 Scintillation parameters of receivers at S2, S2.1, and Nanyang House on 28 September 2014, PRN 12

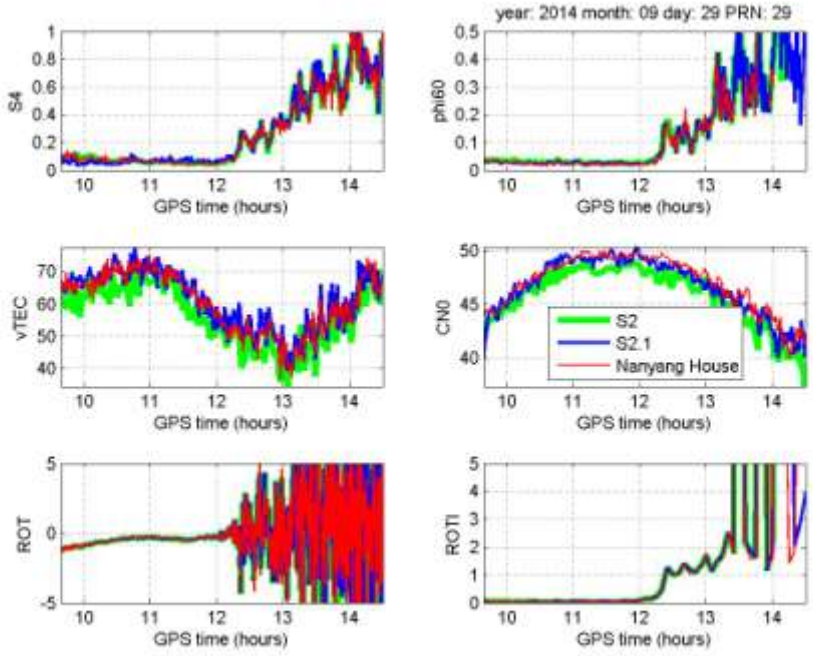

Figure 3-33 Scintillation parameters of receivers at S2, S2.1, and Nanyang House on 29 September 2014, PRN 29

Next, correlation coefficients among those three locations are calculated for S4, phi60, and ROTI. The correlation coefficient between variables X and Y is calculated by [5]

$$\rho_{X,Y} = \frac{cov(X,Y)}{\sigma_X \sigma_Y} = \frac{E[(X-\mu_X)(Y-\mu_Y)}{\sigma_X \sigma_Y} \qquad \textbf{(3-2)}$$

where *cov(X,Y)* is the covariance of variables X and Y, σ_X is the standard deviation of X, μ_X is the mean of X, and E is the expectation.

Table 3-7 shows the correlation coefficient of S4, phi60 and ROTI between receivers in S2 and S2.1. Table 3-8 shows the correlation coefficient of those between receivers in S2 and Nanyang House. The obtained correlation coefficients are generally near to one, which indicate scintillation similarity among those locations.

Table 3-7 Correlation coefficients between S2 and S2.1

Day and PRN	S4	phi60	ROTI
7 May 2014, PRN 10	0.99	0.79	0.98
20 May 2014, PRN 5	0.97	1.00	0.98
1 September 2014, PRN 29	0.99	0.99	0.96
9 September 2014, PRN 29	0.99	0.92	0.98
9 September 2014, PRN 14	0.97	0.99	0.99
10 September 2014, PRN 29	0.98	0.99	0.98
18 September 2014, PRN 14	0.97	0.99	0.99
23 September 2014, PRN 14	0.92	0.99	0.99
28 September 2014, PRN 12	0.99	0.97	0.86
29 September 2014, PRN 29	0.99	0.98	0.85

Table 3-8 Correlation coefficients between S2 and Nanyang House

Day and PRN	S4	phi60	ROTI
7 May 2014, PRN 10	0.97	0.97	0.97
20 May 2014, PRN 5	0.97	0.99	0.97
1 September 2014, PRN 29	0.91	0.96	0.97
9 September 2014, PRN 29	0.98	0.99	0.96
9 September 2014, PRN 14	0.97	0.99	0.99
10 September 2014, PRN 29	0.97	0.99	0.98
18 September 2014, PRN 14	0.94	0.98	0.98
23 September 2014, PRN 14	0.87	0.99	0.99
28 September 2014, PRN 12	0.98	0.98	0.88
29 September 2014, PRN 29	0.97	0.98	0.83

3.6.2. Cross Correlation of Signal Intensity and Carrier Phase among Locations

It has been shown that the scintillation parameters among different receivers in NTU (S2, S2.1, and Nanyang House) show very close results and there is not observed variation in the temporal factor. This is because the distance among those receivers are too near to generate variation. The time resolution of S4 and phi60 is only one minute which is not able to provide any observable difference within such near distance.

To be able to observe some temporal variation among those locations, signal intensity (SI) and detrended carrier phase with 50 Hz data rate are used. Data presented here is taken on 20 September 2014 at around 14.00 universal time (UT) or 22.00 local time (LT) when scintillation happened. Ten minutes data are used to get the cross correlation between two receivers. Cross-correlation is a measure of similarity of two waveforms as a function of a time-lag applied to one of them. For discrete functions, the cross-correlation is defined as:

$$(f \star g)[n] \stackrel{\text{def}}{=} \sum_{m=-\infty}^{\infty} f^*[m]\, g[m+n] \qquad \textbf{(3.3)}$$

where *f** denotes the complex conjugate of *f* and *n* is the time lag.

Figure 3-34 shows detrended SI of satellite PRN 14 during the selected scintillation time. It can be seen that the SI of receiver at S2 and S2.1 are very close, while the one from receiver at Nanyang House (NH) is lagging by certain period. Similar behavior is also observed on the detrended carrier phase shown in Figure 3-35. This time lag or delay will be quantified next.

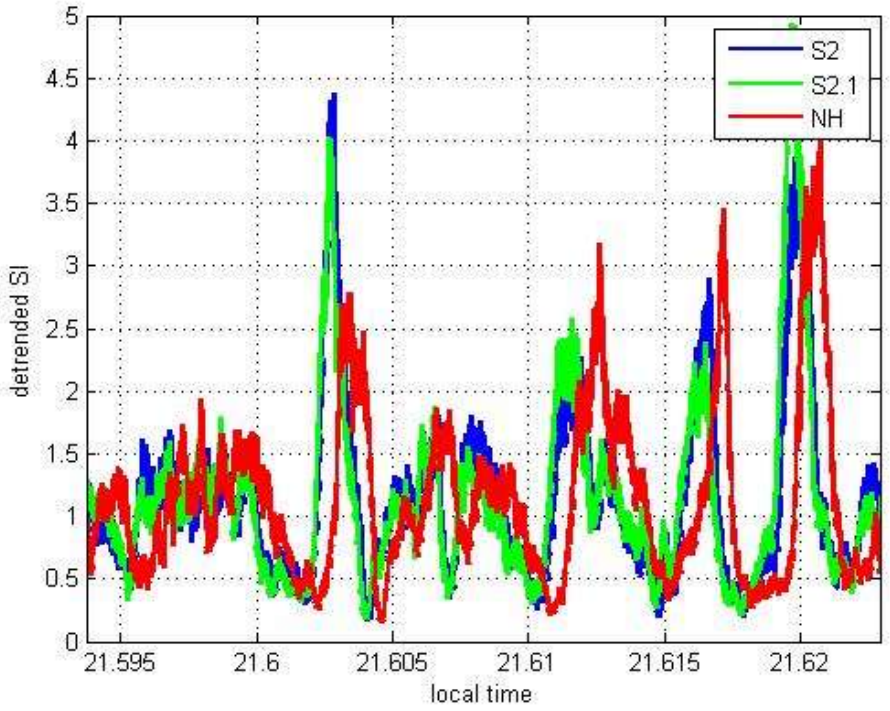

Figure 3-34 Detrended SI of satellite PRN 14

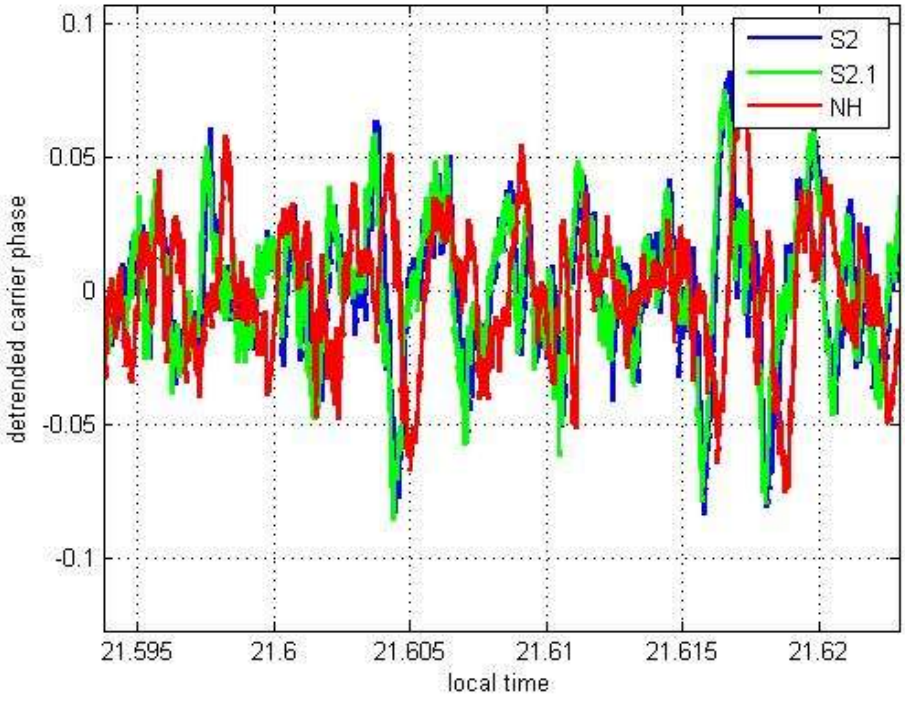

Figure 3-35 Detrended carrier phase of satellite PRN 14

Figure 3-36, Figure 3-37, and Figure 3-38 show the cross correlation result of SI at receiver S2.1 and S2, S2.1 and NH, S2 and NH respectively. SI is available at 50 Hz rate meaning that each unit of the time offset in the *x*-axis corresponds to 20 ms. The time delay shown by the obtained peak is displayed in each figure. The receiver at S2 is lagging by 14 time unit relative to receiver at S.1 which equals 0.28 s. The receiver at NH is lagging by 108 time unit (2.16 s) relative to receiver at S.1. The receiver at NH is lagging by 94 time unit (1.88 s) relative to receiver at S2.

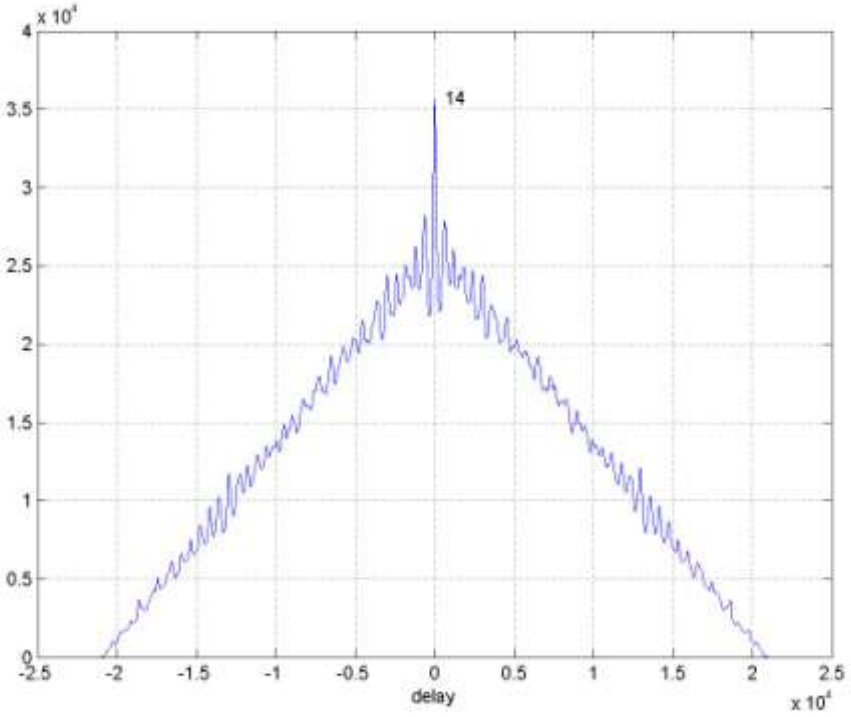

Figure 3-36 Cross correlation of detrended SI of PRN 14 at S2.1 and S2

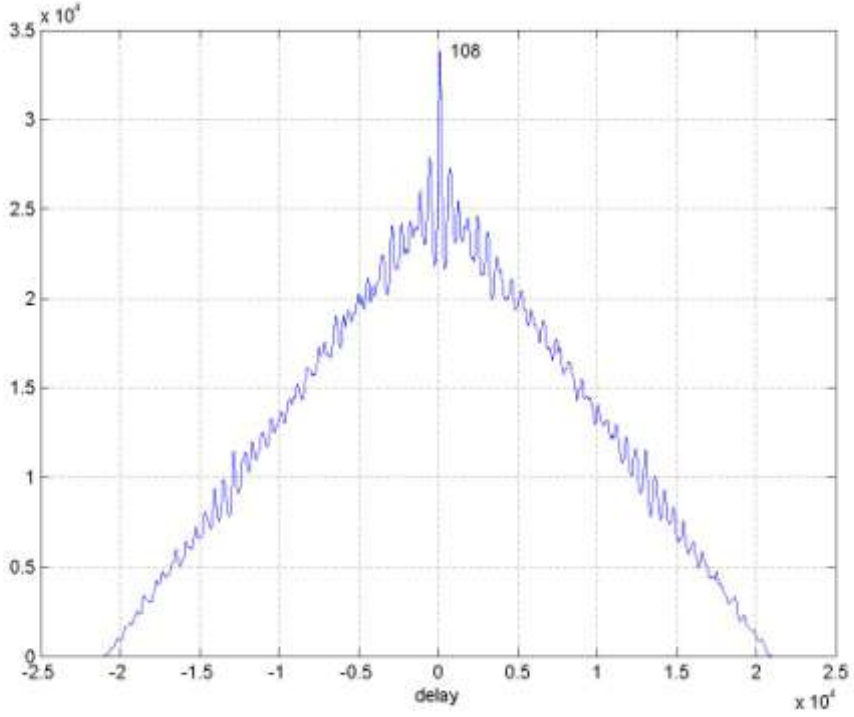

Figure 3-37 Cross correlation of detrended SI of PRN 14 at S2.1 and NH

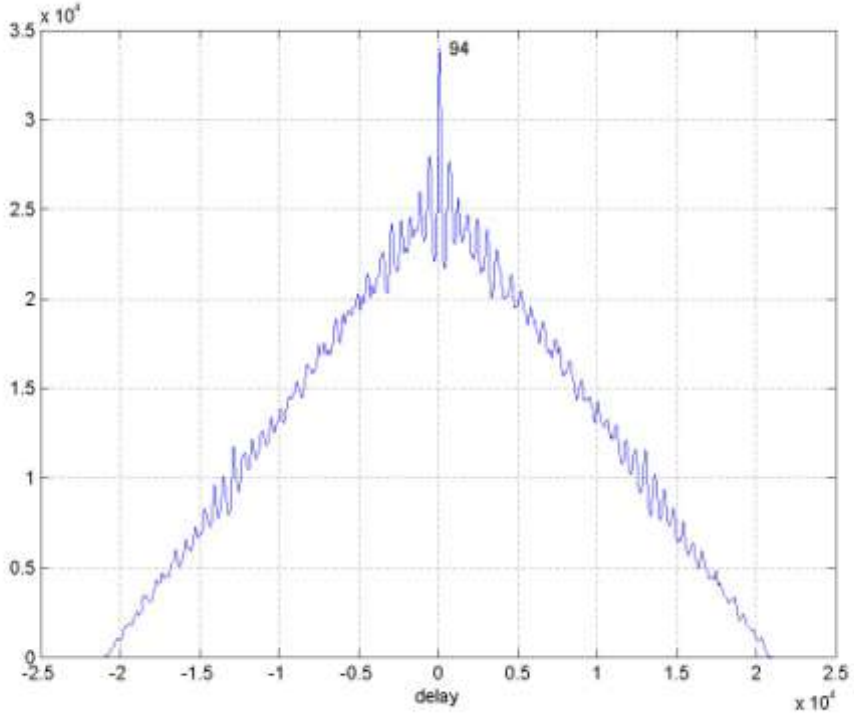

Figure 3-38 Cross correlation of detrended SI of PRN 14 at S2 and NH

Figure 3-39, Figure 3-40, and Figure 3-41 show the cross correlation result of detrended carrier phase at receiver S2.1 and S2, S2.1 and NH, S2 and NH respectively. Carrier phase is also available at 50 Hz rate, therefore each unit of the time delay in the figures corresponds to 20 ms. Based on this carrier phase cross correlation, the receiver at S2 is lagging by 14 unit time (0.28 s) relative to receiver at S.1. The receiver at NH is lagging by 100 unit time (2 s) relative to receiver at S.1. The receiver at NH is lagging by 85 unit time (1.7 s) relative to receiver at S2. This results is very close and consistent with the cross correlation of signal intensity.

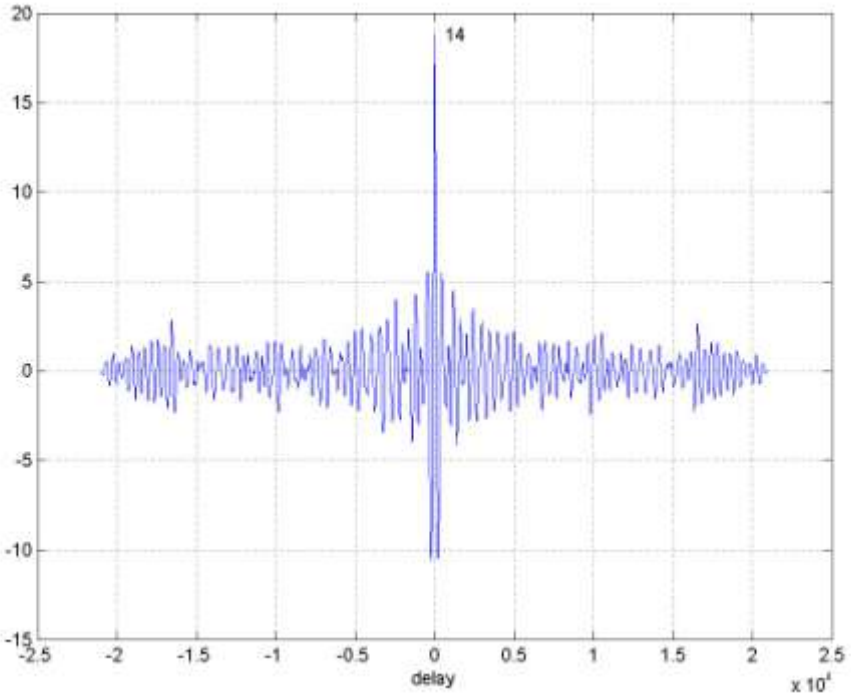

Figure 3-39 Cross correlation of detrended carrier phase of PRN 14 at S2.1 and S2

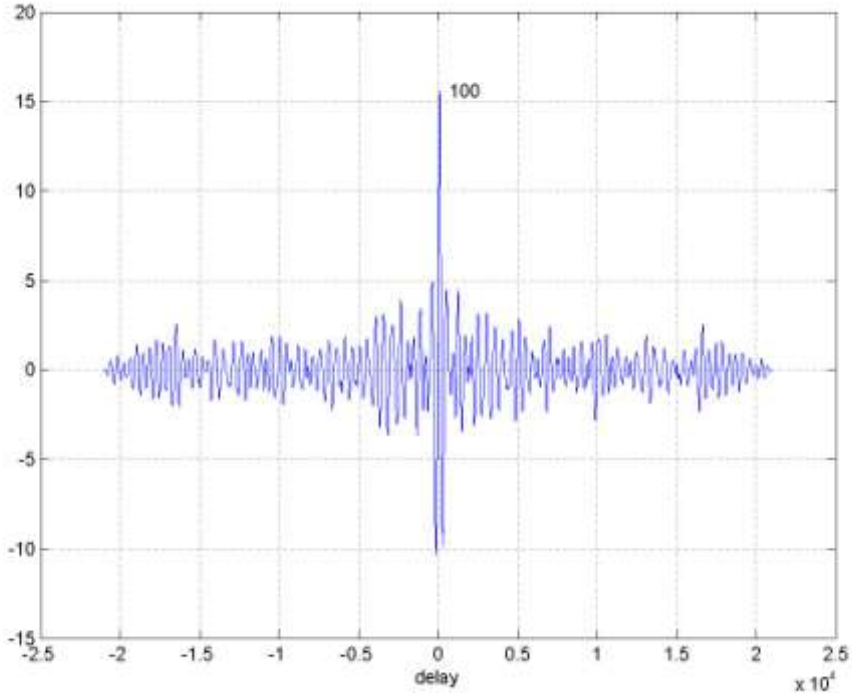

Figure 3-40 Cross correlation of detrended carrier phase of PRN 14 at S2.1 and NH

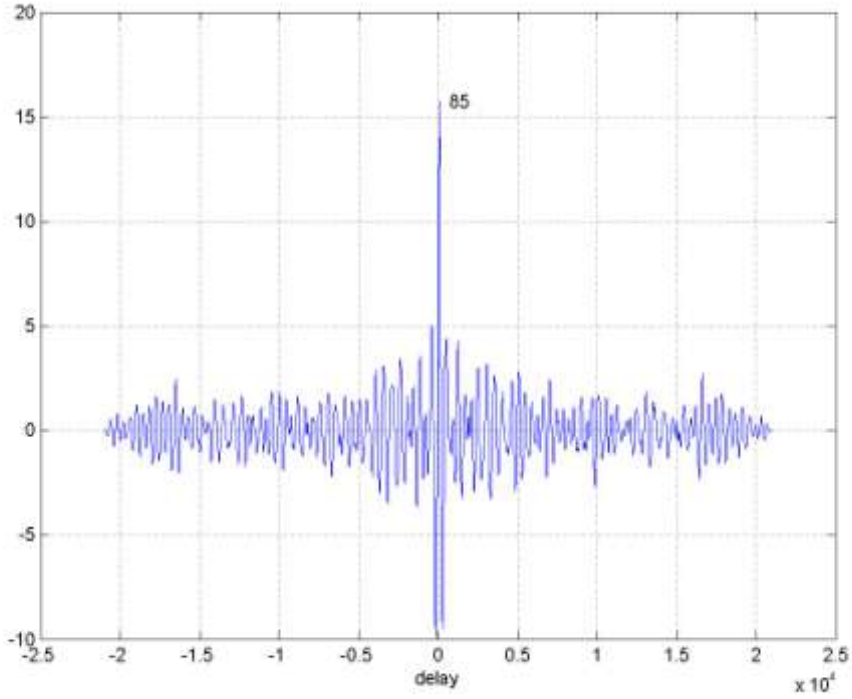

Figure 3-41 Cross correlation of detrended carrier phase of PRN 14 at S2 and NH

The cross correlation is also done for other satellites: PRN 18, 21, 25, 29 on the selected time period. The time lags indicated by the peak of cross correlation results are shown in the Table 3-9 with unit of 20 ms. The time lag between S2 and S2.1 are generally nearly zero. One possible reason is because those receivers are separated by only 80m distance. Besides that, it indicates irregularity drift does not have much component on north-south direction which is the relative direction between those two receivers as shown by the map in Figure 3-1. Significant time lag is obtained from the cross correlation between Nanyang House (NH) receiver with those in S2 and S2.1. The distance between NH and both S2 and S2.1 is around 1 km. This gives sufficient time lag to observe irregularities drift. Nanyang House is located in the north east direction of S2 and S2.1. Therefore, it can be concluded that the irregularity bubbles during scintillation drift toward east direction. Drift in north or south direction can be neglected as the time offset between S2 and S2.1 is nearly zero. This result differs with the work done at Wuhan in China [45] which stated that the irregularity drifts westward. But, it conforms to the result from [46], [47], [48] stating that during night ionosphere plasma drifts toward east.

Table 3-9 Delay of the cross correlation between receivers

		S2.1 and S2		S2.1 and NH		S2 and NH	
Day	PRN	SI	CP	SI	CP	SI	CP
20-9-2014	14	14	14	108	100	94	85
20-9-2014	18	0	2	NA	NA	NA	NA
20-9-2014	21	5	6	306	312	306	306
20-9-2014	25	1	2	494	495	494	491
20-9-2014	29	10	10	316	313	306	303

As seen in Table 3-9, the cross correlations of both detrended SI and carrier phase of satellite PRN 18 at NH with those at S2.1 and S2 is not available. The cross correlation results of them are shown in Figure 3-42 to Figure 3-45 which do not have distinct peak to show the time lag. One possible reason is that the irregularity between those locations is quite different which result in different SI fluctuation shown in Figure 3-46. This phenomenon is also observed in carrier phase shown in Figure 3-47. This suggests that within 1 km distance the bubble characteristic can change, causing different effect into SI and carrier phase fluctuation significantly. However, the cross correlation between S2 and S2.1 of the same satellite shows a distinct peak indicating similar bubble characteristic within 80 m distance.

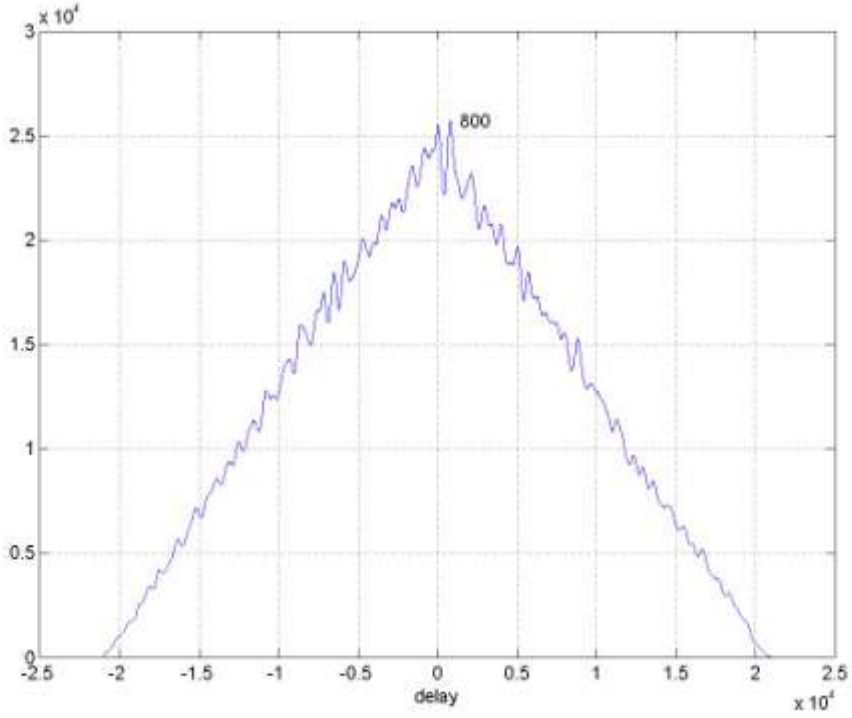

Figure 3-42 Cross correlation of detrended SI of PRN 18 at S2.1 and NH

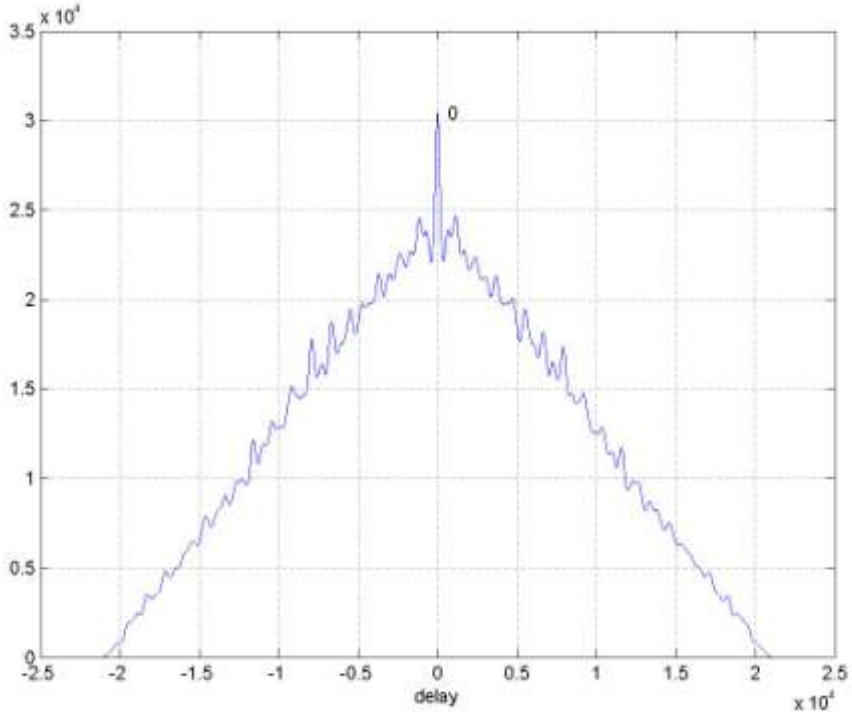

Figure 3-43 Cross correlation of detrended SI of PRN 18 at S2.1 and S2

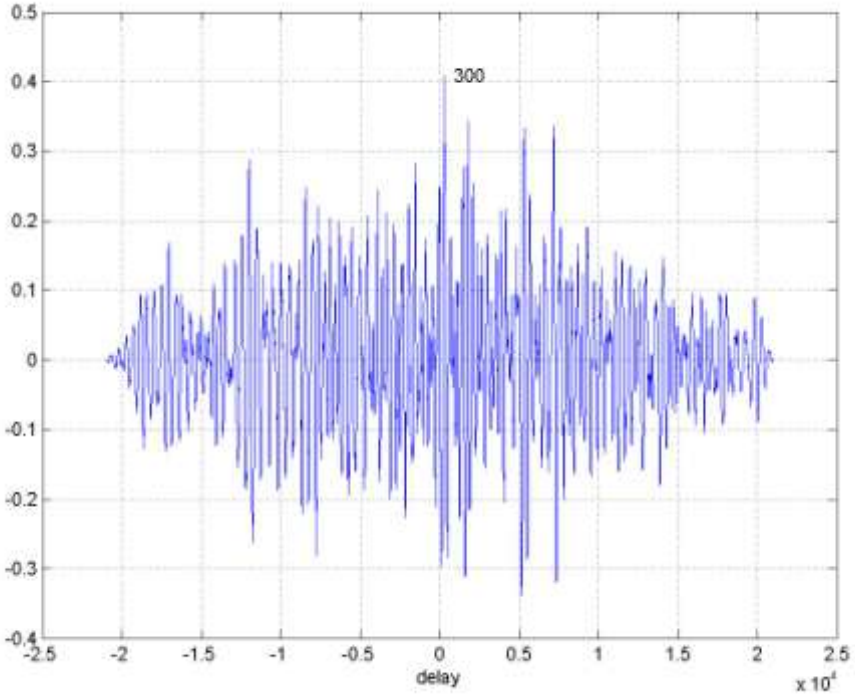

Figure 3-44 Cross correlation of detrended carrier phase of PRN 18 at S2.1 and NH

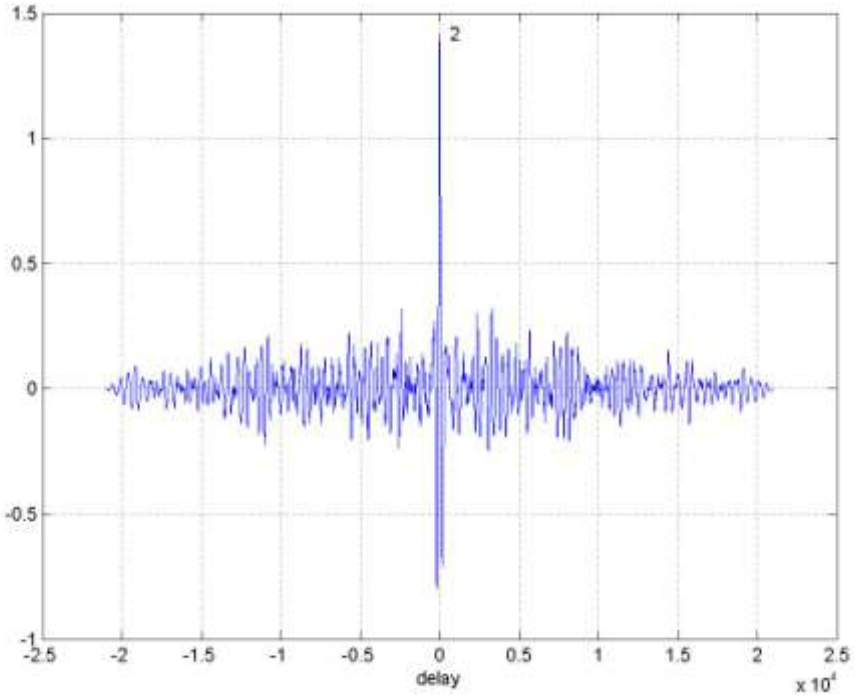

Figure 3-45 Cross correlation of detrended carrier phase of PRN 18 at S2.1 and S2

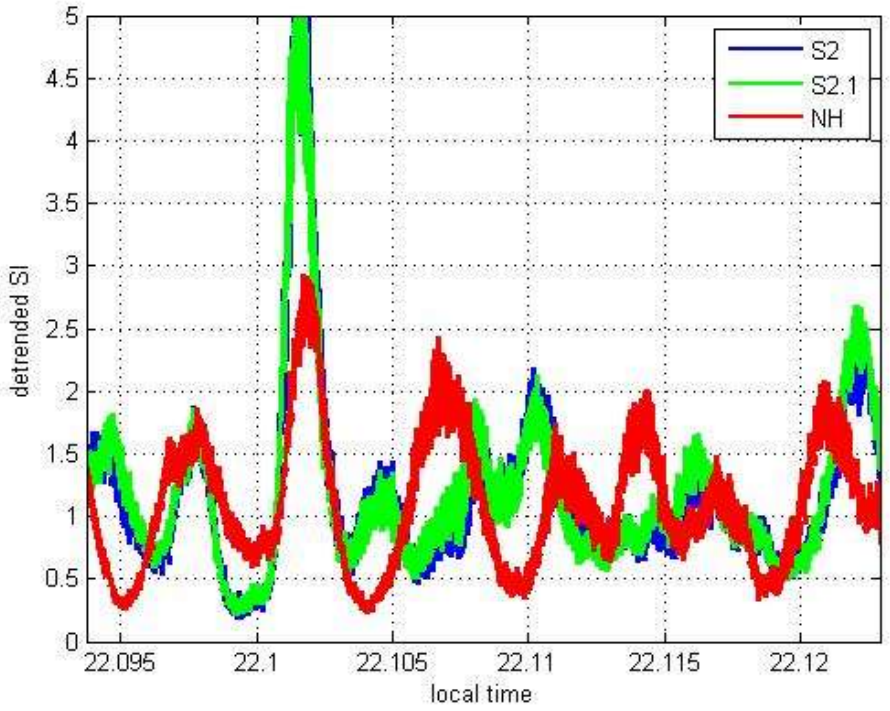

Figure 3-46 Detrended SI of PRN 18

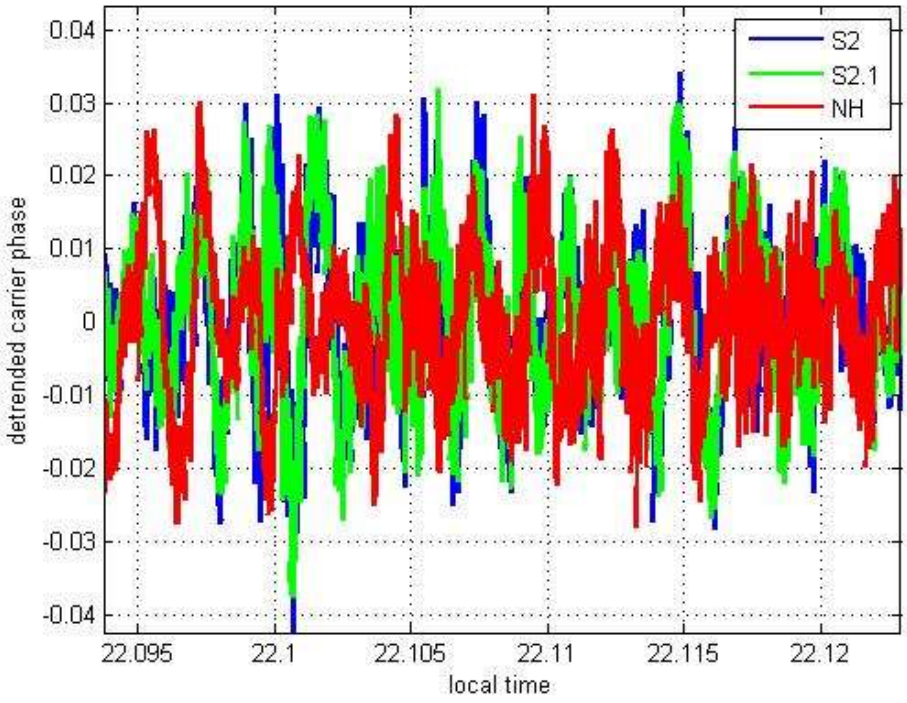

Figure 3-47 Detrended carrier phase of PRN 18

3.7. Ionospheric Scintillation Spatial Distribution

3.7.1. Multipath Data Omission

Before doing the sky plot of ionospheric scintillation for spatial distribution analysis, multipath effect need to be further omitted, especially to minimize the false observed scintillation in lower elevation angle. Multipath effect minimization has been done in the previous section by selecting data only to those that have elevation angle higher than 20 degree. However, this method is insufficient to eliminate the multipath effect. This effect is shown in the monthly S4 plot in Figure 3-48 and Figure 3-49 as diagonal pattern of higher S4 and standard deviation of the code over carrier divergence (SDCCD).

Variations in the code over carrier divergence, which is the measured difference between group delay and carrier phase advance, can be used to verify the existence of multipath. This is because the group delay tracking error due to multipath far exceeds carrier tracking errors due to multipath [20], [49]. Standard deviation of the code over carrier divergence (SDCCD) provided by Septentrio PolaRxS receiver is used here to indicate multipath. Receivers located at different locations may have different multipath effect due to different surrounding environment.

Monthly SDCCD, S4, phi60 and ROTI on March 2013 for satellite PRN 4 are plotted in Figure 3-48 to Figure 3-51 to show the multipath indication. Multipath effect is indicated by high SDCCD or S4 that happen every day at four minutes shifted time which is shown by the diagonal pattern of high SDCCD and S4 in Figure 3-48 and Figure 3-49 respectively. At those times satellite are located at the same direction from receiver and hence multipath effects by the same environment apply. Multipath effect is not observed in phi60 and ROTI as shown in Figure 3-50 and Figure 3-51. By applying this method for each satellite, the satellites affected by multipath are selected.

These multipath effects observation are done to the data of March and April 2013. Two groups of satellites are then selected. First is the group of satellites that are affected by multipath but having low S4, second group is those that have high S4 without multipath effect. S4 vs. SDCCD of these satellites are plotted in Figure 3-52. SDCCD is in the *y*-axis while S4 is in the x-axis. Satellites with multipath effect are red colored, satellites with high S4 without multipath are in green. Blue dots are the all

remaining satellites. The magenta line (y=1.3x+0.3) is obtained by visual observation to separate area of multipath effect (above line) and real scintillation (below line). Data indicated as multipath effect are than omitted from the analysis afterwards using this separating line.

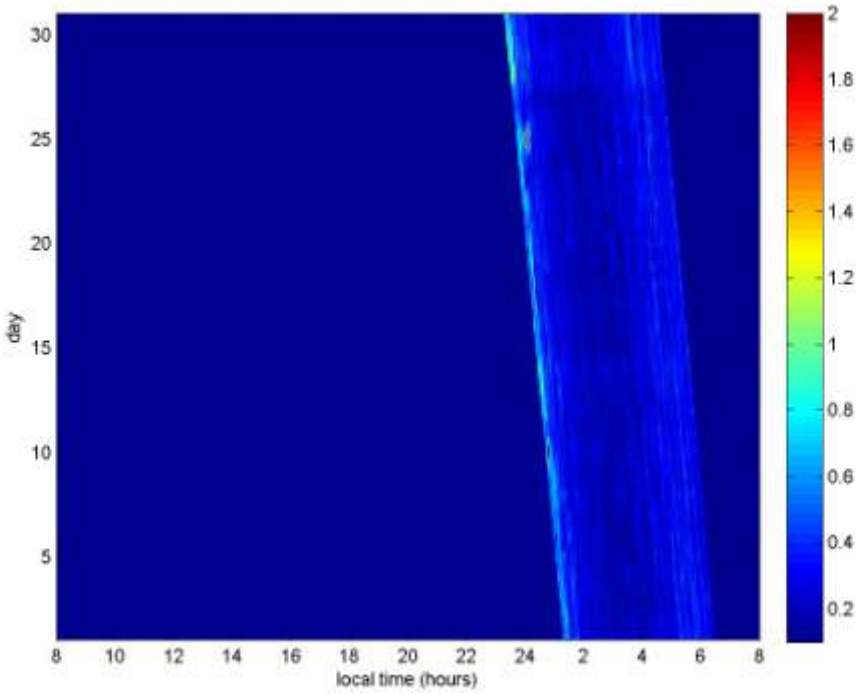

Figure 3-48 SDCCD on March 2013, PRN 4

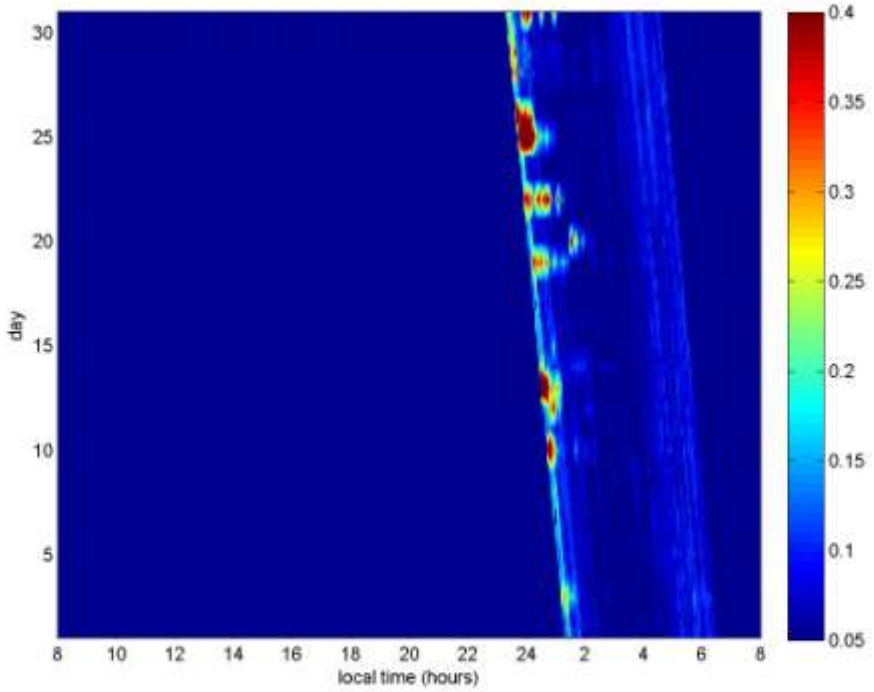

Figure 3-49 S4 on March 2013, PRN 4

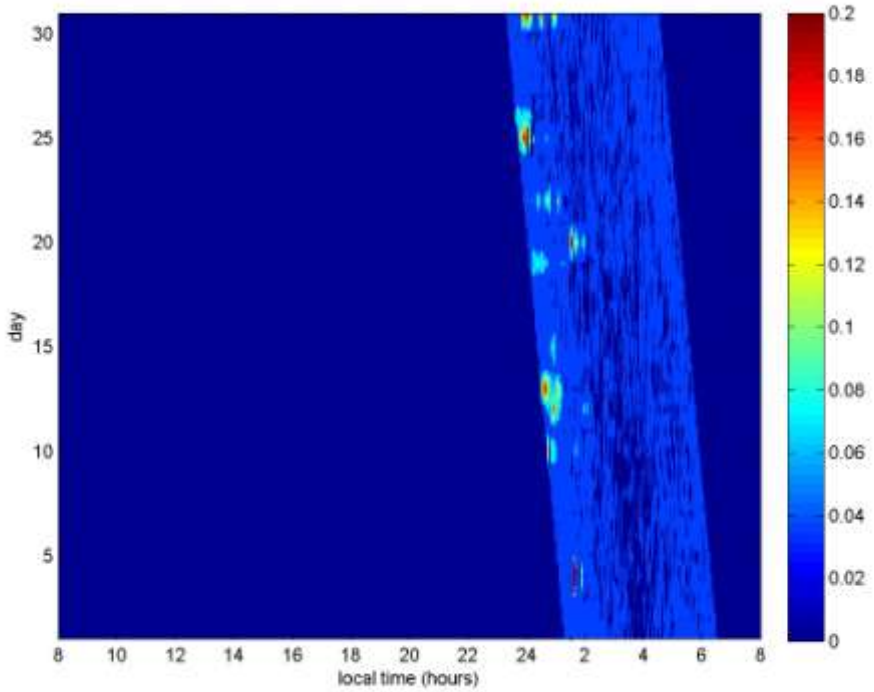

Figure 3-50 Phi60 on March 2013, PRN 4

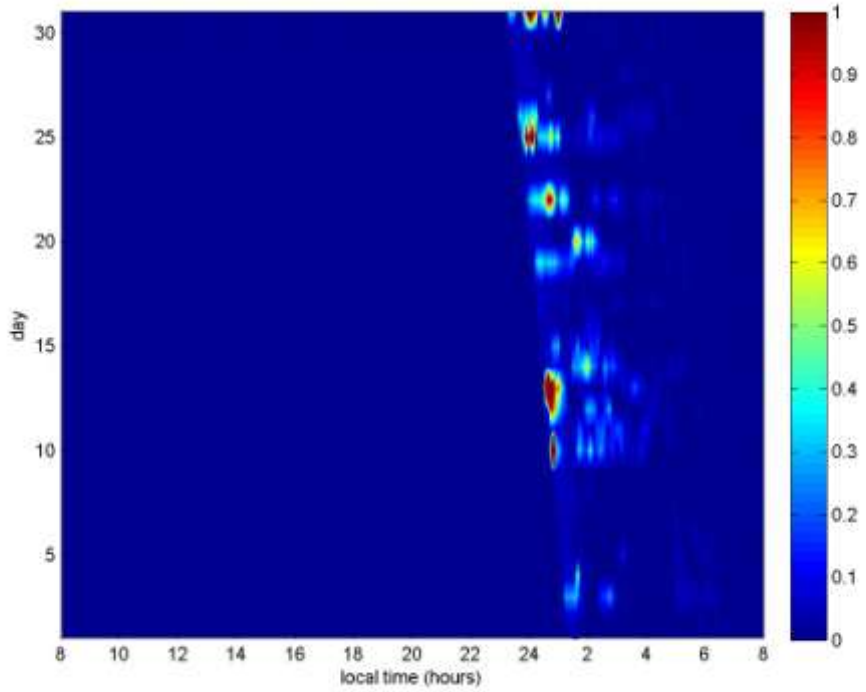

Figure 3-51 ROTI on March 2013, PRN 4

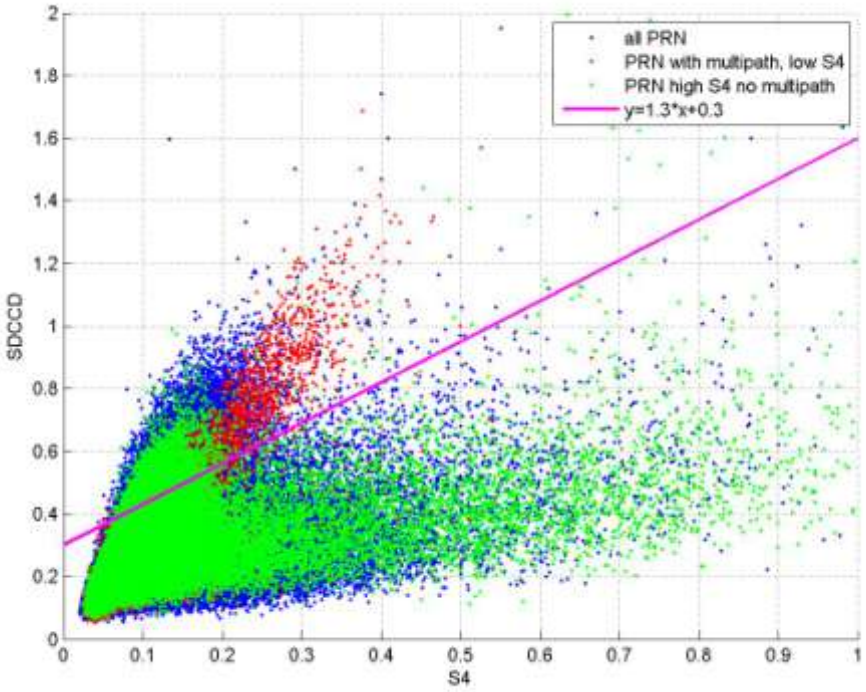

Figure 3-52 SDCCD vs. S4 on March and April 2013

Figure 3-53 and Figure 3-54 compare the S4 and SDCCD before and after the multipath effects omission. These data are taken on 15 and 16 March 2013 which are scintillation day and quiet day respectively. The left subplots show data before multipath removal, and the right subplots are after multipath removal. The S4 and SDCCD caused by multipath are shown by red colored dots in the left subfigures, while the blue dots represent the data without multipath. The left subfigures show the data including multipath, while the right subfigures show the data after multipath removal.

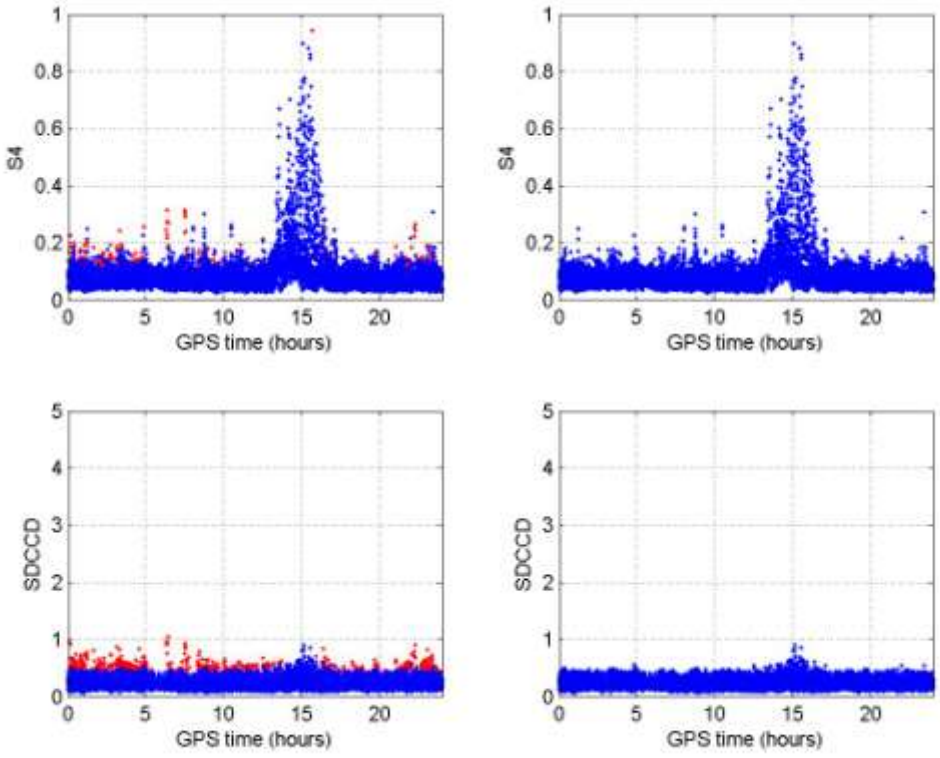

Figure 3-53 S4 and SDCCD on 15 March 2013 with multipath (left) and removed multipath (right)

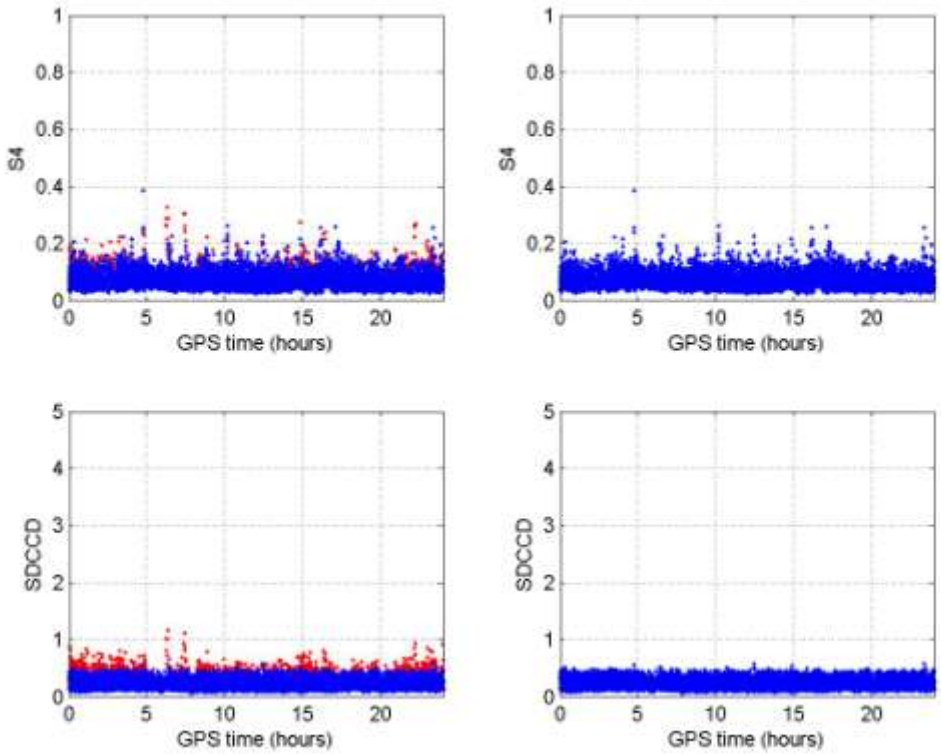

Figure 3-54 S4 and SDCCD on 16 March 2013 (left) and removed multipath (right)

Figure 3-55 and Figure 3-56 show the monthly S4 and SDCCD of satellite PRN 4 on March 2013 after multipath removal. The diagonal patterns of high S4 and SDCCD are much subtler here as compared to Figure 3-48 and Figure 3-49. Although these diagonal trends are still visible, they have much lower intensity compared to the pre-removal. Before multipath removal, the SDCCD diagonal trend reaches higher than 0.8 as shown by light blue colored line in Figure 3-48, while the S4 diagonal trend reaches higher than 0.2 shown by light blue to yellow colored line in Figure 3-49. After multipath removal, the remaining diagonal trends of SDCCD and S4 are negligible to scintillation analysis as they are very weak, lower than 0.5 and 0.15 respectively as shown by Figure 3-55 and Figure 3-56.

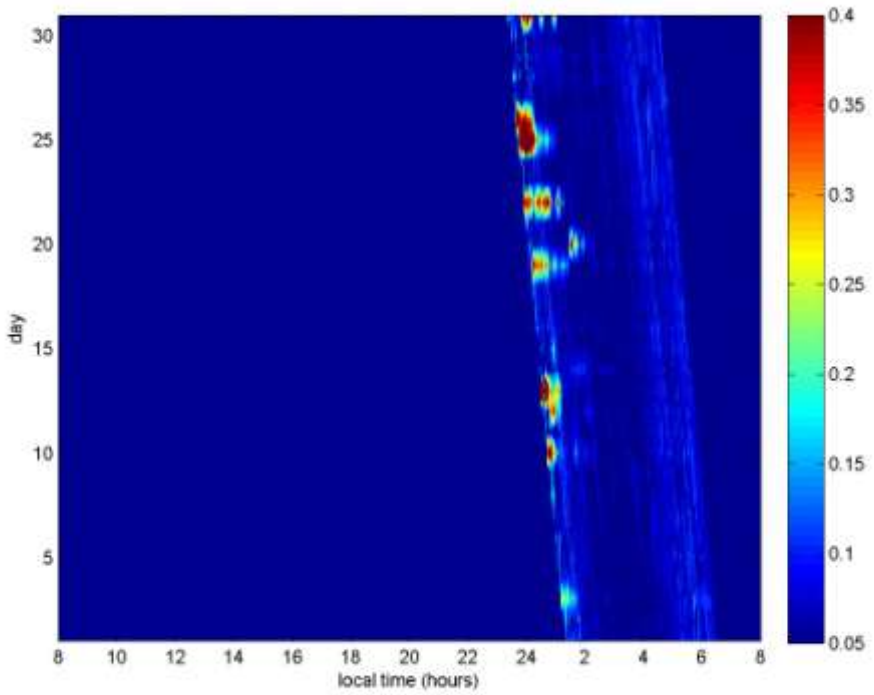

Figure 3-55 S4 on March 2013, PRN 4 after multipath removal

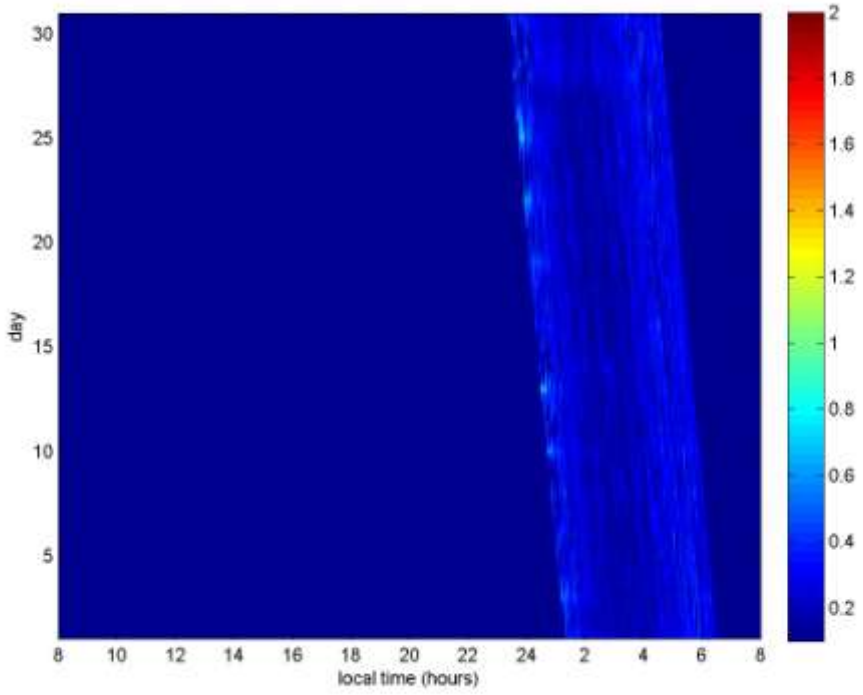

Figure 3-56 SDCCD on March 2013, PRN 4 after multipath removal

To further investigate the multipath properties in this particular receiver environment we also plotted the SDCCD with respect to azimuth and elevation angle of the satellites as done in [50]. Data in month of January, February, June, July, August, November, and December of year 2013 are chosen due to their relatively quiet ionospheric behavior.

Figure 3-57 shows the azimuth–elevation map of SDCCD averaged over this period before the multipath filtering. High SDCCD value which indicate high multipath is observed at around azimuth 210^0 and 240^0 both at low elevation angle around 20^0-25^0. The same SDCCD plot after multipath omission is shown in Figure 3-58. Here, the aforementioned multipath activities are no longer observed. Overall the multipath filtering process reduces the multipath affected data, although at lower elevation angle the observed SDDCD is generally higher than those at higher elevation angle which is naturally happens due to signal reflection by earth surface.

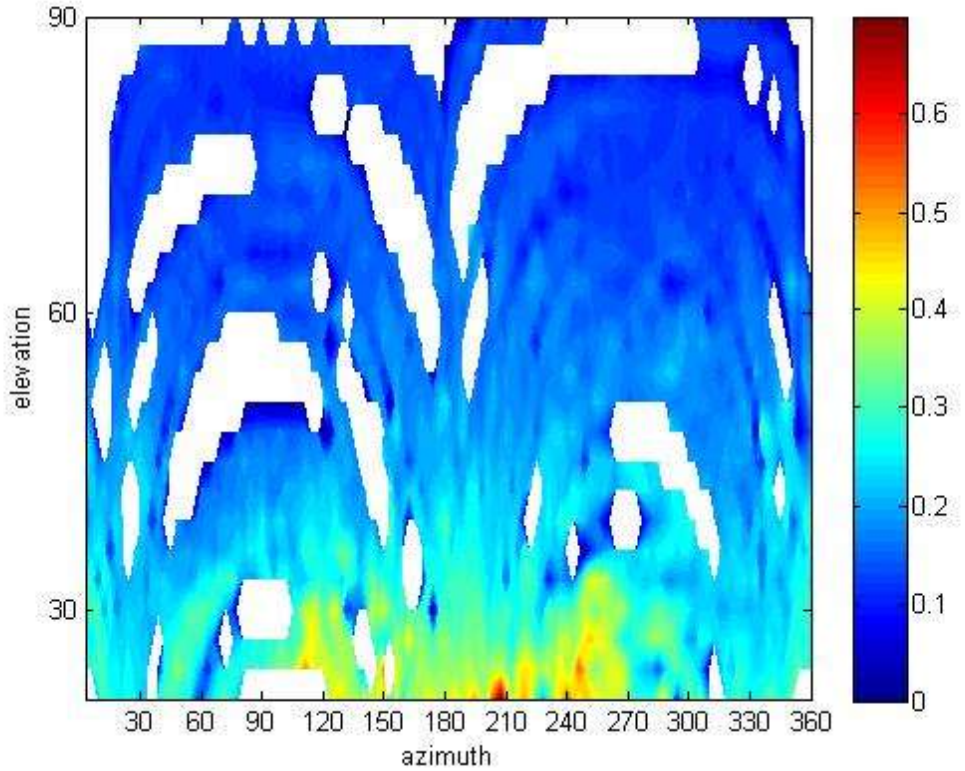

Figure 3-57 Azimuth–elevation map of SDCCD averaged over the quiet months of 2013

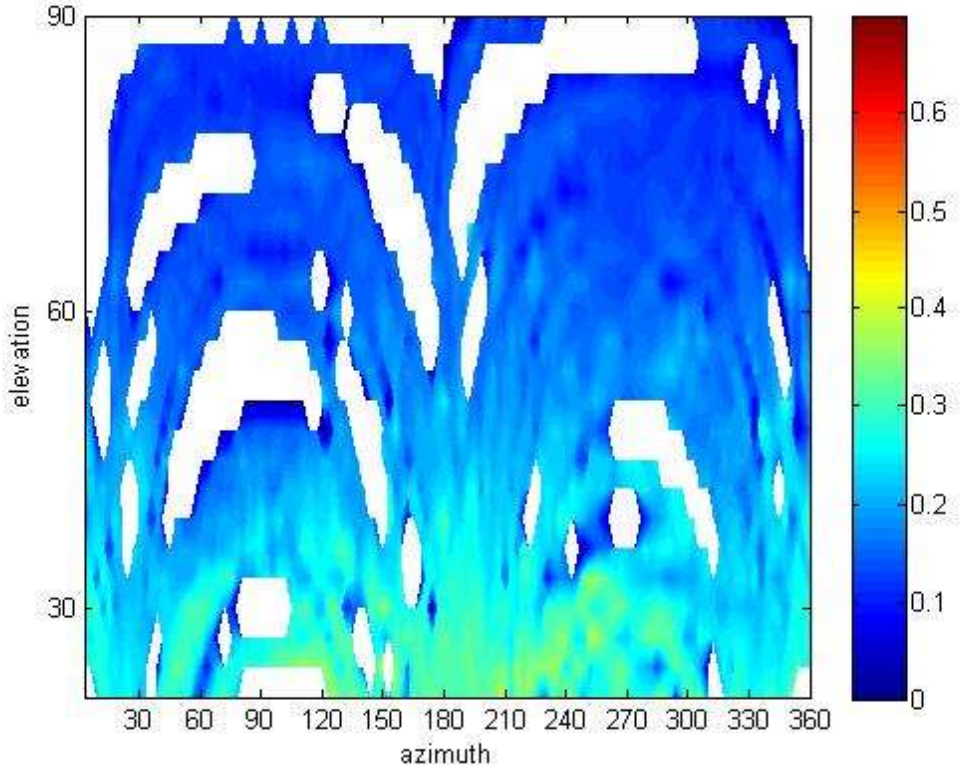

Figure 3-58 Azimuth–elevation map of SDCCD averaged over the quiet months of 2013 after multipath omission

3.7.2. Ionospheric Scintillation Sky Plot

We analyze the spatial distribution of scintillation occurrences by using sky plot based on the geographic longitude and latitude similar as the works previously done in Norway and Antarctica [53][54]. Scintillation intensity depends on the background electron density [51]. The electron density distribution has significant latitudinal variation, especially around the EIA region. Because the electron density in the crest of EIA region is higher than the magnetic equator, higher scintillation occurrence is expected to be higher also around the crest.

In this section GPS data are used. S4, phi60, and ROTI skyplot on equinox months of year 2013 are presented in Figure 3-59 to Figure 3-61. The ionosphere over Singapore is divided into bins of latitude and longitude with resolution of two degree. Those scintillation parameters are then averaged in each bin. The *x*-axis shows the

geographic longitude (E) where the ionosphere is projected into while *y*-axis shows the geographic latitude.

Figure 3-59 shows the spatial distribution or the skyplot of S4 over Singapore. Higher S4 is observed in the south part of the observed ionosphere. This is because the crest of EIA is located in the south of Singapore. S4 is also higher in the west compared to the east part. This is due to the fact that generally plasma bubbles are tilted westward as they vertically develop, which is due to vertical shear in the eastward plasma drift in the F region [52], [53]. This result agrees with previous observation in Bandung, Indonesia which is also near the EIA region [32]. It also observed that S4 in the north is slightly higher than the center region. This is due to the remaining multipath effect that is failed to be filtered. Another possible reason is that in lower elevation angle the thickness of the ionosphere that GPS signal traverses through increases which also increases the magnitude of its perturbation [54].

Figure 3-60 and Figure 3-61 show the spatial distribution of phi60 and ROTI respectively. They show similar pattern as S4 whose scintillations are concentrated in the south part of the sky. Scintillations in the west are also generally higher than the east ones. Phi60 and ROTI do not show higher magnitude in the north part which is shown by S4 skyplot. As presented in the previous section, multipath does not have significant effect to phi60 and ROTI. Besides, this may indicate that phase scintillation is not affected by the variation of elevation angle and thickness of the ionosphere layer that the signal passing through. ROTI is also not affected by variation in elevation angle as vertical TEC is used in the calculation instead of slant TEC.

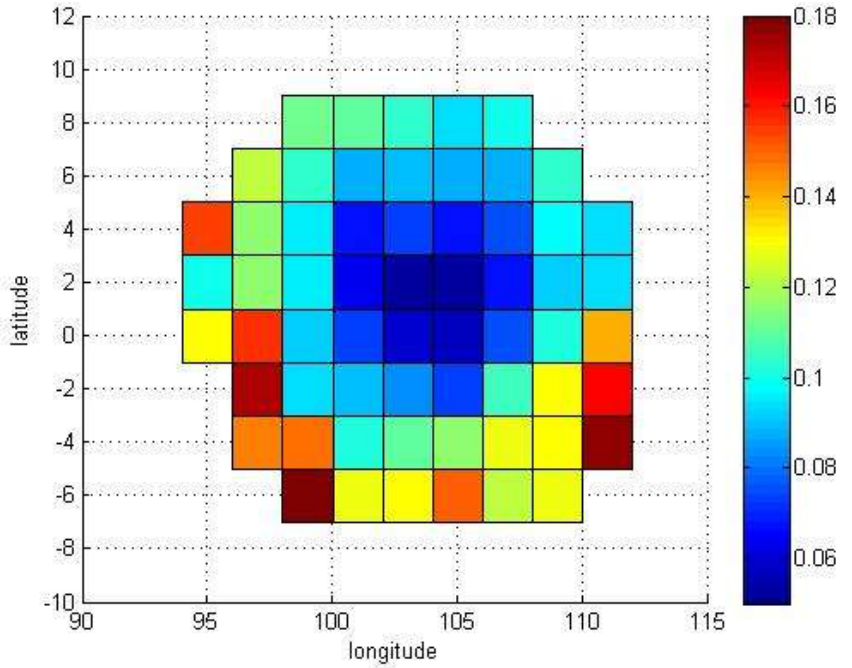

Figure 3-59 S4 GPS spatial distribution on equinox 2013

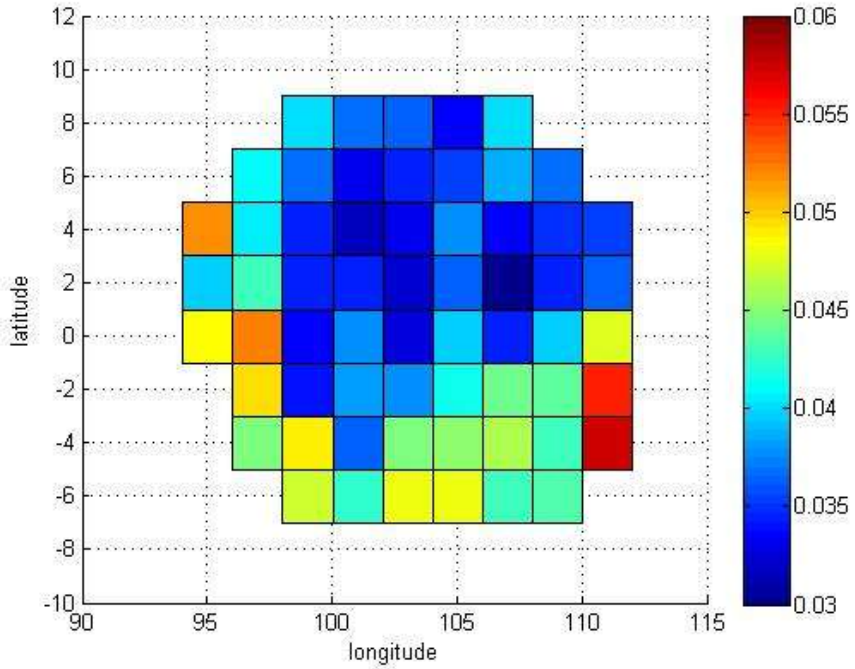

Figure 3-60 Phi60 GPS spatial distribution on equinox 2013

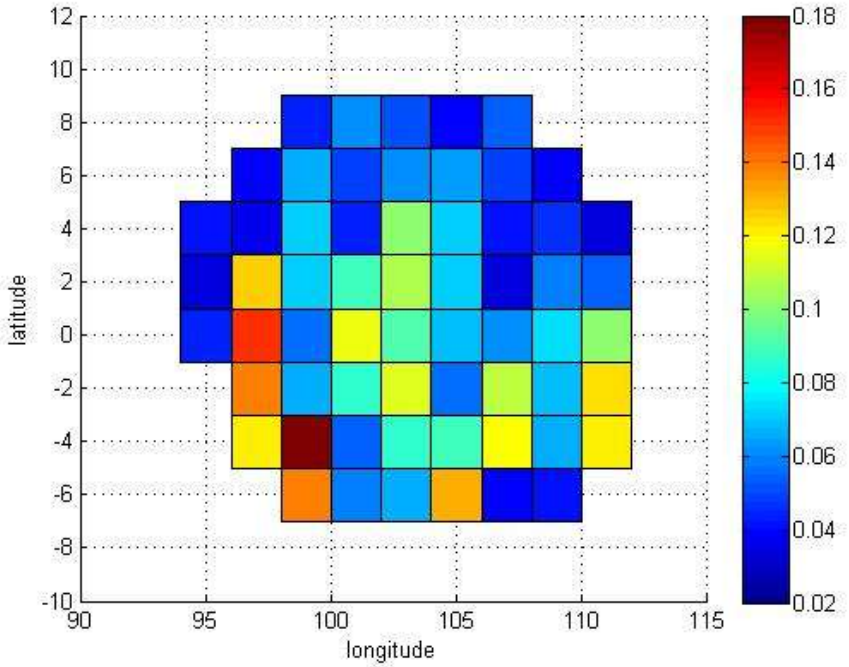

Figure 3-61 ROTI GPS spatial distribution on equinox 2013

3.7.3. Scintillation Latitudinal and Temporal Distribution

The distribution of scintillation with respect to latitudinal and daily hour variation is analyzed. Figure 3-62, Figure 3-63, and Figure 3-64 show the plot for S4, phi60, and ROTI respectively. The *x*-axis indicates universal time (UT) with resolution of 1 hour while the *y*-axis is geographic latitude with resolution of 1 degree. The objective of this method is to study the effect of daily temporal variation to the latitudinal variation of scintillation skyplot.

Similarly to the previous skyplot, higher ionospheric scintillation is observed in the south part of Singapore sky. There is also higher S4 also in the north part which is not observed in phi60 and ROTI as presented in the previous section. For all latitudes, significant scintillation generally happen at the same time around 13.00-17.00 UT or 21.00-01.00 LT. This concludes that daily temporal variation does not have significant effect to the latitudinal variation of scintillation.

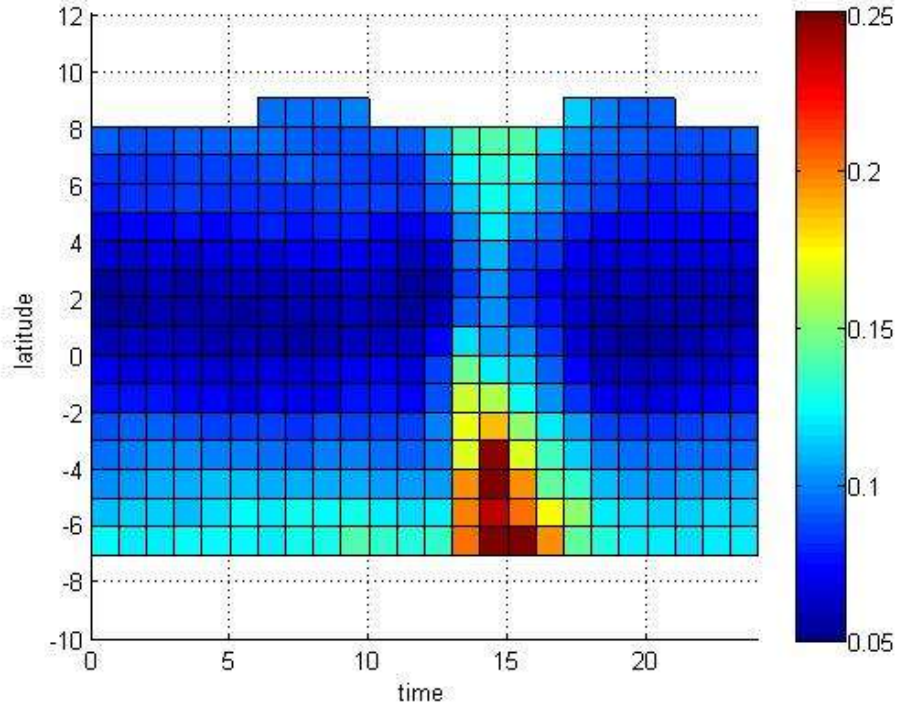

Figure 3-62 GPS S4 latitudinal and temporal variation

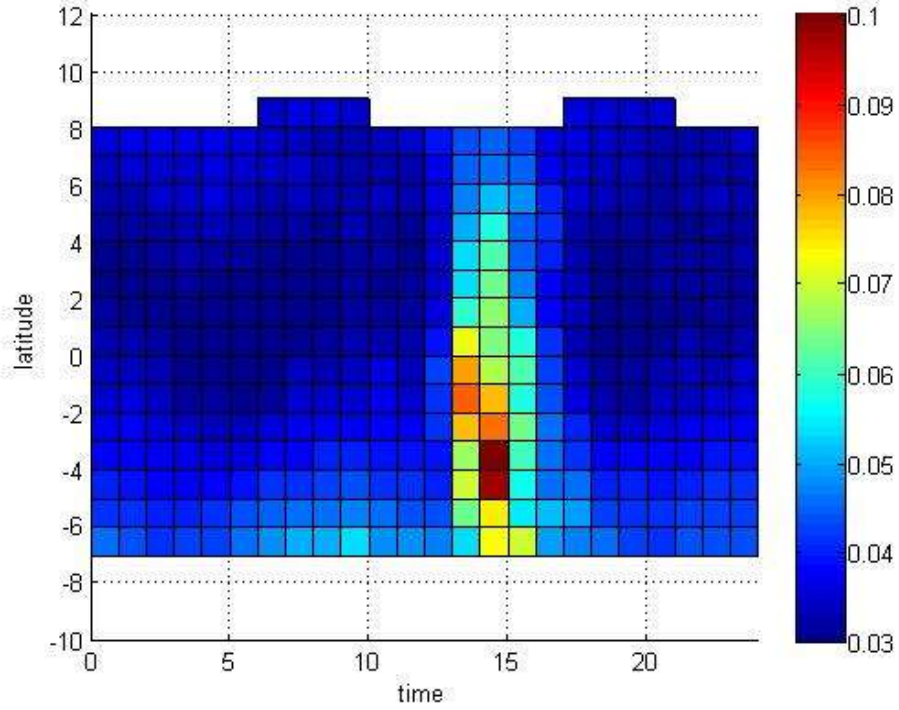

Figure 3-63 GPS Phi60 latitudinal and temporal variation

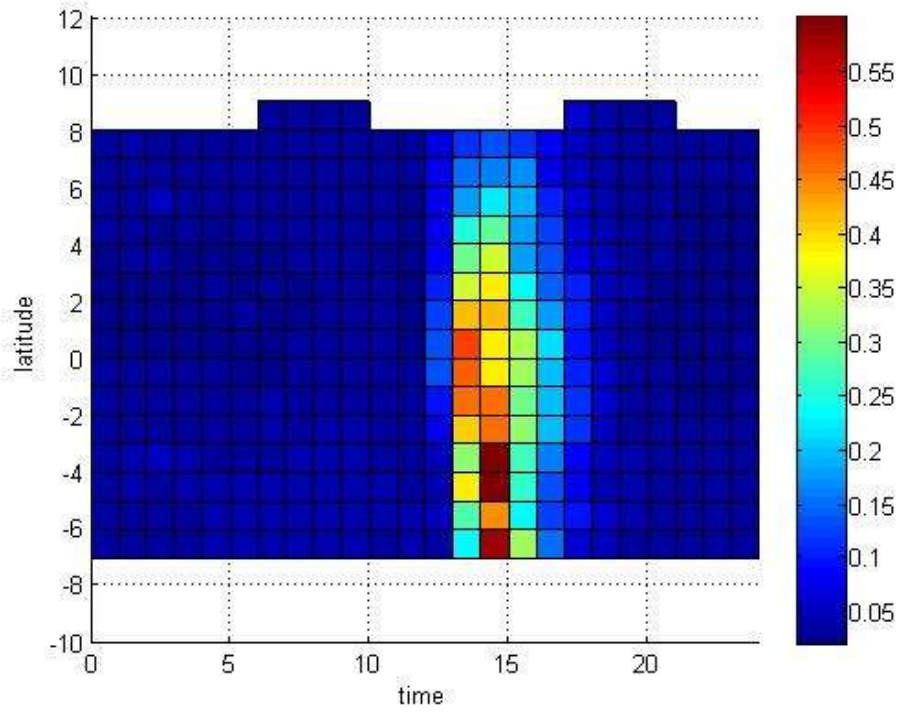

Figure 3-64 GPS ROTI latitudinal and temporal variation

3.7.4. Scintillation Longitudinal and Temporal Distribution

In this section the distribution of ionospheric scintillation with respect to the longitudinal and daily time variation is analyzed. Figure 3-65, Figure 3-66, and Figure 3-67 show the plot for S4, phi60, and ROTI respectively. The *x*-axis indicates universal time (UT) with resolution of 1 hour while the *y*-axis is geographic eastward longitude (E) with 1 degree resolution. The objective of this method is to study the effect of daily time to the longitudinal variation of scintillation.

It is observed that generally scintillations are higher in the west part of the sky which is indicated by lower longitude degree. There is slightly higher S4 also in the most east part, probably due to remaining multipath effect and longer signal path effect in lower elevation angle. For phi60 and ROTI there is no high scintillation observed in the east part because phi60 and ROTI is less affected by multipath and elevation angle variation.

For all longitude, significant scintillation generally happen at the same time around 13-17 UT or 21-01 LT. There is no significant longitudinal variation in the scintillation time. However, it is weakly observed that scintillations happen slightly earlier in the east at around 12 UT. This behavior is seen more clearly in phi60 and ROTI than S4 due to low elevation effect on S4. This time variation is caused by different time zone between east and west. East time is earlier than west time which results in earlier scintillation occurrences also.

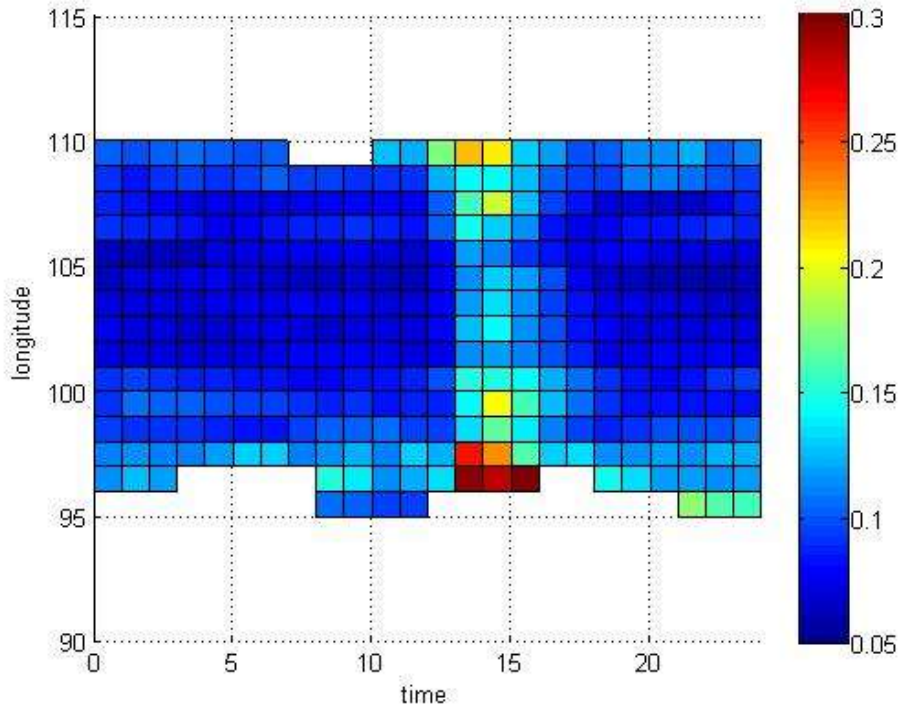

Figure 3-65 GPS S4 longitudinal and temporal variation

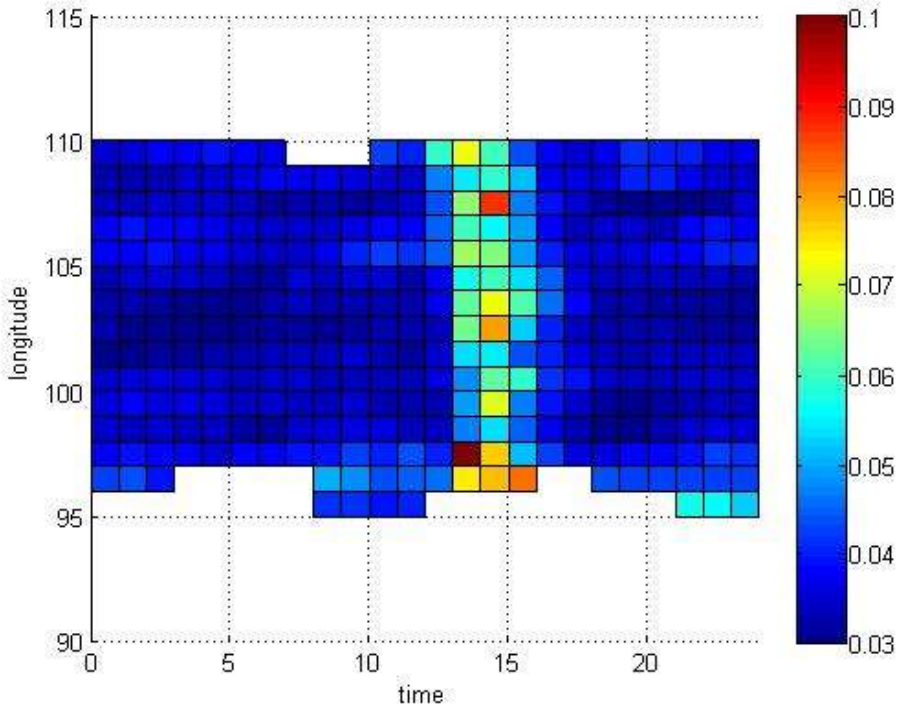

Figure 3-66 GPS Phi60 longitudinal and temporal variation

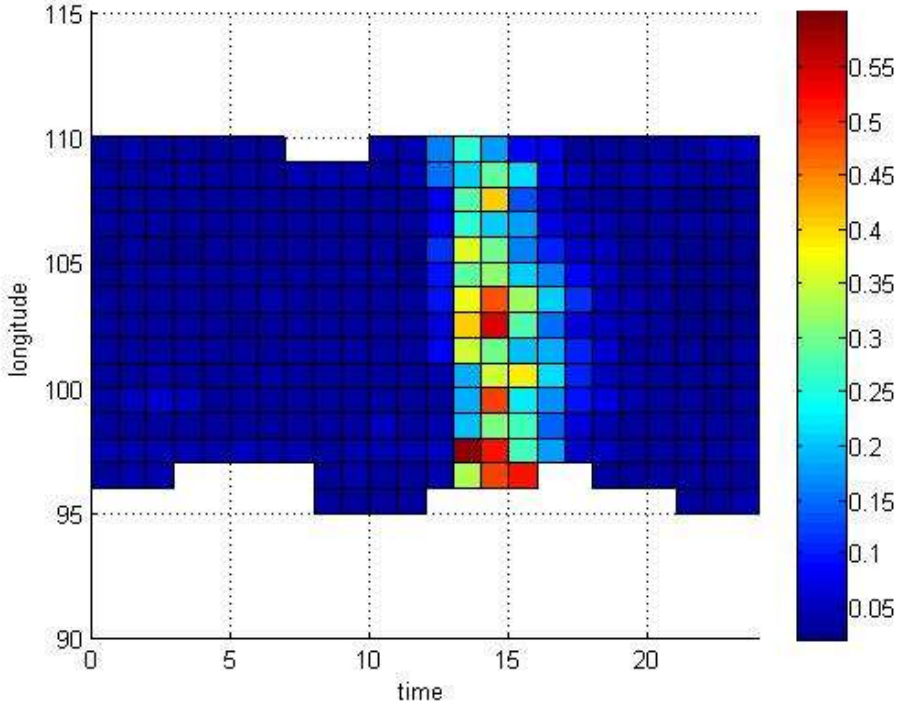

Figure 3-67 GPS ROTI longitudinal and temporal variation

3.8. Correlation with Solar Activity

3.8.1. Effect of Solar Activity in Long Term Observation

Ionization activity in ionosphere is highly affected by the radiation of sun. Therefore, solar activity is presented here to observe the relation of it to ionosphere scintillation in few years period. The sunspot number (SSN) is a commonly used index to represent solar activity.

Sunspots are temporary phenomena on the photosphere of the Sun that appear visibly as dark spots compared to surrounding regions. They are caused by intense magnetic activity, which inhibits convection, forming areas of reduced surface temperature. They usually appear as pairs, with each sunspot having the opposite magnetic pole to the other. Although they are at temperatures of roughly 3000-4500 K, the contrast with the surrounding material at about 5780 K leaves them clearly visible as dark spots [55].

The SSN is an index of the activity of the entire visible disk of the Sun. It is determined each day without reference to preceding days. Each isolated cluster of sunspots is termed a sunspot group, and it may consist of one or a large number of distinct spots with various sizes. The SSN is defined as

$$SSN = K\,(10g + s) \qquad \textbf{(3-4)}$$

where g is the number of sunspot groups and s is the total number of distinct spots. The scale factor K depends on the observer and is intended to effect the conversion to the scale [55].

Figure 3-68 shows the monthly mean of sunspot number from year 1975 to mid of 2014 provided by National Geophysical Data Center (NGDC) which is available in www.ngdc.noaa.gov. The *x*-axis represent the time in monthly resolution, while the *y*-axis is the monthly averaged SSN. It is clearly seen that the solar activity has certain cycle with a period of around 11-12 years. Year 1980, 1991, 2002, and 2014 are around the peak solar activity period while year 1976, 1986, 1997, and 2009 are the minimum solar activity years.

Besides sunspot number, solar radio flux is also used to indicate solar activity. The solar flux used here is the daily measurements of the integrated emission from the

solar disc at 2800 MHz (10.7cm wavelength) provided by National Research Council of Canada (NRCC). The data are taken in Penticton, at local noon. The flux values are expressed in solar flux units (sfu); 1 sfu = 10^{-22} $W.m^{-2}Hz^{-1}$. Figure 3-69 shows the monthly mean of solar radio flux during the same period as the SSN plot. The *x*-axis represent the time in monthly resolution, while the *y*-axis is the monthly averaged solar flux. The solar flux has the same pattern as SSN showing that year 1980, 1991, 2002, and 2014 are around the peak solar activity period while year 1976, 1986, 1997, and 2009 are the minimum solar activity years.

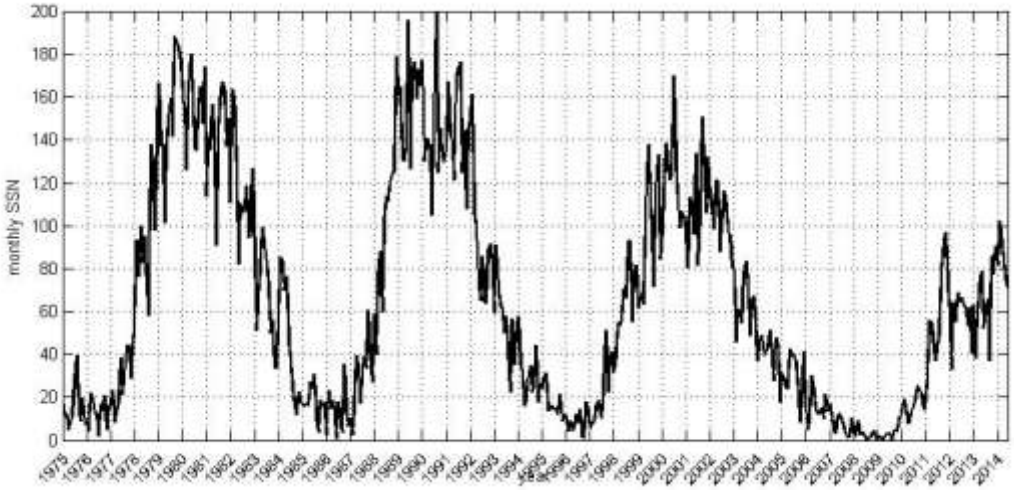

Figure 3-68 Monthly mean Sunspot Number in January 1975 – June 2014

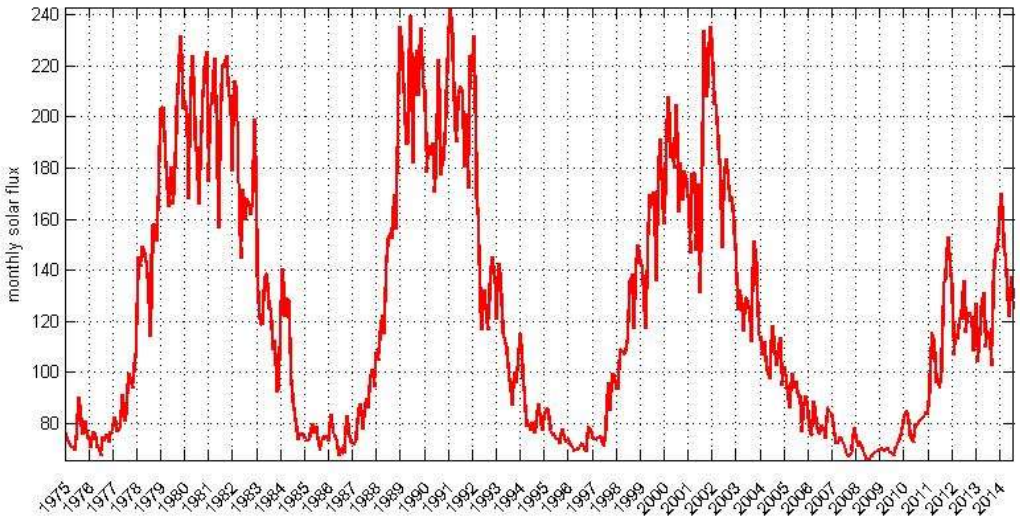

Figure 3-69 Monthly mean Solar Flux in January 1975 – June 2014

Figure 3-70 (a) to (j) shows the mean of S4 during equinox months (April and September) in year 2009 to 2013 obtained from IGS at NTUS station. The *y* and *x* axes for each subplot represent the day (1^{st} to 30^{th} or 31^{st}) and local time (8 a.m. to 8 a.m. next day) in each month. Note that in year 2009, August data is used as the September data is not available.

This S4 pattern correlates well with the solar activity shown by sunspot number and solar radio flux. In 2009, during minimum solar activity there is not ionospheric scintillation observed. From 2010 to 2013 ionospheric scintillation is increasingly occurring. The reason behind this phenomenon is because ionization in earth atmosphere is mainly caused by energy radiation from the sun. The higher the ionization activity, the higher is the chance of ionospheric scintillation. This observation is consistent with previous works done at Cambridge (52^0N 0^0E) which is in mid latitude zone [56].

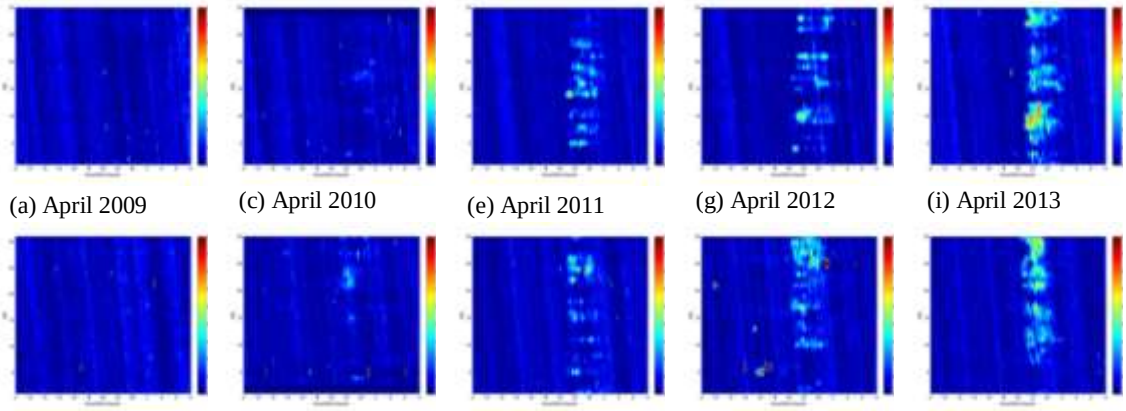

(a) April 2009 (c) April 2010 (e) April 2011 (g) April 2012 (i) April 2013

(b) August 2009 (d) September 2010 (f) September 2011 (h) September 2012 (j) September 2013

Figure 3-70 Average S4 during equinox in year 2009 to 2013

3.8.2. Effect of Solar Activity in Daily Observation

The effect of solar activities onto ionospheric scintillation is studied further in daily basis. Daily sunspot number (SSN) and solar flux during equinox months are plotted. The daily average TEC and S4 on those months are then also plotted to see the correlation of them.

Figure 3-71 to Figure 3-74 show the solar activity and its effect on ionosphere vTEC and S4 during equinox months of year 2013. Each figure constitutes of four subplots, the subplot (a) shows sunspot number and solar flux, the subplot (b) is the average of vTEC obtained from all visible satellites on each day. The subplot (c) shows the average of S4 in the day, while subplot (d) shows the occurrence of S4>0.2 in each day. The *x*-axis of the figures indicates the day.

It is clearly observed that SSN and solar flux show very similar trend which indicate solar activity. The vTEC also shows similar trend as solar activity. It further proves that sun activity is the main cause of ionization in ionosphere. However, no obvious pattern is shown by S4 that is related to solar activity. On April 2014, S4 seems to have similar trend as solar activity and TEC, but it is not shown on other equinox months. This behavior indicates that the level of ionosphere ionization is not the only factor that affects ionospheric scintillation. There are other factors also such as geomagnetic activity that is presented in the next section and the randomness factor of the irregularities initiation by Rayleigh-Taylor mechanism.

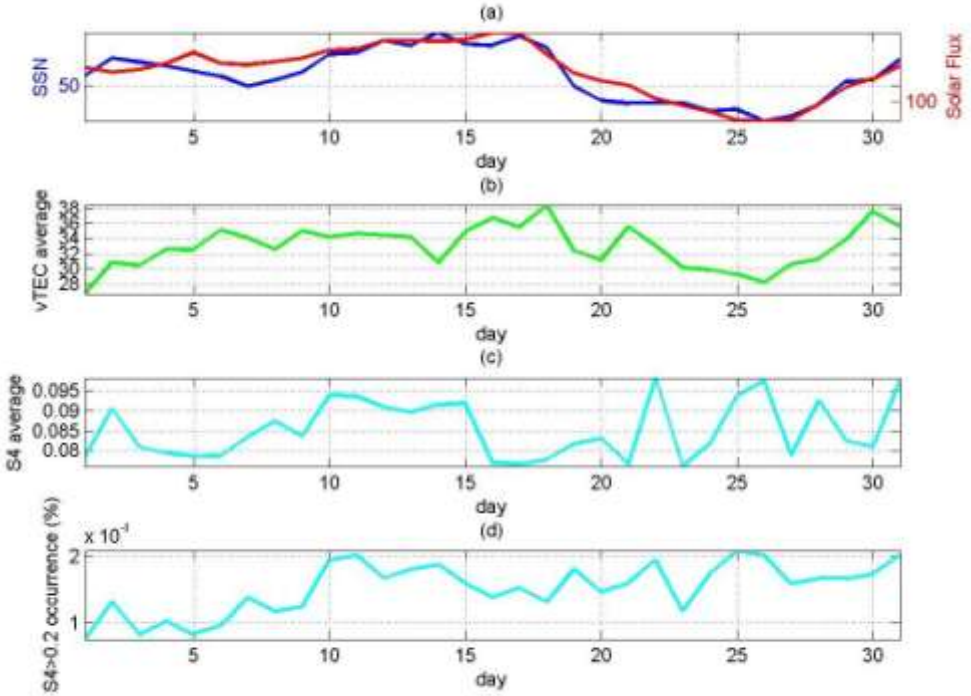

Figure 3-71 Solar and ionosphere activities on March 2013

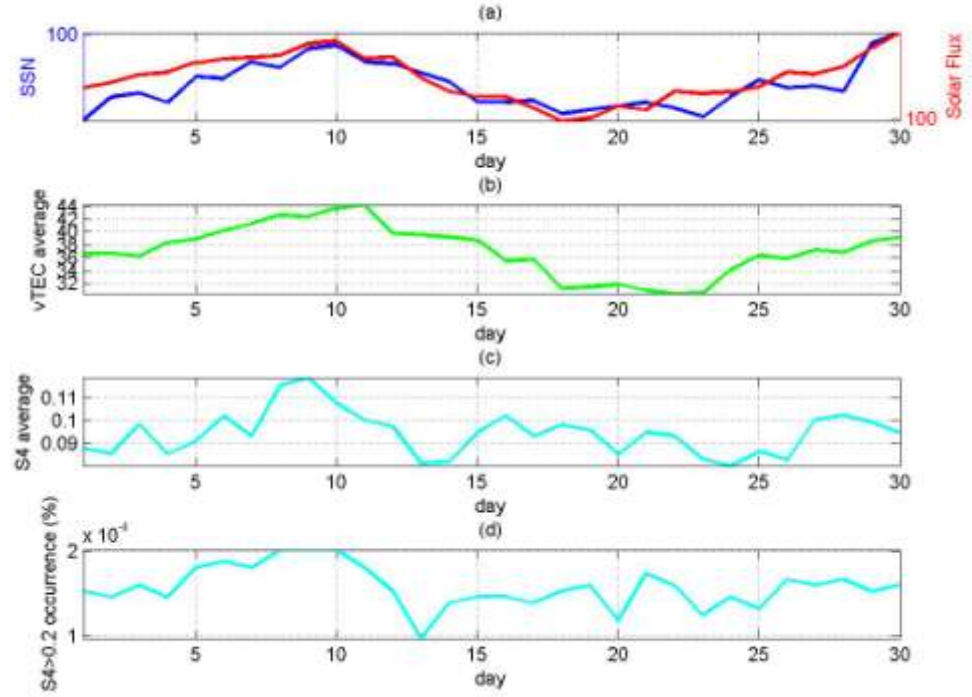

Figure 3-72 Solar and ionosphere activities on April 2013

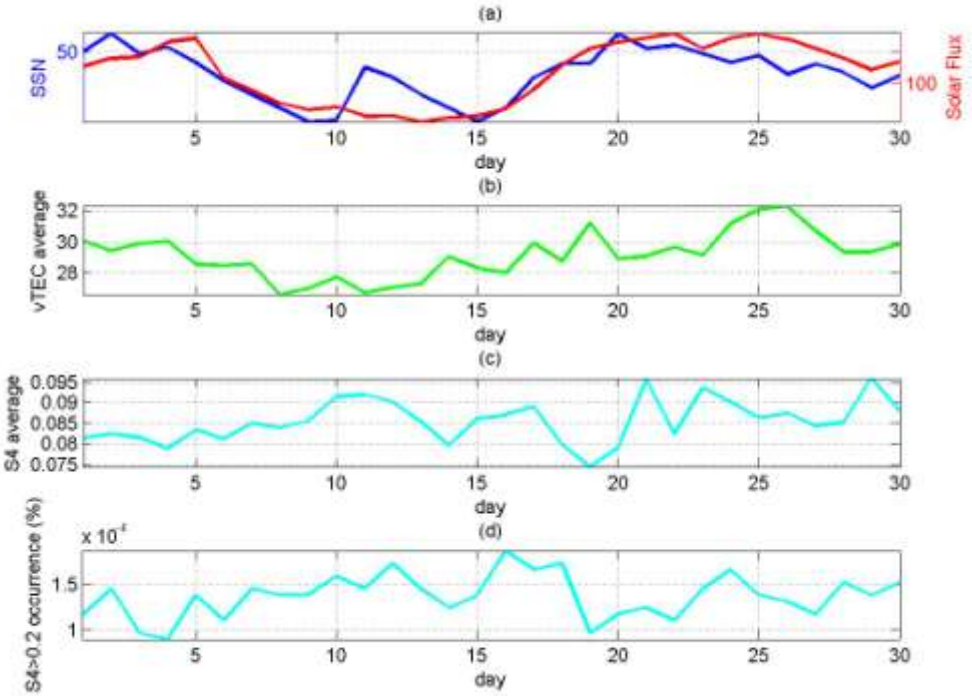

Figure 3-73 Solar and ionosphere activities on September 2013

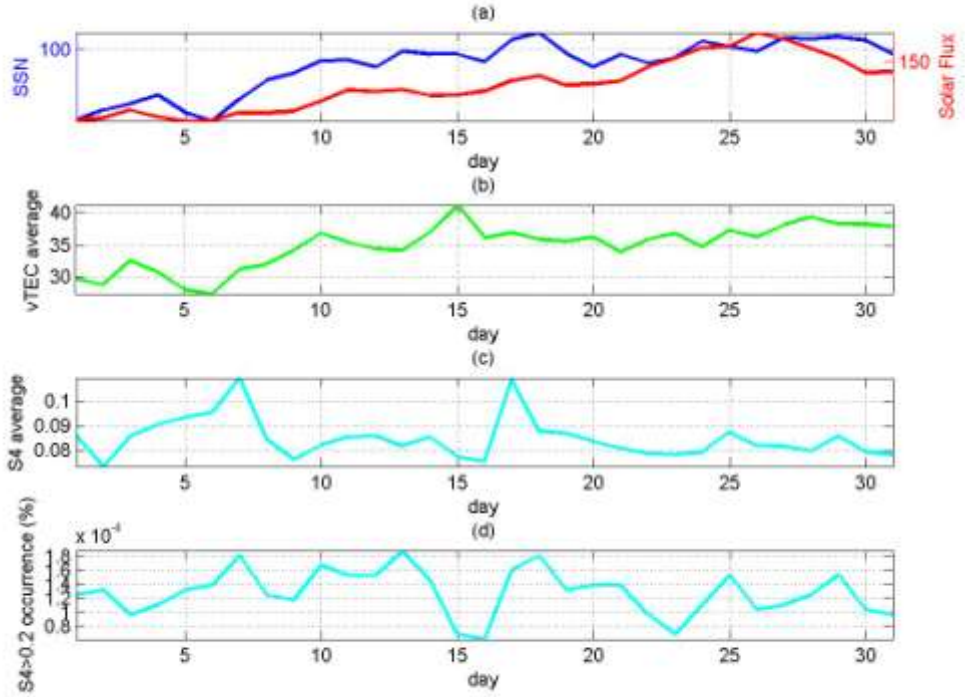

Figure 3-74 Solar and ionosphere activities on October 2013

3.9. Effect of Geomagnetic Disturbance

Geomagnetic field has an important role on ionospheric scintillation in equatorial region. Geomagnetic field coupled with eastward electric field constitute the vertical force ***E x B*** that lifts the ionosphere plasma in equatorial region forming equatorial ionization anomaly (EIA). This vertical lift also causes plasma density imbalance between top and bottom layer which is also the primary factor in triggering plasma bubble irregularities.

Geomagnetic field sometimes get disturbance which is caused by solar wind or solar magnetic activity. This section discuses the effect of such geomagnetic disturbance on the variation of ionospheric scintillation. Observation is done on the equinox months of year 2013. In each month, five days are selected for both geomagnetic quiet and disturbed conditions. The selection of such days is provided by

http://www.ga.gov.au/oracle/geomag/iqd_form.jsp which uses Kp-index as the tool to indicate geomagnetic disturbance.

Figure 3-75 to Figure 3-78 compare the average S4 on geomagnetic quiet days and disturbed days during equinox months of year 2013. The *y*-axis shows the S4, while the *x*-axis shows the universal time (UT). The S4 during quiet days indicated by blue lines are generally higher than those observed during disturbed days indicated by red lines. This behavior is shown in all of the equinox months: March, April, September, and October.

During geomagnetic disturbed days, dynamo electric fields opposing the normal ionospheric electric field are generated. This phenomena cause reduction in the post-sunset rise of the F-layer plasma in equatorial region which consequently, reducing the probability of scintillation occurrences [57]. Work done in India [42] and [58] also reported that there is a suppression of ionospheric scintillation during disturbed days.

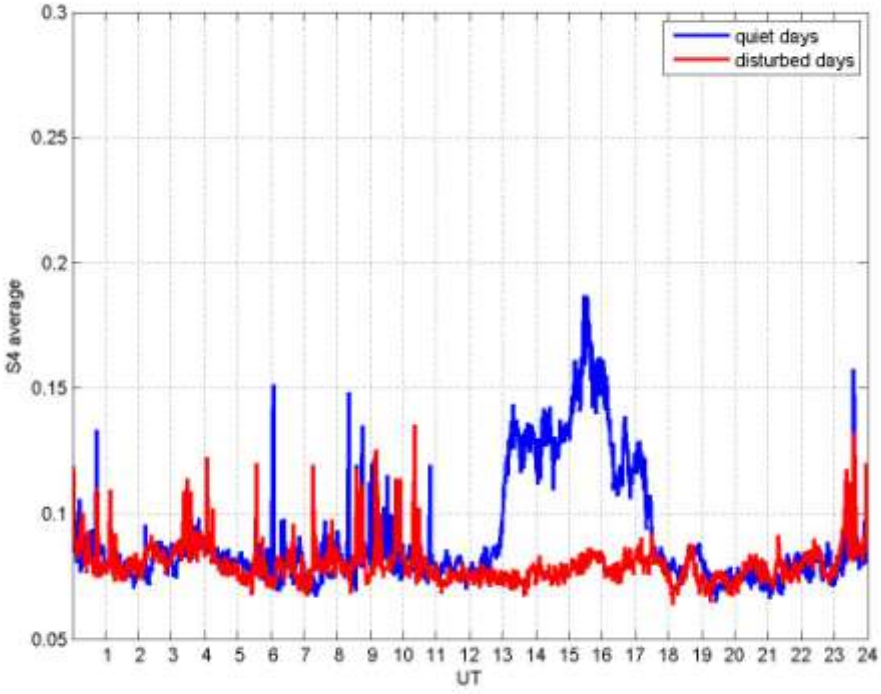

Figure 3-75 S4 average during magnetic quiet and disturbed days on March 2013

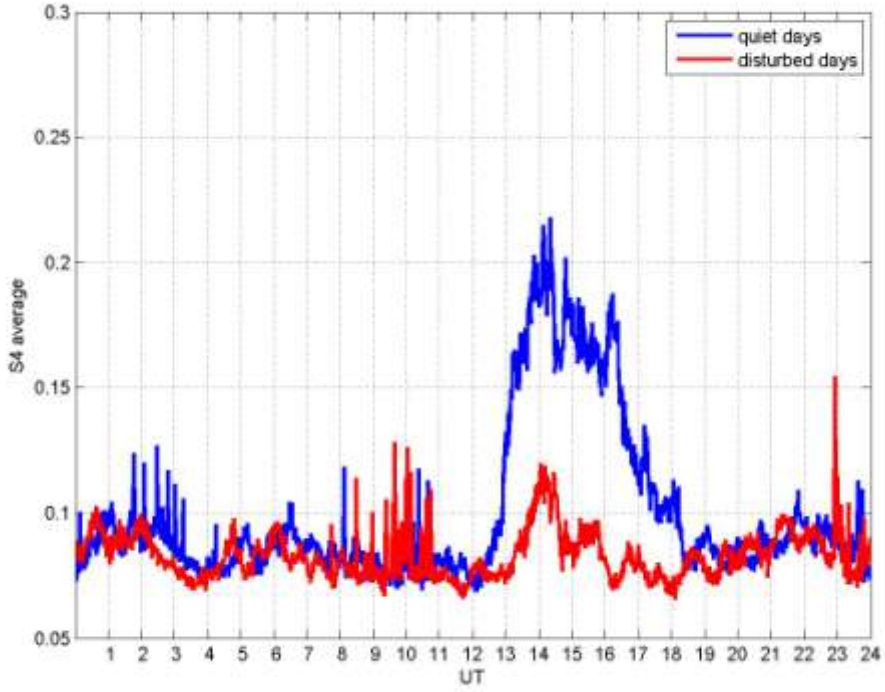

Figure 3-76 S4 average during magnetic quiet and disturbed days on April 2013

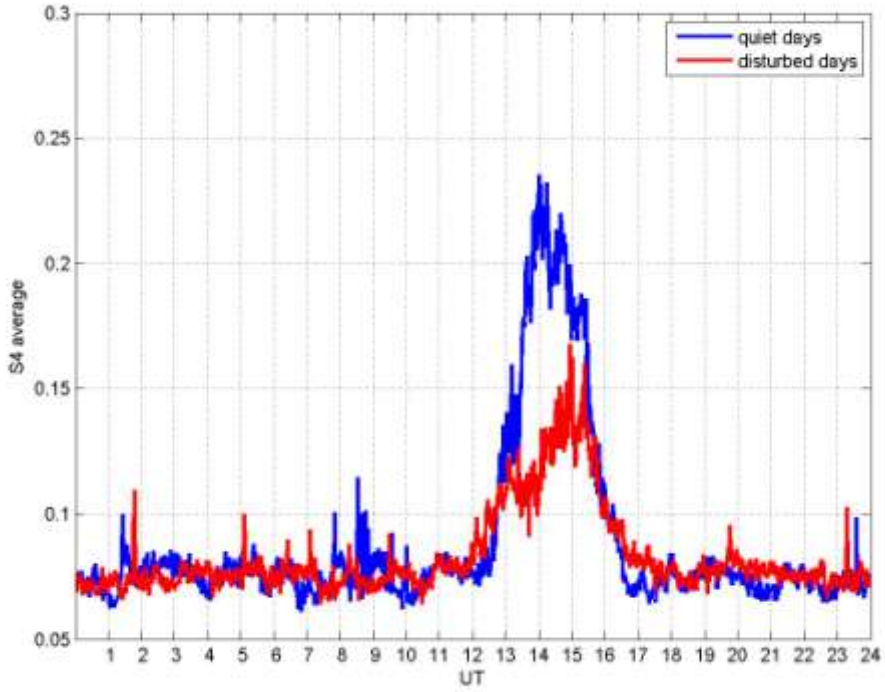

Figure 3-77 S4 average during magnetic quiet and disturbed days on September 2013

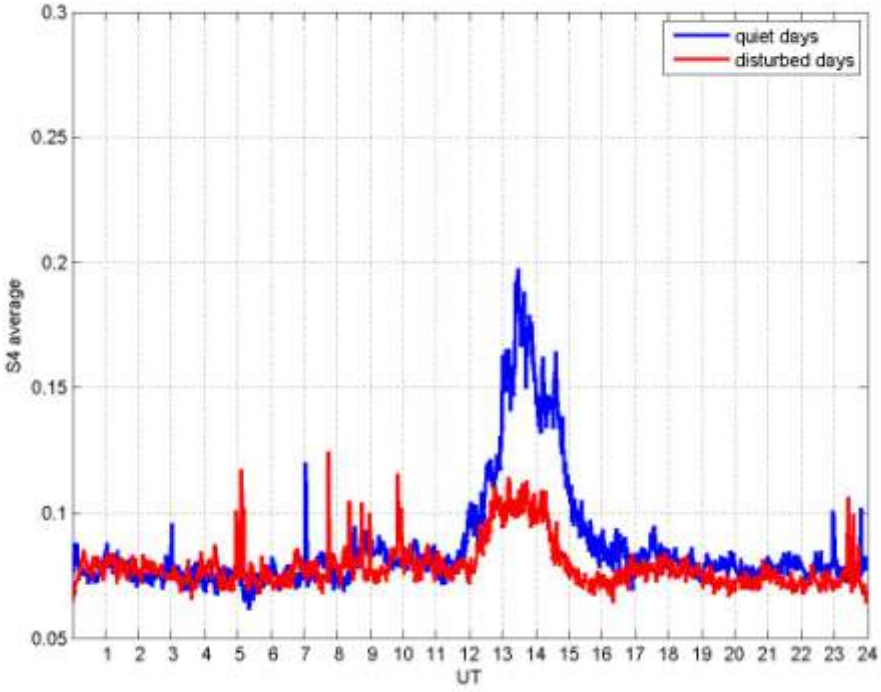

Figure 3-78 S4 average during magnetic quiet and disturbed days on October 2013

3.10. Effect of Scintillation into Pseudorange Accuracy

It has been widely known that ionospheric scintillations generate adverse effect onto GPS tracking performance. In this section the effect of such scintillation into the performance of GPS positioning is analyzed. To get accurate correlation between scintillation and the effect, we propose to use the pseudorange fluctuation of each satellite as indication. To remove the effect of satellite-receiver dynamics, pseudorange is detrended by passing it through a 6 order high pass butterworth filter with cut off frequency of 0.1 Hz. The fluctuation of it is then quantified by calculating the standard deviation named σ_{PR} (sigma PR) as follows:

$$\sigma_{PR} = \sqrt{\langle dPR \rangle - \langle dPR \rangle^2} \qquad \textbf{(3.5)}$$

where dPR is the detrended pseudorange and $\langle . \rangle$ denotes the expected (or average) value over the interval of interest. Interval of 60 seconds is used here to conform to the interval used in S4 and phi60.

Figure 3-79 shows the scatter plot of σ_{PR} against S4 using GPS data taken on 20 September 2014. X-axis here represents S4 while y-axis represents $\sigma_{PR.}$ The obtained fitted line is y=0.14x+0.076, which shows that S4 is proportional to σ_{PR} although it is very noisy. This data is noisy because the relation of σ_{PR} with S4 may be affected by other factor such as satellite elevation angle. Nevertheless, two lines are taken by visual observation as the bound of the scattered data. The lower bound is y=0.1x+0.03 line, while the upper bound is y=2x line. The y-axis represents σ_{PR} while the x-axis represents S4.

Similar treatment is also applied on phi60 and σ_{PR} which is shown Figure 3-80. Similar pattern is also observed in this plot. The obtained fitted line is y=0.15x+0.087, which shows that phi60 is proportional to σ_{PR} although it is very noisy due to the same reason as the aforementioned case of S4. Data are bounded by y=0.15x+0.03 line and y=6x line. The x-axis here represents phi60 and y-axis represents σ_{PR}.

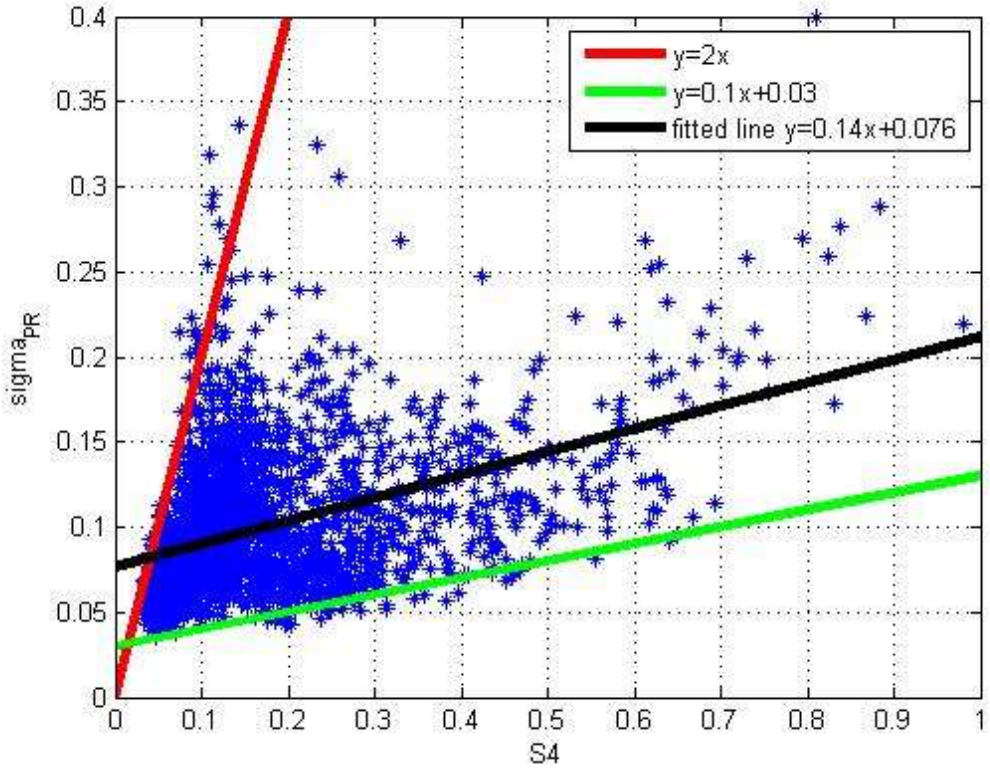

Figure 3-79 Relation of S4 and fluctuation of pseudorange

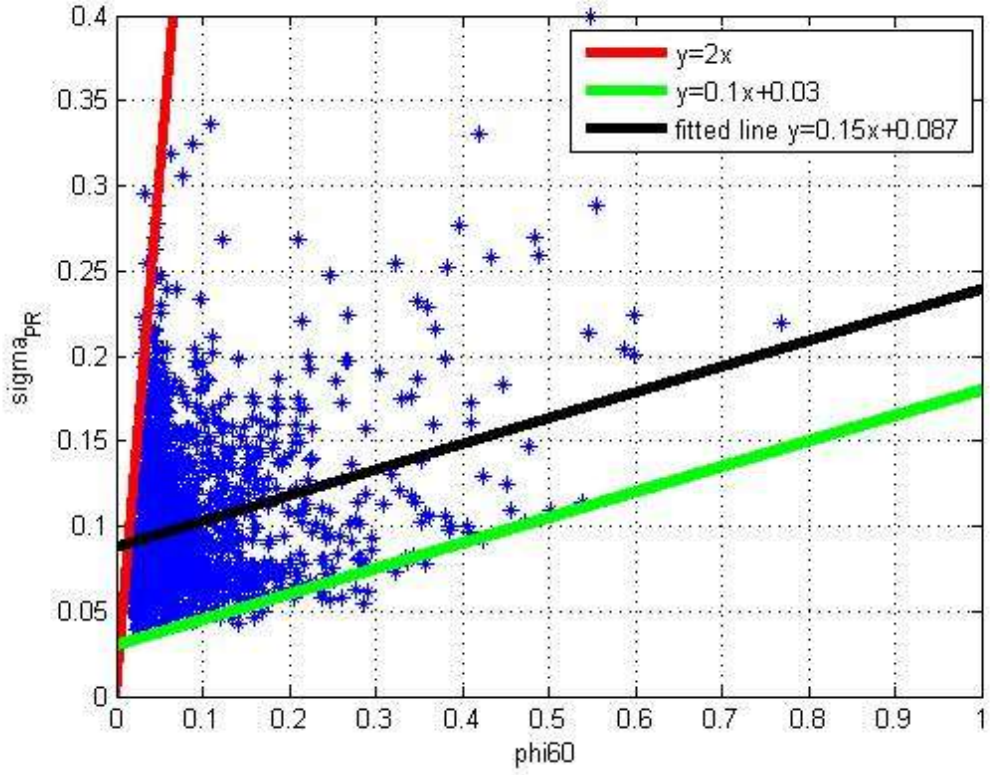

Figure 3-80 Relation of Phi60 and fluctuation of pseudorange

4. Analysis of Other GNSS Constellations and L2 Frequencies

4.1. Comparison among GPS, GLONASS and BeiDou

To compare the scintillation parameters among different GNSS, the average of the ionospheric scintillation related parameters are calculated for visible satellites of GPS, GLONASS, and BeiDou for two selected scintillation days. Galileo data is not presented in this thesis because most of the time it can't be seen from Singapore and sometimes only one satellite is visible. Figure 4-1 and Figure 4-2 show the S4, C/N_0, phi60, ROT, sTEC, and ROTI data on 9 and 14 March 2014. STEC is used instead of vTEC because the current firmware of PolaRxS receiver is unable to give BeiDou elevation angle which is needed to calculate vTEC. It is observed that GPS, GLONASS, and BeiDou exhibit very similar value of S4, phi60, and ROTI. Some early work about using GLONASS as ionospheric scintillation monitoring has been done in Brazil [28] which reported that special attention needs to be given to the obtained phi60 due to higher phase noise produced by GLONASS satellites.

Phi60 of GLONASS generally has higher noise floor than GPS and BeiDou. This is caused by higher jitter on GLONASS satellites oscillators [4]. These fluctuations make the GLONASS signals less suitable for phase scintillation studies because it will be difficult to separate true scintillation events from these non-scintillation effects [21].

TEC obtained by BeiDou is lower than that from GPS and even reach negative value, while GLONASS is higher. This is caused by inaccurate instrumental bias estimation done by the receiver. TEC measurements derived from differencing dual-frequency GNSS delays are corrupted by instrumental biases in both the receiver and satellite transmitters. The instrumental bias is the difference of the two dispersive delays introduced by the analog hardware in the L1and L2 signal paths [59]. To solve this problem, receiver's firmware needs to be upgraded to calculate GLONASS and BeiDou TEC bias correctly. The calculation of such TEC bias is beyond the scope of this thesis and can be found in several references [59][60][61][62].

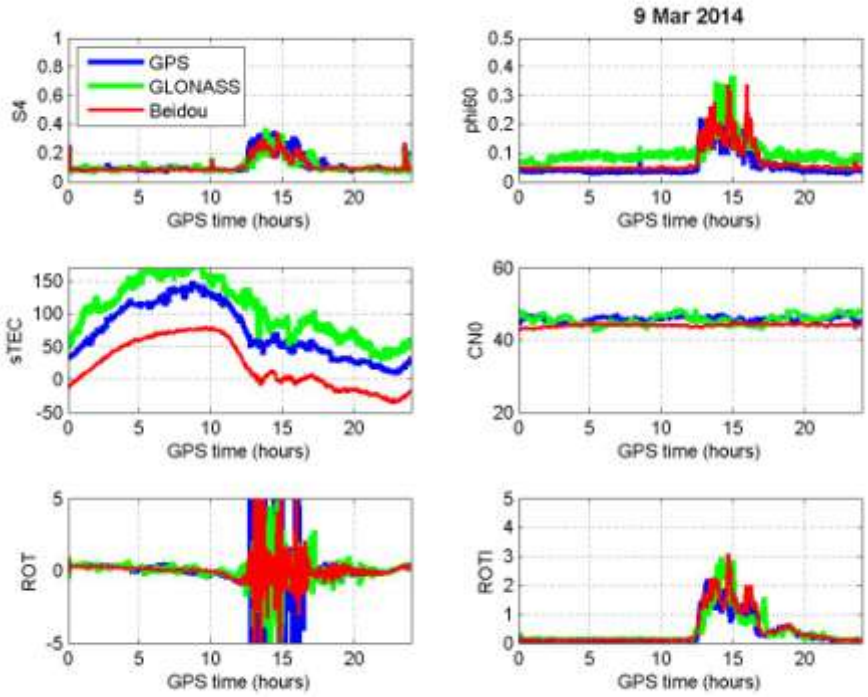

Figure 4-1 Comparison of GPS, GLONASS, and BeiDou Average Data on 9 March 2014

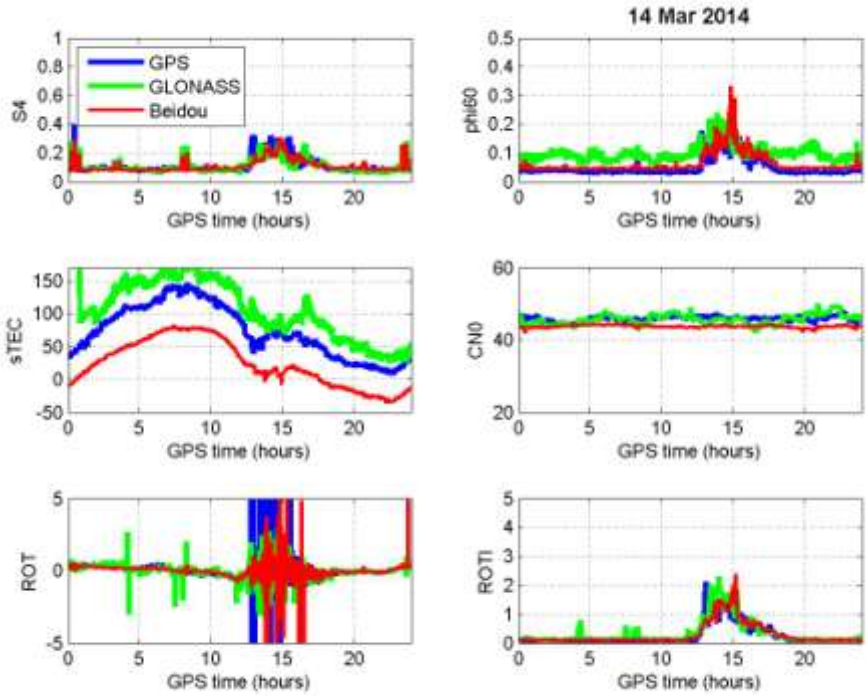

Figure 4-2 Comparison of GPS, GLONASS, and BeiDou Average Data on 14 March 2014

Next, by using (3-2), the correlation coefficient is calculated for S4, phi60, and ROTI between GPS GLONASS, and BeiDou. Table 4-1 shows the correlation coefficient between the scintillation parameters of GPS and GLONASS during 10 selected scintillation days, while Table 4-2 shows the correlation coefficient of GPS and BeiDou. The obtained correlation coefficients for both cases are high, which indicate similar scintillation observations between GPS, GLONASS, and BeiDou.

Table 4-1 Correlation coefficient between GPS and GLONASS during scintillation days

day	S4 correlation coefficient	phi60 correlation coefficient	ROTI correlation coefficient
9 March 2014	0.73	0.75	0.79
14 March 2014	0.76	0.67	0.84
16 March 2014	0.82	0.78	0.88
24 March 2014	0.82	0.76	0.78
28 March 2014	0.92	0.87	0.92
2 April 2014	0.80	0.83	0.83
17 April 2014	0.84	0.74	0.83
18 April 2014	0.86	0.82	0.87
1 September 2014	0.81	0.75	0.83
9 September 2014	0.82	0.81	0.86

Table 4-2 Correlation coefficient between GPS and BeiDou during scintillation days

day	S4 correlation coefficient	phi60 correlation coefficient	ROTI correlation coefficient
9 March 2014	0.89	0.89	0.89
14 March 2014	0.82	0.83	0.87
16 March 2014	0.80	0.79	0.94
24 March 2014	0.91	0.82	0.90
28 March 2014	0.95	0.92	0.93
2 April 2014	0.89	0.84	0.91
17 April 2014	0.89	0.87	0.94
18 April 2014	0.93	0.91	0.94
1 September 2014	0.89	0.91	0.89
9 September 2014	0.90	0.90	0.92

To make a closer observation on the different satellite systems, a sample of scintillation event taken place at the same period and at the same spot of the sky is plotted. Figure 4-3 shows the S4 of satellite G13 (G refer to GPS) and R19 (R refers to GLONASS) at 22.00-23.00 local time (LT) on 9 March 2014. It is observed that scintillation affected R19 slightly earlier than G13. Figure 4-4 is the polar plot showing the elevation and azimuth angle of those satellites when S4 exceeded 0.2 during the aforementioned time span. It is shown that those satellites were affected by scintillation at azimuth angle around 130 to 140 and elevation angle around 30 to 60.

In conclusion, both GPS and GLONASS satellites in the nearby region in the sky suffered ionospheric scintillation at approximately the same time span. The slight difference in the scintillation time is caused by the fact that both satellites are not exactly located at the same spot. Ionospheric irregularity variation in those two nearby locations may cause the slight time delay. Further study about the variation of ionosphere irregularity shape needs more detailed analysis on more samples of scintillation affected satellites which can be done in the future. BeiDou satellite is not shown here because the current firmware of the receiver is not able to track BeiDou satellite’s azimuth and elevation angle.

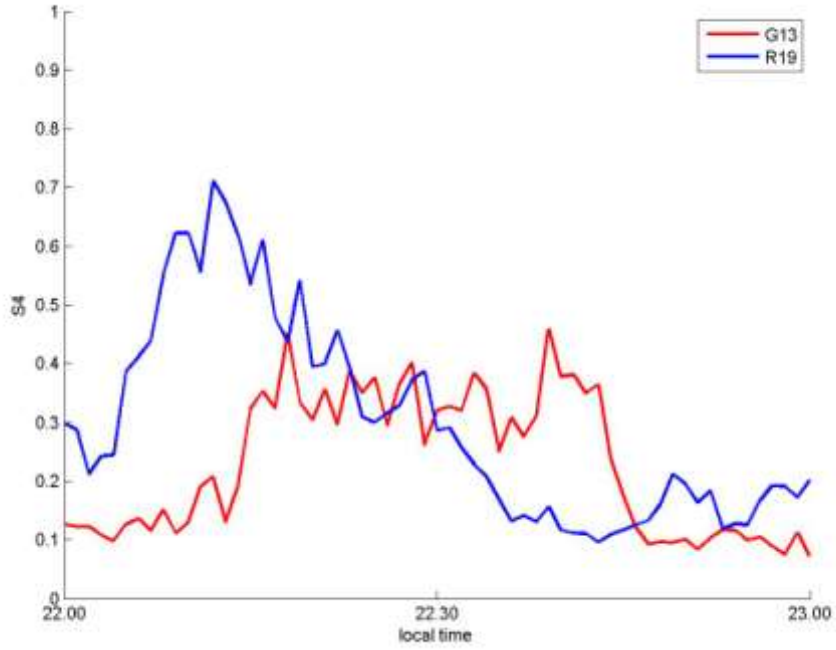

Figure 4-3 S4 of GPS 13 and GLONASS 19 satellites at 22.00-23.00 LT on 9 March 2014

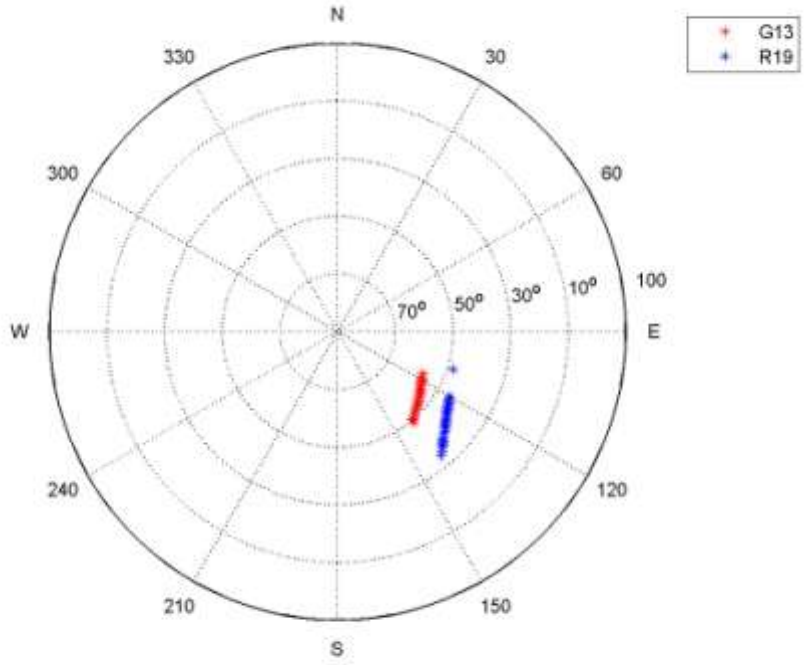

Figure 4-4 Satellite path of GPS 13 and GLONASS 19 satellites with S4>0.2 at 22.00-23.00 LT on 9 March 2014

4.2. GLONASS Ionospheric Scintillation Results

4.2.1. Number of Occurrence of GLONASS Scintillation Events

In this section we try to identify the number of occurrence of scintillation events throughout years 2012 and 2013 based on GLONASS scintillation parameters S4, phi60, and ROTI separately. A scintillation event is identified if S4 value is higher than 0.2 for at least 10 minutes. Separately for phi60, a scintillation event is identified if its value is larger than 0.1 for at least 10 minutes while for ROTI, if its value is larger than 0.5 for the same amount of time. Recorded data with satellite's elevation angle less than 20 degree are excluded to minimize false scintillation event caused by multi path effect.

24 GLONASS satellites are used here. Data available from the receiver in S2 is starting from March 21st 2012 until December 2013. If the scintillation parameters of any of the 24 GLONASS satellites meet the aforementioned conditions, it is counted as one scintillation event. Note that the counting will be performed for each S4, phi60, and ROTI separately.

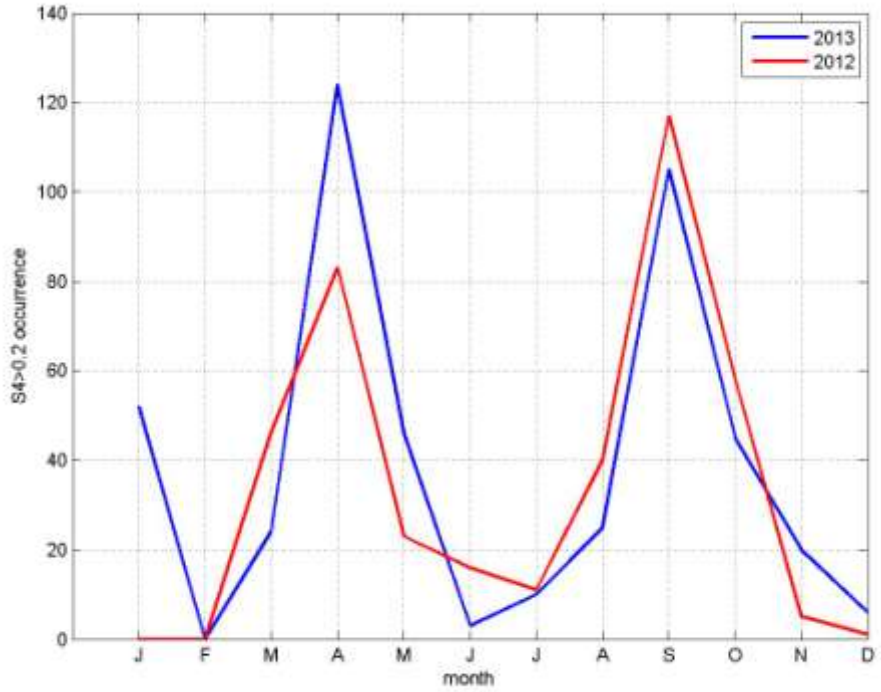

Figure 4-5 Monthly Occurrence of GLONASS S4>0.2

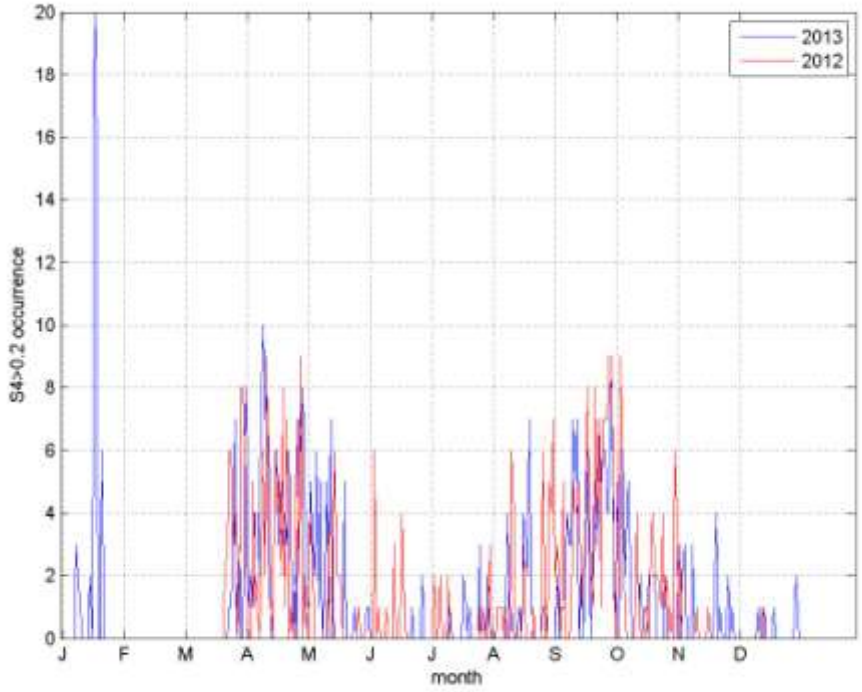

Figure 4-6 Daily Occurrence of GLONASS S4>0.2

Figure 4-5 shows the monthly occurrence of S4 larger than 0.2 throughout years 2012 and 2013. It can be seen that for both years, the months April and September exhibit the highest number of occurrence whereby the S4 is larger than 0.2. On the other hand, Figure 4-6 shows the daily occurrence of S4 larger than 0.2 for the same period. Similarly, we also observe high occurrence of S4 larger than 0.2 congregating around the months of April/May and September/October.

Table 4-3 GLONASS S4>0.2 occurrence in 2012

2012	1	2	3	4	5	6	7	8	9	10	11	12	13	14	15	16	17	18	19	20	21	22	23	24	25	26	27	28	29	30	31	total
January	0	0	0	0	0	0	0	0	0	0	0	0	0	0	0	0	0	0	0	0	0	0	0	0	0	0	0	0	0	0	0	**0**
February	0	0	0	0	0	0	0	0	0	0	0	0	0	0	0	0	0	0	0	0	0	0	0	0	0	0	0	0	0	0	0	**0**
March	0	0	0	0	0	0	0	0	0	0	0	0	0	0	0	0	0	0	0	0	4	2	6	9	1	9	0	0	9	10	10	**60**
April	1	0	0	6	0	2	1	0	11	10	7	1	0	0	4	6	9	0	10	1	12	0	2	0	0	5	4	9	0	6	0	**107**
May	0	3	2	0	0	1	0	0	0	0	5	1	0	10	2	2	2	0	1	0	0	0	0	0	1	2	0	0	0	0	0	**32**
June	0	0	6	0	2	0	0	0	1	0	0	0	3	0	0	0	7	0	0	0	0	0	0	0	0	0	0	0	0	0	0	**19**
July	0	4	0	0	2	0	0	0	4	0	0	0	0	0	0	0	0	0	0	0	0	0	0	0	0	0	1	0	0	4	0	**15**
August	0	0	1	0	3	0	2	1	0	3	2	0	0	1	0	3	1	0	0	0	4	0	0	0	0	3	0	0	4	7	5	**40**
September	1	2	1	0	8	5	0	0	0	10	6	2	7	3	1	3	10	3	3	3	8	5	6	4	15	21	11	9	11	7	0	**165**
October	0	8	10	6	5	0	0	0	0	1	4	2	0	0	2	2	0	4	5	5	2	4	0	1	0	4	0	1	0	11	5	**82**
November	0	2	1	0	0	0	0	0	0	0	0	0	0	0	0	0	0	0	2	0	0	0	0	0	0	0	0	0	0	0	0	**5**
December	0	0	0	0	0	0	0	0	0	0	4	0	0	0	0	0	0	0	0	0	0	0	0	0	0	0	0	0	0	0	0	**4**

Table 4-4 GLONASS S4>0.2 occurrence in 2013

2013	1	2	3	4	5	6	7	8	9	10	11	12	13	14	15	16	17	18	19	20	21	22	23	24	25	26	27	28	29	30	31	total
January	0	0	0	0	0	0	0	2	1	7	0	0	0	0	1	0	0	0	0	0	0	0	0	0	0	0	0	0	0	0	0	**11**
February	0	0	0	0	0	0	0	1	0	0	0	0	0	0	0	1	0	2	0	0	0	5	2	0	0	0	1	0	0	0	0	**12**
March	0	2	0	0	0	0	2	3	2	7	4	5	5	3	4	0	0	0	3	3	0	9	0	3	9	9	0	4	0	0	9	**86**
April	8	3	8	0	6	5	5	10	10	10	8	8	0	0	8	11	6	9	5	2	4	6	1	0	3	1	10	10	8	7	0	**172**
May	0	7	5	4	9	0	6	0	0	9	0	11	2	2	0	0	0	0	6	1	0	0	0	0	0	0	0	0	0	2	0	**64**
June	0	0	0	1	0	0	0	1	0	0	0	0	0	1	0	0	0	1	0	0	0	1	0	0	0	0	1	0	0	0	0	**6**
July	0	0	0	0	0	0	0	2	0	0	1	0	0	1	0	4	2	0	0	1	0	0	0	0	1	0	0	0	1	0	0	**13**
August	1	0	0	0	0	0	1	4	0	3	1	0	0	1	0	5	4	4	5	0	0	0	0	0	0	0	1	0	0	0	0	**30**
September	2	0	0	0	0	0	3	3	3	5	7	6	3	1	5	7	7	2	0	3	8	4	7	5	6	8	7	6	9	9	0	**126**
October	8	0	7	8	7	8	6	2	0	0	3	2	2	4	0	0	4	4	2	1	0	0	0	0	3	0	0	1	2	0	0	**74**
November	0	0	1	5	0	0	0	1	0	0	0	0	0	0	0	0	0	0	2	2	1	0	0	0	1	3	0	1	0	0	0	**17**
December	0	0	0	0	0	0	0	0	1	0	0	0	2	0	0	0	0	0	0	0	0	0	0	0	0	0	0	0	0	0	0	**3**

Table 4-3 and Table 4-4 Table 3-2 show a more detailed number of occurrence of S4 larger than 0.2 for years 2012 and 2013, respectively. Highest occurrences of amplitude scintillations are observed in month April and September for both years.

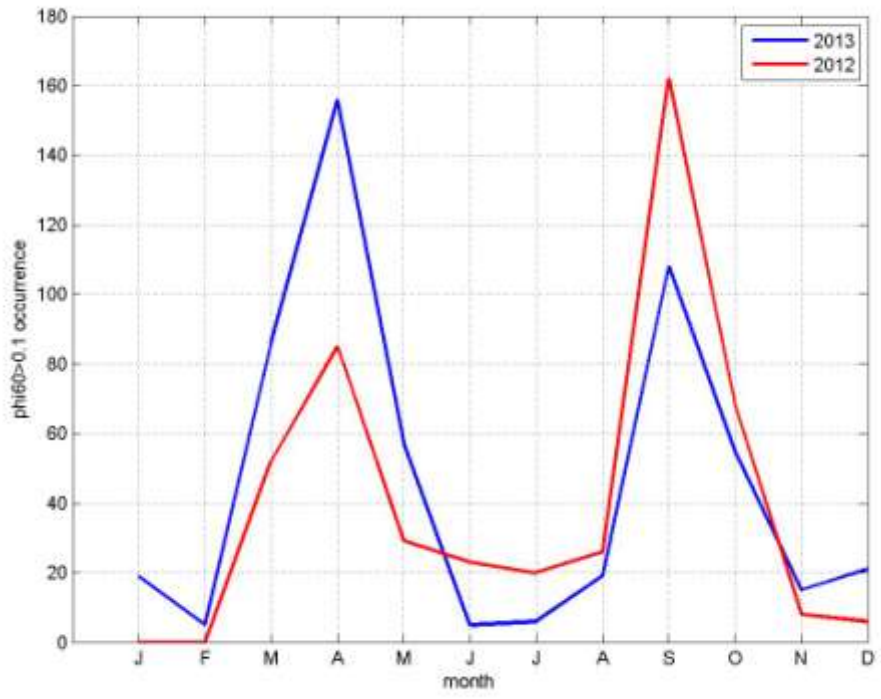

Figure 4-7 Monthly Occurrence of GLONASS Phi60>0.1

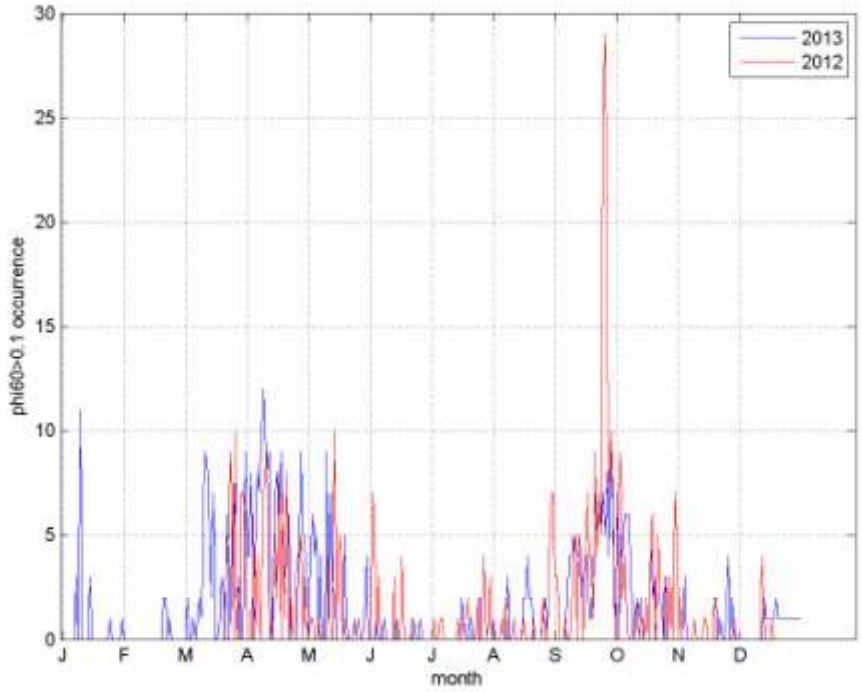

Figure 4-8 Daily Occurrence of GLONASS Phi60>0.1

Figure 4-7 and Figure 4-8 now show the monthly and daily occurrence of phase scintillation indicated by phi60 larger than 0.1 for years 2012 and 2013. Similar to amplitude scintillation, the months of April and September of both years also exhibit the highest number of occurrences of phase scintillation.

Table 4-5 GLONASS phi60>0.1 occurrence in 2012

2012	1	2	3	4	5	6	7	8	9	10	11	12	13	14	15	16	17	18	19	20	21	22	23	24	25	26	27	28	29	30	31	total
January	0	0	0	0	0	0	0	0	0	0	0	0	0	0	0	0	0	0	0	0	0	0	0	0	0	0	0	0	0	0	0	0
February	0	0	0	0	0	0	0	0	0	0	0	0	0	0	0	0	0	0	0	0	0	0	0	0	0	0	0	0	0	0	0	0
March	0	0	0	0	0	0	0	0	0	0	0	0	0	0	0	0	0	0	0	0	2	4	7	9	0	10	0	0	7	7	6	52
April	0	0	0	6	0	4	1	0	7	8	9	0	0	0	5	2	8	0	7	1	8	0	2	0	1	4	4	5	0	3	0	85
May	0	1	1	0	0	1	0	0	0	0	4	0	0	10	1	4	5	0	1	0	0	0	0	0	0	1	0	0	0	0	0	29
June	0	7	5	0	3	0	0	0	0	0	0	0	3	0	0	0	4	0	0	0	0	0	1	0	0	0	0	0	0	0	0	23
July	0	1	0	0	1	1	0	0	0	0	0	0	0	1	0	0	1	1	2	1	1	0	0	2	0	0	4	1	0	3	0	20
August	0	0	0	0	1	0	2	0	0	0	1	0	0	0	0	1	0	0	0	0	1	0	0	0	0	2	0	0	4	7	7	26
September	3	3	0	0	0	1	0	0	1	5	4	0	5	4	0	2	7	4	4	1	9	4	7	5	26	29	14	7	10	7	0	162
October	0	7	9	2	4	1	0	0	0	1	2	0	1	1	0	2	0	5	6	0	2	5	1	1	0	3	0	3	0	7	5	68
November	0	2	0	0	0	0	0	0	1	0	0	0	0	1	1	0	0	0	2	0	0	0	0	0	0	0	0	0	1	0	0	8
December	0	0	0	0	0	0	0	0	0	0	0	4	1	0	0	0	1	0	0	0	0	0	0	0	0	0	0	0	0	0	0	6

Table 4-6 GLONASS phi60>0.1 occurrences in 2013

2013	1	2	3	4	5	6	7	8	9	10	11	12	13	14	15	16	17	18	19	20	21	22	23	24	25	26	27	28	29	30	31	total
January	0	0	0	0	0	0	0	3	0	11	0	0	0	0	3	0	0	0	0	0	0	0	0	0	1	0	0	0	0	0	1	19
February	0	0	0	0	0	0	0	0	0	0	0	0	0	0	0	0	0	0	0	0	2	2	0	1	0	0	0	0	0	0	0	5
March	0	2	0	0	1	0	1	2	1	7	9	8	5	2	7	0	0	1	3	2	0	6	0	3	6	8	0	3	0	0	9	86
April	4	4	8	0	4	8	7	9	12	10	8	9	0	1	7	8	6	9	5	3	4	6	0	0	0	0	5	9	5	5	0	156
May	0	4	6	4	5	0	4	0	0	9	1	7	3	2	0	0	0	0	5	1	0	0	0	1	0	0	0	0	1	4	0	57
June	0	0	0	1	0	0	0	1	0	0	0	0	0	1	0	0	0	0	0	0	0	1	0	0	0	1	0	0	0	0	0	5
July	0	0	0	0	0	0	0	0	0	0	0	0	0	0	0	2	1	0	0	1	0	0	0	0	2	0	0	0	0	0	0	6
August	1	0	0	0	0	0	0	3	0	0	0	0	0	0	0	2	2	4	2	2	0	0	0	0	0	1	2	0	0	0	0	19
September	0	0	0	0	0	0	2	4	4	4	5	4	4	2	3	4	4	1	1	3	7	5	7	5	7	5	8	4	9	6	0	108
October	7	0	5	4	6	6	6	3	0	0	2	1	2	0	0	0	0	5	2	3	0	0	0	0	3	0	0	0	0	0	0	55
November	0	0	0	3	0	0	0	0	0	0	0	0	0	0	0	0	0	0	2	2	0	1	0	0	1	4	0	2	0	0	0	15
December	0	0	0	0	0	0	0	0	0	0	0	0	2	1	1	1	1	1	2	1	1	1	1	1	1	1	1	1	1	1	1	21

Table 4-5 and Table 4-6 show a more detailed number of occurrence of phi60 larger than 0.1 for years 2012 and 2013, respectively. For both years, highest occurrences of phase scintillations are again observed in equinox months of April and September.

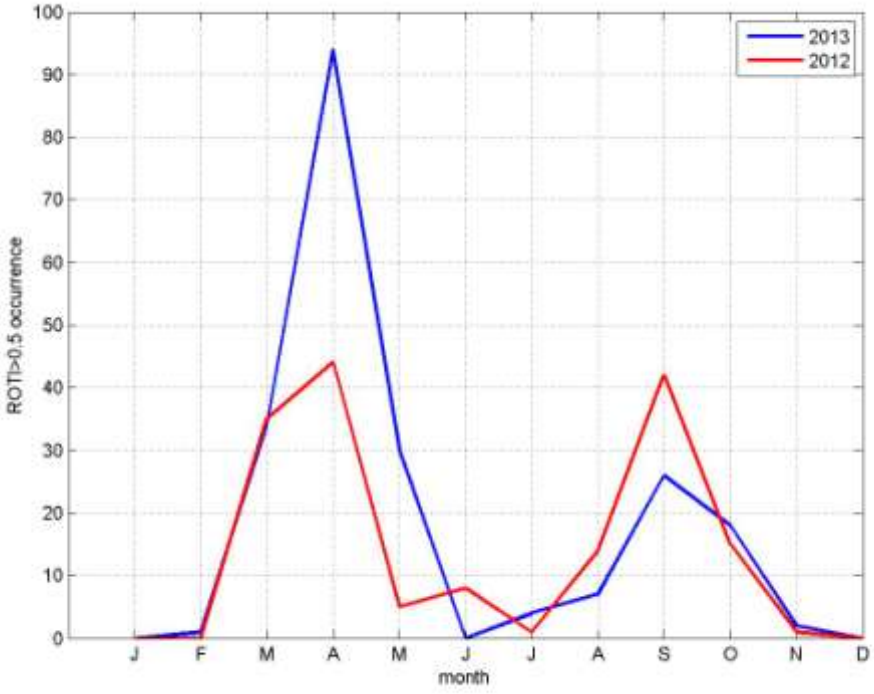

Figure 4-9 Monthly Occurrence of GLONASS ROTI>0.5

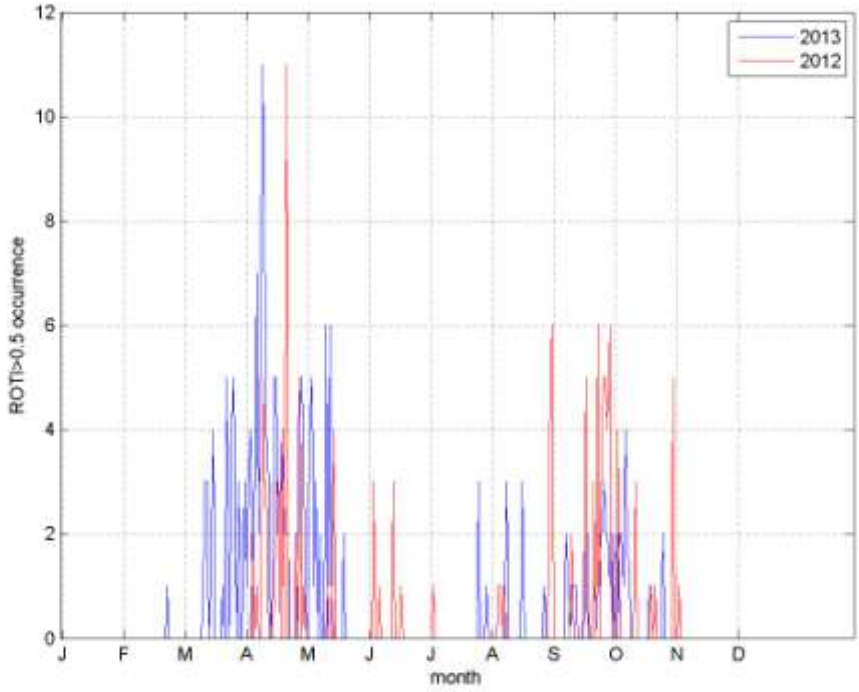

Figure 4-10 Daily Occurrence of GLONASS ROTI>0.5

Figure 4-9 and Figure 4-10 now show the monthly and daily occurrence of ROTI larger than 0.5 for years 2012 and 2013. Similar also to S4 parameter, the months of April and September of both years exhibit the highest number of occurrence.

Table 4-7 GLONASS ROTI>0.5 occurrence in 2012

2012	1	2	3	4	5	6	7	8	9	10	11	12	13	14	15	16	17	18	19	20	21	22	23	24	25	26	27	28	29	30	31	total
January	0	0	0	0	0	0	0	0	0	0	0	0	0	0	0	0	0	0	0	0	0	0	0	0	0	0	0	0	0	0	0	0
February	0	0	0	0	0	0	0	0	0	0	0	0	0	0	0	0	0	0	0	0	0	0	0	0	0	0	0	0	0	0	0	0
March	0	0	0	0	0	0	0	0	0	0	0	0	0	0	0	0	0	0	0	0	0	0	0	0	0	0	0	0	0	0	0	0
April	0	0	0	2	0	1	0	0	5	3	3	0	0	0	1	3	3	0	4	0	11	0	0	0	0	2	0	5	0	1	0	44
May	0	0	0	0	0	0	0	0	0	0	1	0	0	4	0	0	0	0	0	0	0	0	0	0	0	0	0	0	0	0	0	5
June	0	0	3	0	0	1	0	0	0	0	0	0	3	0	0	0	1	0	0	0	0	0	0	0	0	0	0	0	0	0	0	8
July	0	1	0	0	0	0	0	0	0	0	0	0	0	0	0	0	0	0	0	0	0	0	0	0	0	0	0	0	0	0	0	1
August	0	0	0	1	1	0	1	0	0	0	0	0	0	0	0	0	0	0	0	0	0	0	0	0	0	0	0	0	0	5	6	14
September	0	0	0	0	0	0	0	0	0	2	0	0	0	0	0	1	5	1	0	0	3	0	6	0	4	5	5	4	6	0	0	42
October	0	4	1	0	0	0	0	0	0	0	3	0	0	0	0	0	0	0	1	0	1	0	0	0	0	0	0	0	0	5	0	15
November	0	1	0	0	0	0	0	0	0	0	0	0	0	0	0	0	0	0	0	0	0	0	0	0	0	0	0	0	0	0	0	1
December	0	0	0	0	0	0	0	0	0	0	0	0	0	0	0	0	0	0	0	0	0	0	0	0	0	0	0	0	0	0	0	0

Table 4-8 GLONASS ROTI>0.5 occurrence in 2013

2013	1	2	3	4	5	6	7	8	9	10	11	12	13	14	15	16	17	18	19	20	21	22	23	24	25	26	27	28	29	30	31	total
January	0	0	0	0	0	0	0	0	0	0	0	0	0	0	0	0	0	0	0	0	0	0	0	0	0	0	0	0	0	0	0	0
February	0	0	0	0	0	0	0	0	0	0	0	0	0	0	0	0	0	0	0	0	0	0	1	0	0	0	0	0	0	0	0	1
March	0	0	0	0	0	0	0	0	0	1	3	3	0	1	4	0	0	0	0	1	0	5	0	1	5	4	0	3	0	0	3	34
April	1	3	4	0	2	7	2	6	11	8	4	3	0	1	5	5	2	3	4	2	2	2	0	0	0	0	4	5	5	3	0	94
May	0	4	5	1	3	0	2	0	0	6	0	6	1	0	0	0	0	0	2	0	0	0	0	0	0	0	0	0	0	0	0	30
June	0	0	0	0	0	0	0	0	0	0	0	0	0	0	0	0	0	0	0	0	0	0	0	0	0	0	0	0	0	0	0	0
July	0	0	0	0	0	0	0	0	0	0	0	0	0	0	0	0	0	0	0	0	0	0	0	0	3	0	0	0	1	0	0	4
August	0	0	0	0	0	0	0	3	0	0	0	0	0	0	0	3	0	0	0	0	0	0	0	0	0	0	1	0	0	0	0	7
September	0	0	0	0	0	0	2	1	0	1	1	1	0	0	0	0	2	0	0	0	3	0	1	2	2	3	2	2	1	2	0	26
October	2	0	2	2	1	4	2	1	0	0	0	0	0	0	0	0	0	1	1	0	0	0	0	0	2	0	0	0	0	0	0	18
November	0	0	0	1	0	0	0	0	0	0	0	0	0	0	0	0	0	0	0	0	0	0	0	0	0	0	0	1	0	0	0	2
December	0	0	0	0	0	0	0	0	0	0	0	0	0	0	0	0	0	0	0	0	0	0	0	0	0	0	0	0	0	0	0	0

Table 4-7 and

Table 4-8 show a more detailed number of occurrence of ROTI larger than 0.5 for years 2012 and 2013, respectively. For both years, highest occurrence of ROTI larger than 0.5 is again observed in months April and September.

To conclude for this section, ionospheric scintillation peak usually happen in around April and September (equinox) for both years 2012 and 2013. Generally, high S4 will also correspond to higher phi60 and ROTI values. This result agrees with previous conclusion obtained by GPS data.

4.2.2. GLONASS Equinox Scintillation

To get closer study during equinox months, the monthly S4, phi60, and ROTI average of GLONASS satellites are computed where those parameters are averaged over all visible GLONASS satellites in every minute. The visible satellites are only limited to those having elevation angle more than 20 degrees to filter out fluctuation due to multipath effects.

Figure 4-11 to Figure 4-13 show the monthly S4, phi60, and ROTI average of visible GLONASS satellites during the equinox months of March, April, September and October 2013. The *y* and *x* axes for each subplot represent the day (1^{st} to 30^{th} or 31^{st}) and local time (8 a.m. to 8 a.m. next day) in each month. It can be observed that in equinox months, relatively high scintillation is present in reasonably high number of

days which agrees with GPS outcome presented in previous section. This is attributed to the close alignment of the solar terminator with magnetic meridian [41].

Similarly to GPS result, these scintillation events occur mostly around local time of 8 p.m. to 12 a.m, which is during the post sunset period. This is attributed to the eastward prereversal enhancement (PRE) electric field, which is coupled with the earth's geomagnetic field to produce an upward vertical force derived from ***E*** **x** ***B***. The upward vertical force results in steep gradient of ion and electron densities between upper and lower layer, thereby producing plasma bubble irregularities arising from Rayleigh-Taylor instability process [4].

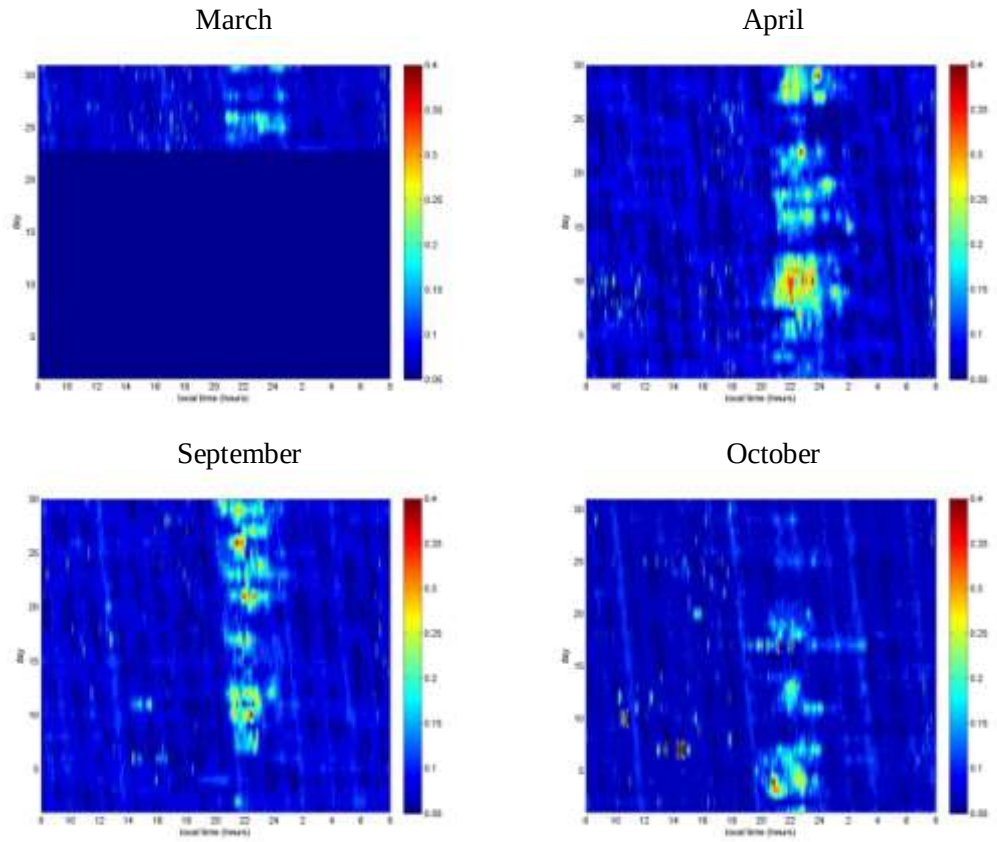

Figure 4-11 Monthly GLONASS S4 average during the equinox months of year 2013

March

April

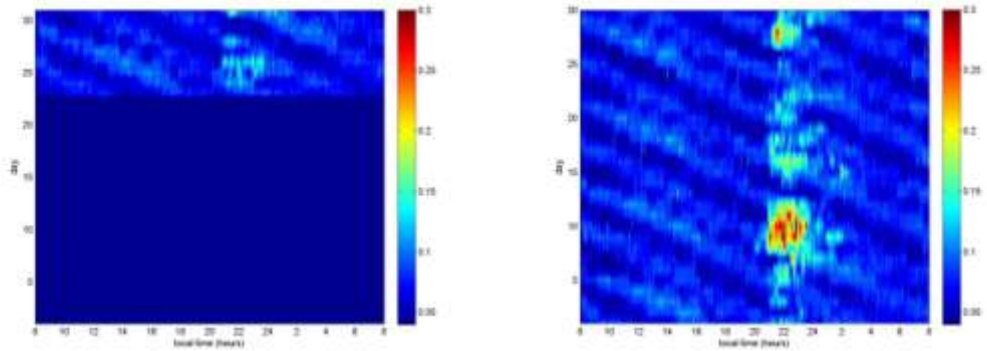

September

October

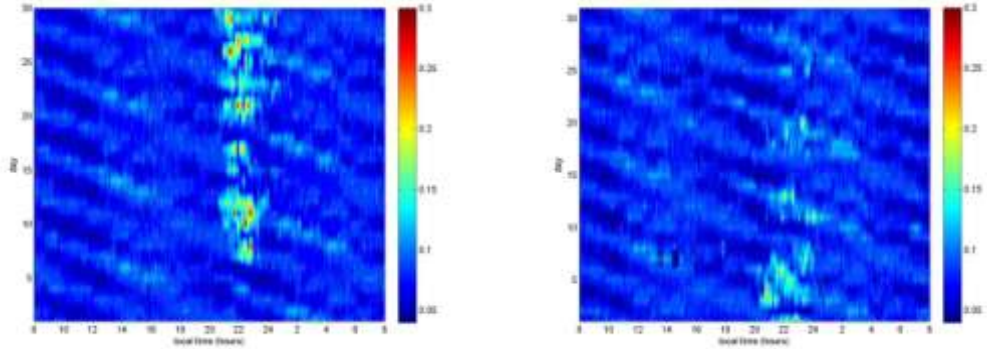

Figure 4-12 Monthly GLONASS Phi60 average during the equinox months of year 2013

March

April

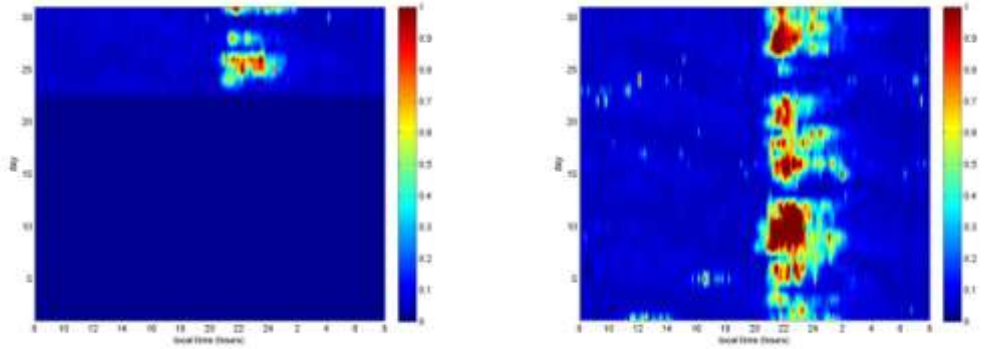

September

October

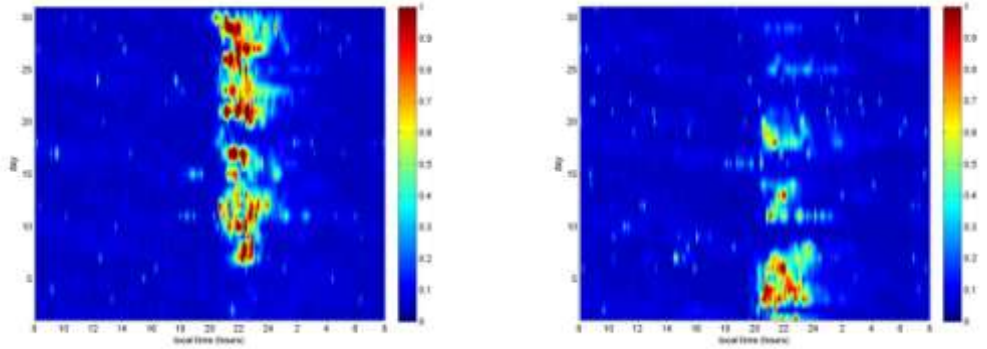

Figure 4-13 Monthly GLONASS ROTI average during the equinox months of year 2013

4.2.3. GLONASS Ionospheric Scintillation Sky Plot

Similarly to GPS, the spatial distribution of GLONASS scintillation is analyzed. S4, phi60, and ROTI sky plot on equinox months of year 2013 are presented in Figure 4-14 to Figure 4-16. The ionosphere over Singapore is divided into bins of geographic latitude and longitude with resolution of two degree. Those scintillation parameters are then averaged in each bin. The *x*-axis shows the longitude where the ionosphere is projected into while *y*-axis shows the latitude.

The S4, phi60, and ROTI obtained by GLONASS here show similar pattern as the outcome of GPS previously presented. High scintillation is concentrated in the south part of the ionosphere over Singapore where the crest of EIA is located. Higher scintillation is also observed in the west part than the east part due to the fact that generally plasma bubbles are tilted westward as they vertically develop [52], [53]. The high S4 in the north part is due to the remaining multipath effect that was failed to be filtered. Another possible reason is that in lower elevation angle the ionosphere layer that GLONASS signal traverse through is thicker compared to that in high elevation angle which also increase the magnitude of its perturbation [54]. This behavior is not observed in phi60 and ROTI.

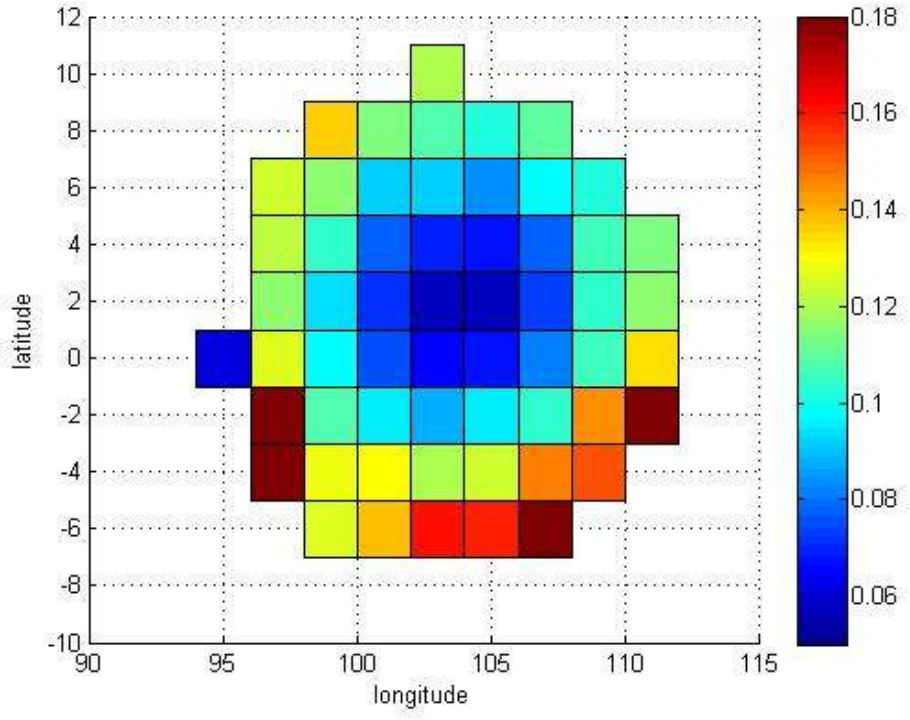

Figure 4-14 S4 GLONASS Spatial Distribution on Equinox 2013

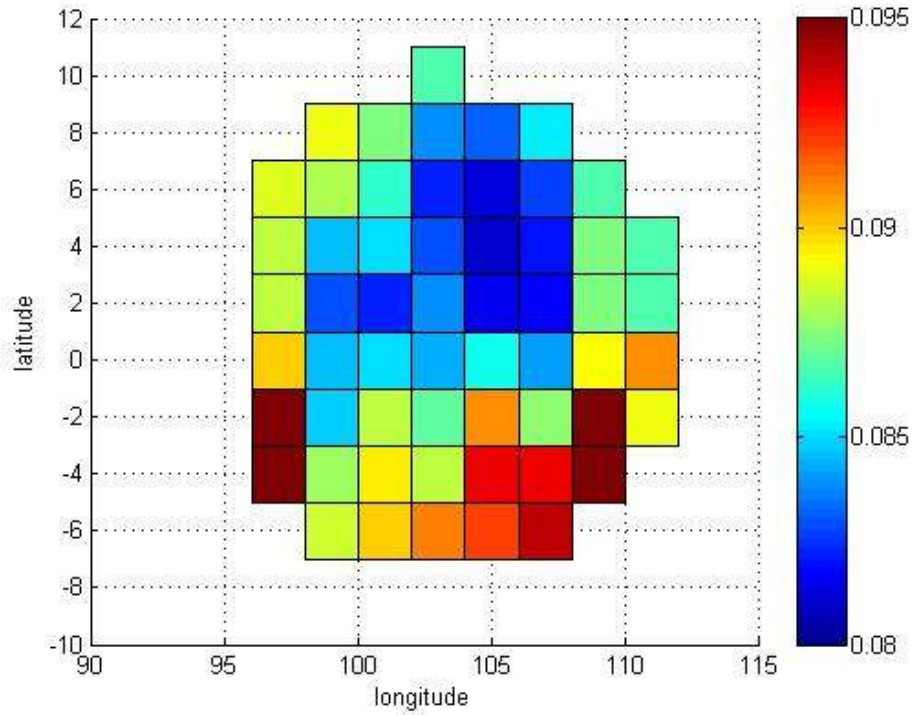

Figure 4-15 Phi60 GLONASS Spatial Distribution on Equinox 2013

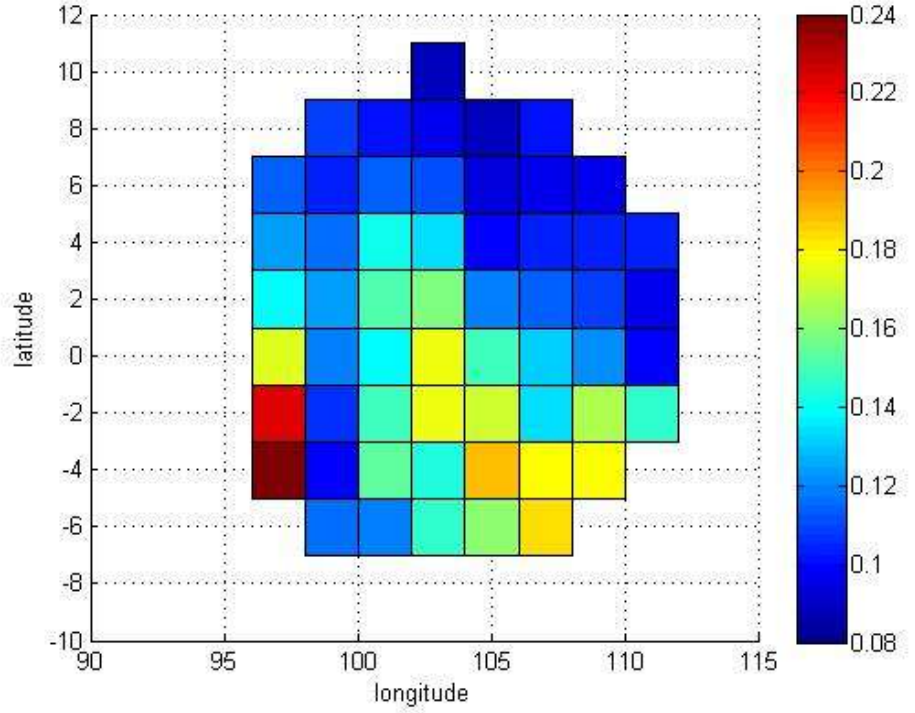

Figure 4-16 ROTI GLONASS spatial distribution on equinox 2013

4.3. BeiDou Ionospheric Scintillation Results

4.3.1. Number of Occurrence of BeiDou Scintillation Events

In this section we try to identify the number of occurrence of scintillation events in BeiDou system throughout years 2013 and 2014 based on scintillation parameters S4, phi60, and ROTI separately. A scintillation event is identified if S4 value is higher than 0.2 for at least 10 minutes. Separately for phi60, a scintillation event is identified if its value is larger than 0.1 for at least 10 minutes while for ROTI, if its value is larger than 0.2 for the same amount of time.

10 available BeiDou satellites are used in this stage. BeiDou data available from the receiver in S2 is starting from January 26th 2013 to September 31st 2014. If the scintillation parameters of any of the BeiDou satellites meet the aforementioned conditions, it is counted as one scintillation event.

Figure 4-17 shows the monthly and daily occurrences of S4 larger than 0.2 throughout years 2013 and 2014 indicating amplitude scintillations. It can be seen that for both years, the equinox months around March/April, and September/October exhibit the highest number of occurrence whereby the S4 is larger than 0.2. On the other hand, Figure 4-18 shows the daily occurrence of S4 larger than 0.2 for the same period. Similarly, we also observe high occurrence of S4 larger than 0.2 congregating around the months of April/May and September/October.

Table 4-9 and Table 4-10 show a more detailed number of occurrence of S4 larger than 0.2 for years 2013 and 2014, respectively. In both years, highest occurrences of amplitude scintillations are observed in equinox months.

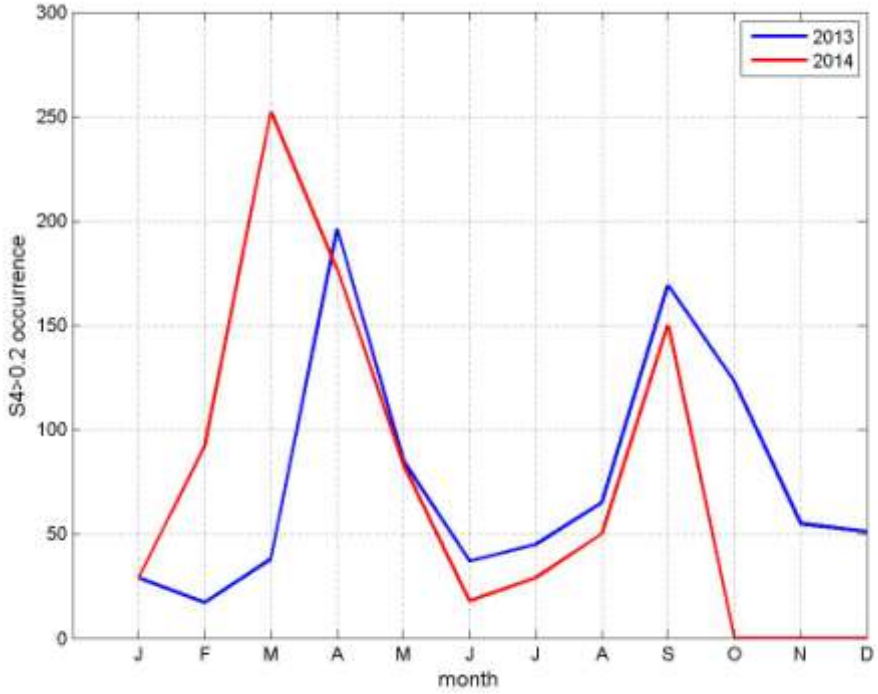

Figure 4-17 Monthly Occurrence of BeiDou S4>0.2

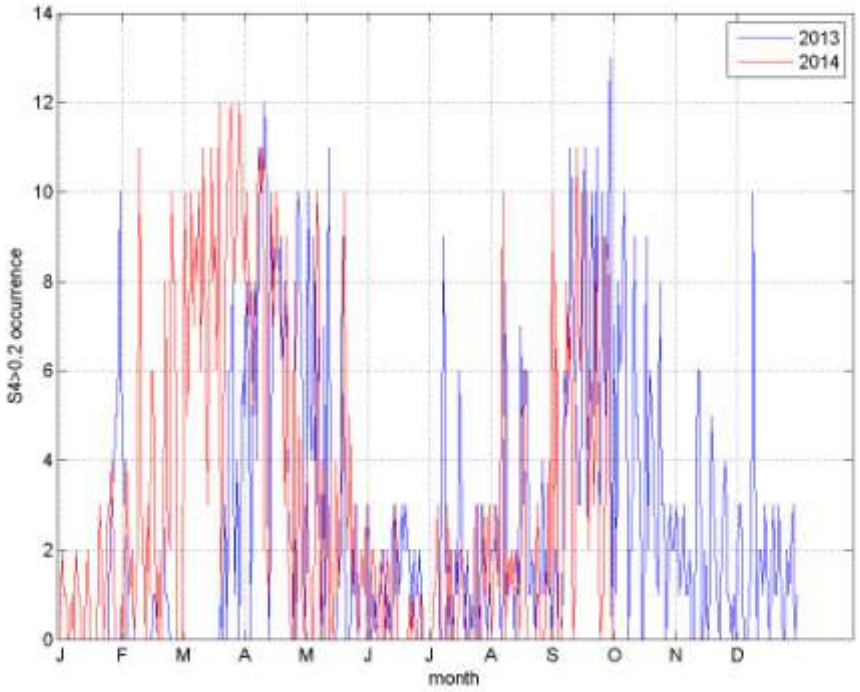

Figure 4-18 Daily Occurrence of BeiDou S4>0.2

Table 4-9 BeiDou S4>0.2 occurrence in 2013

2013	1	2	3	4	5	6	7	8	9	10	11	12	13	14	15	16	17	18	19	20	21	22	23	24	25	26	27	28	29	30	31	total
January	0	0	0	0	0	0	0	0	0	0	0	0	0	0	0	0	0	0	0	0	0	0	0	0	0	2	3	4	5	5	10	29
February	4	4	2	0	0	0	0	0	0	0	0	0	0	0	0	0	1	1	0	0	0	3	1	1	0	0	0	0	0	0	0	17
March	0	0	0	0	0	0	0	0	0	0	0	0	0	0	0	0	0	0	0	1	0	3	0	6	6	8	1	4	0	3	6	38
April	5	8	5	0	7	8	4	9	11	10	12	10	0	2	9	8	8	8	9	6	8	8	3	2	2	0	9	10	8	7	0	196
May	2	10	5	4	9	3	7	2	0	7	0	11	4	0	0	0	1	2	9	3	0	0	0	2	1	3	0	0	0	0	0	85
June	3	0	0	1	0	1	1	2	2	0	1	0	1	3	1	2	1	3	2	3	2	2	0	2	1	1	2	0	0	0	0	37
July	0	0	0	0	0	0	3	9	2	0	2	0	0	2	1	6	4	1	0	2	0	1	0	0	3	0	3	3	2	0	1	45
August	2	2	2	3	1	0	1	8	1	1	2	1	0	2	1	7	3	6	6	1	1	2	0	1	1	1	4	1	2	1	1	65
September	0	2	2	0	0	1	6	5	6	11	7	6	5	3	3	8	11	5	2	8	10	5	11	4	3	10	6	5	11	13	0	169
October	7	1	8	6	7	10	8	0	2	2	9	5	5	3	0	0	9	2	6	5	3	2	1	8	3	3	0	1	3	2	2	123
November	3	2	1	2	3	1	1	2	0	0	2	6	6	0	0	2	0	1	5	3	2	1	0	2	3	4	1	1	0	1	0	55
December	2	3	3	0	0	0	1	2	10	2	0	2	2	1	3	1	0	1	3	1	1	3	1	0	0	2	1	2	3	0	1	51

Table 4-10 BeiDou S4>0.2 occurrence in 2014

2014	1	2	3	4	5	6	7	8	9	10	11	12	13	14	15	16	17	18	19	20	21	22	23	24	25	26	27	28	29	30	31	total
January	0	2	1	1	0	0	1	0	2	1	1	0	0	1	2	0	0	0	0	1	3	1	0	1	3	3	4	1	0	0	0	29
February	1	0	4	3	1	2	0	1	2	11	3	2	0	3	1	6	6	2	0	2	0	3	8	3	2	10	8	8	0	0	0	92
March	4	10	5	7	10	7	9	8	10	6	11	7	3	6	11	8	9	6	12	1	3	8	10	11	12	8	8	10	12	11	9	252
April	8	10	7	8	5	7	8	11	10	11	2	2	1	10	7	8	10	8	7	6	3	9	2	0	0	8	0	5	3	1	0	177
May	4	2	1	0	0	10	9	0	4	3	0	0	4	0	1	4	1	3	4	10	4	2	5	1	3	1	0	1	2	1	3	83
June	1	0	2	2	0	0	0	2	0	1	2	0	0	1	3	0	0	0	0	0	0	1	0	1	0	0	1	1	0	0	0	18
July	0	0	1	1	3	1	0	0	0	3	0	2	0	0	0	2	2	1	1	0	0	0	0	3	0	0	0	3	1	2	3	29
August	0	1	3	2	1	5	10	0	2	1	2	1	2	1	0	1	6	3	0	0	0	0	0	3	1	0	0	0	1	4	0	50
September	10	2	8	0	0	2	2	8	6	7	0	1	11	7	6	10	10	10	2	6	5	3	9	4	0	1	1	9	8	2	0	150
October	0	0	0	0	0	0	0	0	0	0	0	0	0	0	0	0	0	0	0	0	0	0	0	0	0	0	0	0	0	0	0	0
November	0	0	0	0	0	0	0	0	0	0	0	0	0	0	0	0	0	0	0	0	0	0	0	0	0	0	0	0	0	0	0	0
December	0	0	0	0	0	0	0	0	0	0	0	0	0	0	0	0	0	0	0	0	0	0	0	0	0	0	0	0	0	0	0	0

Figure 4-19 and Figure 4-20 show the monthly and daily occurrence of phi60 larger than 0.1 indicating phase scintillations for years 2013 and 2014. Similar to S4 parameter, the months of March/April and September/October of both years also exhibit the highest number of occurrences.

Table 4-11 and Table 4-12 show a more detailed number of occurrences of phi60 larger than 0.1 for years 2013 and 2014, respectively. For both years, highest occurrences of phase scintillations are again observed in months March/April and September/October.

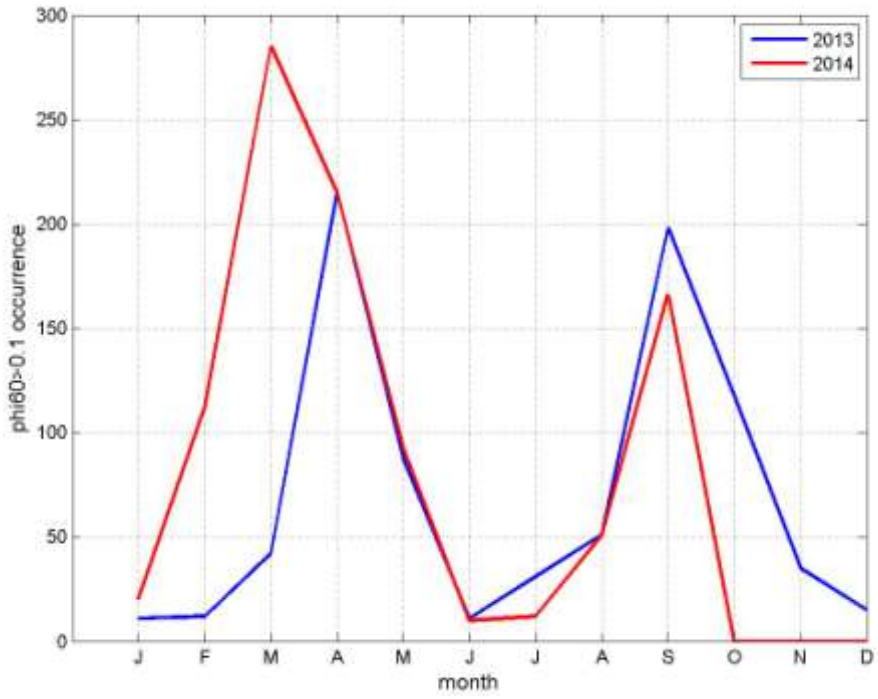

Figure 4-19 Monthly Occurrence of BeiDou Phi60>0.1

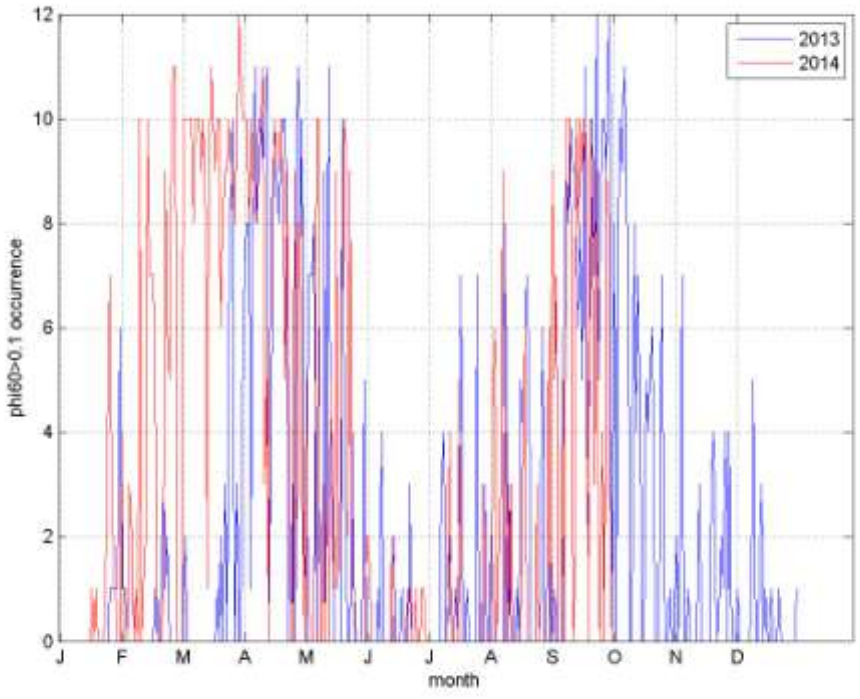

Figure 4-20 Daily Occurrence of BeiDou Phi60>0.1

Table 4-11 BeiDou phi60>0.1 occurrence in 2013

2013	1	2	3	4	5	6	7	8	9	10	11	12	13	14	15	16	17	18	19	20	21	22	23	24	25	26	27	28	29	30	31	total
January	0	0	0	0	0	0	0	0	0	0	0	0	0	0	0	0	0	0	0	0	0	0	0	0	0	1	1	1	1	1	6	11
February	1	1	1	0	0	0	0	1	0	0	0	0	0	0	0	0	0	1	0	0	1	3	1	2	0	0	0	0	0	0	0	12
March	0	2	0	0	0	0	0	0	0	0	0	0	0	0	0	0	0	1	0	2	0	3	0	6	9	10	0	3	0	0	6	42
April	7	8	8	1	8	11	8	9	10	9	10	11	0	3	8	10	9	8	9	10	10	7	0	0	3	0	10	11	7	10	0	215
May	0	7	7	7	8	0	6	0	0	9	0	11	4	4	0	0	0	0	10	4	1	0	0	4	0	0	0	0	0	5	0	87
June	0	0	0	0	0	1	0	4	0	0	0	0	0	2	0	0	0	1	0	0	0	3	0	0	0	0	0	0	0	0	0	11
July	0	0	0	0	0	0	3	4	0	0	2	0	0	1	0	3	7	0	0	1	0	0	0	0	7	0	0	0	3	0	0	31
August	2	1	0	0	0	0	0	8	0	3	0	0	0	1	0	5	4	6	7	5	0	0	0	0	0	1	6	0	0	0	2	51
September	0	1	0	0	0	0	8	9	8	10	9	9	8	6	8	5	11	4	2	7	10	7	12	5	8	10	10	9	12	10	0	198
October	8	0	8	10	9	11	10	6	0	0	8	4	7	4	0	0	5	4	5	6	2	0	0	2	7	1	0	0	1	0	0	118
November	2	0	1	7	0	0	1	0	0	0	0	1	3	0	0	0	0	0	3	4	1	0	1	2	1	4	0	4	0	0	0	35
December	1	0	0	0	0	0	0	1	5	0	0	1	3	0	1	0	0	1	0	0	0	1	0	0	0	0	0	0	0	0	1	15

Table 4-12 BeiDou phi60>0.1 occurrence in 2014

2014	1	2	3	4	5	6	7	8	9	10	11	12	13	14	15	16	17	18	19	20	21	22	23	24	25	26	27	28	29	30	31	total
January	0	0	0	0	0	0	0	0	0	0	0	0	0	0	0	0	1	0	1	0	0	0	0	1	5	7	3	1	1	0	0	20
February	4	0	0	0	3	2	0	1	0	10	0	1	2	10	7	7	7	5	0	0	0	1	9	6	5	10	11	11	0	0	0	112
March	10	10	10	10	10	8	10	10	10	9	10	8	1	9	11	10	9	10	10	6	8	9	9	10	9	8	8	10	12	11	10	285
April	10	10	8	10	9	8	9	10	10	11	3	5	0	8	9	10	9	9	10	9	5	9	5	0	0	9	1	8	8	3	0	215
May	5	1	0	0	0	10	10	0	0	3	0	0	5	2	1	9	1	3	8	10	9	2	9	1	1	0	0	0	0	0	2	92
June	2	1	0	0	0	0	0	0	0	0	0	0	2	0	0	0	0	0	0	0	1	1	0	0	1	0	0	1	1	0	0	10
July	0	0	0	0	0	0	0	0	0	0	4	0	0	0	0	5	0	0	0	0	0	0	0	0	0	0	0	3	0	0	0	12
August	0	5	6	0	2	3	9	0	4	0	3	0	0	0	0	0	4	6	0	0	0	0	0	3	0	0	0	0	0	6	0	51
September	9	5	7	0	0	5	0	10	10	10	0	1	10	8	10	9	10	9	0	10	8	3	9	1	0	4	0	9	8	1	0	166
October	0	0	0	0	0	0	0	0	0	0	0	0	0	0	0	0	0	0	0	0	0	0	0	0	0	0	0	0	0	0	0	0
November	0	0	0	0	0	0	0	0	0	0	0	0	0	0	0	0	0	0	0	0	0	0	0	0	0	0	0	0	0	0	0	0
December	0	0	0	0	0	0	0	0	0	0	0	0	0	0	0	0	0	0	0	0	0	0	0	0	0	0	0	0	0	0	0	0

Figure 4-21 and Figure 4-22 show the monthly and daily occurrence of ROTI larger than 0.2 indicating TEC perturbations for years 2013 and 2014. Similar to S4 and phi60 parameter, the months of March/April and September/October of both years also exhibit the highest number of occurrence.

Table 4-13 and Table 4-14 show a more detailed number of occurrence of ROTI larger than 0.2 for years 2013 and 2014, respectively. For both years, highest occurrence of ROTI larger than 0.2 is again observed in months March/April and September/October.

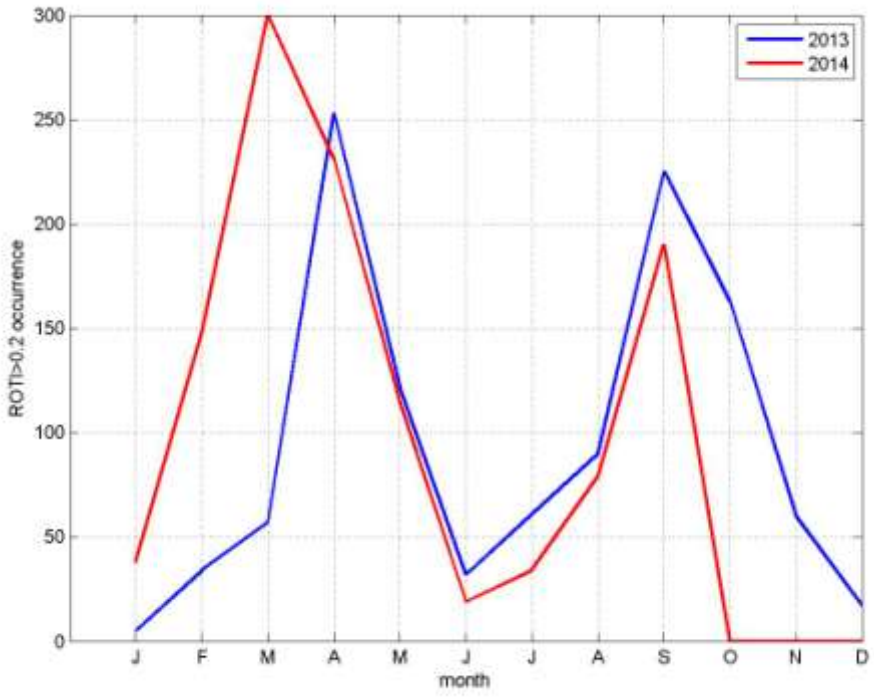

Figure 4-21 Monthly occurrence of BeiDou ROTI>0.2

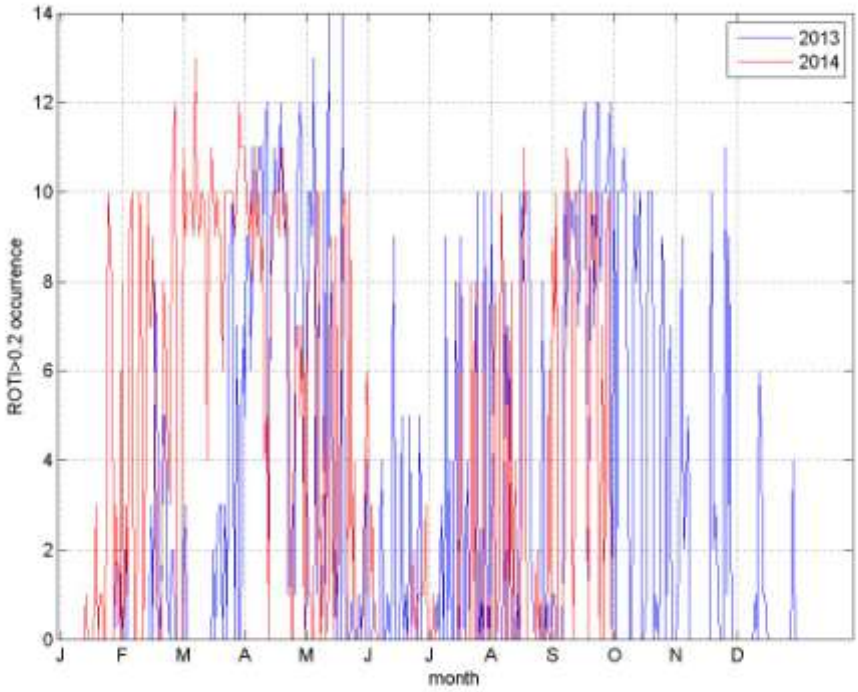

Figure 4-22 Daily occurrence of BeiDou ROTI>0.2

Table 4-13 BeiDou ROTI>0.2 occurrence in 2013

2013	1	2	3	4	5	6	7	8	9	10	11	12	13	14	15	16	17	18	19	20	21	22	23	24	25	26	27	28	29	30	31	total
January	0	0	0	0	0	0	0	0	0	0	0	0	0	0	0	0	0	0	0	0	0	0	0	0	0	0	0	0	1	2	2	5
February	0	1	2	0	0	0	0	0	0	0	0	0	0	0	0	3	0	8	4	0	1	5	5	1	0	2	2	0	0	0	0	34
March	0	3	0	0	0	0	0	0	0	0	0	0	0	0	0	2	0	2	3	3	0	3	0	8	9	10	0	7	0	0	7	57
April	5	9	9	6	11	11	9	11	11	9	11	12	1	8	9	11	10	10	12	10	9	10	1	1	3	1	10	11	12	10	0	253
May	1	10	10	9	13	1	9	0	1	10	1	14	7	8	0	2	0	0	14	2	0	0	0	1	0	0	0	1	0	3	4	121
June	0	0	0	1	0	0	0	4	0	0	1	0	1	9	0	0	0	5	0	1	0	5	0	0	0	0	5	0	0	0	0	32
July	0	0	0	0	1	0	3	0	9	0	4	0	0	8	1	0	9	1	0	4	0	0	0	0	10	0	1	0	10	0	0	61
August	10	3	0	0	0	0	1	8	0	7	0	0	0	1	0	10	8	10	10	10	2	1	0	0	0	0	8	0	1	0	0	90
September	1	1	0	0	0	0	10	7	10	10	9	10	10	7	10	11	12	7	0	8	10	7	12	12	8	10	10	10	11	12	0	225
October	11	0	10	10	10	11	10	3	0	0	10	8	9	10	0	0	1	10	10	10	0	1	0	1	9	8	0	4	7	0	0	163
November	0	1	2	9	2	3	5	0	0	0	0	0	0	0	0	0	0	0	10	2	3	2	0	0	0	11	1	9	0	0	0	60
December	0	0	0	0	0	0	0	0	0	1	0	6	4	1	1	0	0	0	0	0	0	0	0	0	0	0	0	0	4	0	0	17

Table 4-14 BeiDou ROTI>0.2 occurrence in 2014

2014	1	2	3	4	5	6	7	8	9	10	11	12	13	14	15	16	17	18	19	20	21	22	23	24	25	26	27	28	29	30	31	total
January	0	0	0	0	0	0	0	0	0	0	0	0	0	1	0	0	0	0	3	0	1	1	0	0	10	9	8	0	3	2	0	38
February	8	0	3	1	9	10	0	0	2	10	9	0	4	10	7	7	9	4	0	0	0	8	7	5	3	9	11	12	0	0	0	148
March	11	9	10	10	10	9	13	10	9	10	10	9	4	9	11	10	9	10	9	9	6	10	10	10	10	10	9	10	12	11	11	300
April	11	10	9	10	8	11	9	10	8	9	4	5	0	9	10	10	10	9	11	11	9	10	7	0	0	5	7	7	5	7	0	231
May	8	1	1	0	0	10	10	0	2	5	0	1	9	3	0	9	1	5	9	10	9	0	10	1	4	0	0	0	0	0	6	114
June	5	1	3	1	0	0	0	0	0	0	0	0	0	0	0	0	0	0	0	0	0	0	0	2	0	1	1	1	1	3	0	19
July	0	0	1	0	0	0	0	0	0	0	0	0	0	0	0	8	0	0	0	0	0	8	0	8	0	0	0	8	0	0	1	34
August	0	6	8	0	1	10	8	0	7	0	8	0	4	0	0	0	11	7	0	0	0	0	0	2	0	1	0	0	0	6	0	79
September	9	7	10	0	0	1	2	11	10	10	0	3	10	10	10	10	10	10	0	10	10	8	10	2	0	7	0	9	10	1	0	190
October	0	0	0	0	0	0	0	0	0	0	0	0	0	0	0	0	0	0	0	0	0	0	0	0	0	0	0	0	0	0	0	0
November	0	0	0	0	0	0	0	0	0	0	0	0	0	0	0	0	0	0	0	0	0	0	0	0	0	0	0	0	0	0	0	0
December	0	0	0	0	0	0	0	0	0	0	0	0	0	0	0	0	0	0	0	0	0	0	0	0	0	0	0	0	0	0	0	0

To conclude for this section, based on BeiDou monitored data, ionospheric scintillation peak usually happen in around March/April and September/October (equinox) for both years 2013 and 2014. Generally, high S4 will also correspond to higher phi60 and ROTI values. These results are in consistent with the GPS and GLONASS data presented in the earlier section.

4.3.2. BeiDou Equinox Scintillation

To get closer study during equinox months, the monthly S4, phi60, and ROTI average of BeiDou satellites are computed where those parameters are averaged over all visible BeiDou satellites in every minute. The visible satellites are only limited to those having elevation angle more than 20 degrees to filter out fluctuation due to multipath effects.

Figure 4-23 to Figure 4-25 show the monthly S4, phi60, and ROTI average of visible BeiDou satellites during the equinox months of March, April, September and October 2013. The *y* and *x* axes for each subplot represent the day (1^{st} to 30^{th} or 31^{st}) and local time (8 a.m. to 8 a.m. next day) in each month. It can be observed that in equinox months, relatively high scintillation is present in reasonably high number of days which agrees with GPS and GLONASS outcome presented in previous section. This is attributed to the close alignment of the solar terminator with magnetic meridian [41].

Similarly to GPS and GLONASS result, these scintillation events occur mostly around local time of 8 p.m. to 12 a.m, which is during the post sunset period. This is attributed to the eastward prereversal enhancement (PRE) electric field, which is coupled with the earth's geomagnetic field to produce an upward vertical force derived from $\boldsymbol{E} \times \boldsymbol{B}$. The upward vertical force results in steep gradient of ion and electron densities between upper and lower layer, thereby producing plasma bubble irregularities arising from Rayleigh-Taylor instability process [4].

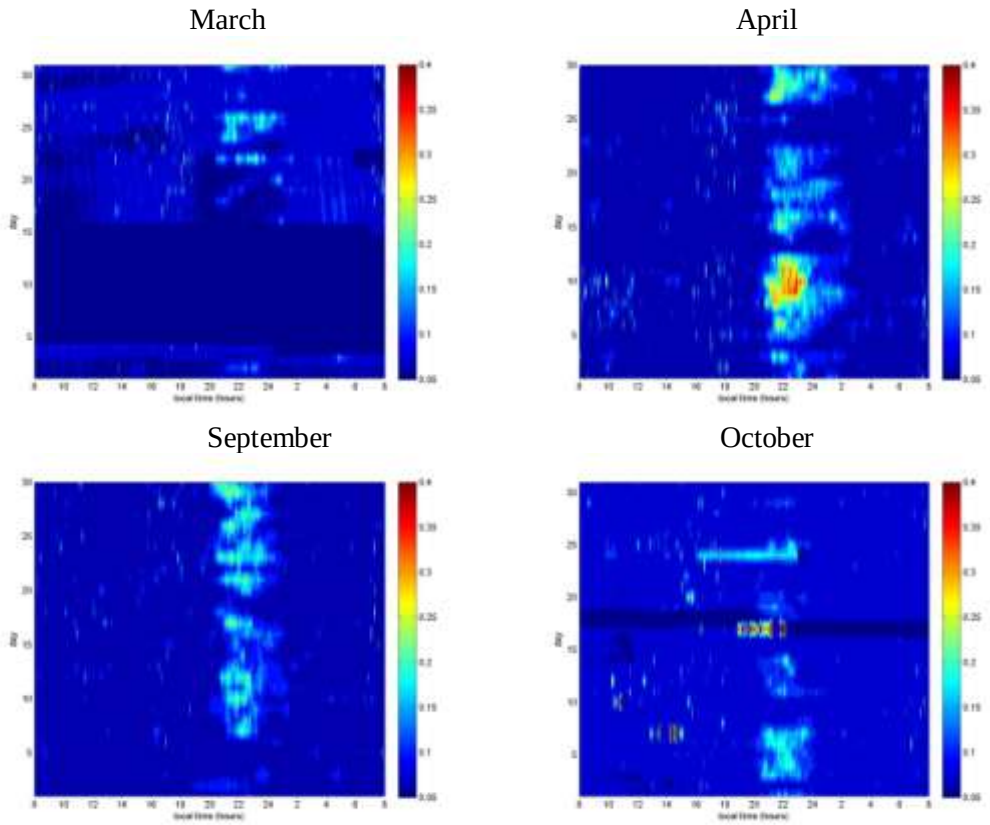

Figure 4-23 Monthly BeiDou S4 average during the equinox months of year 2013

March

April

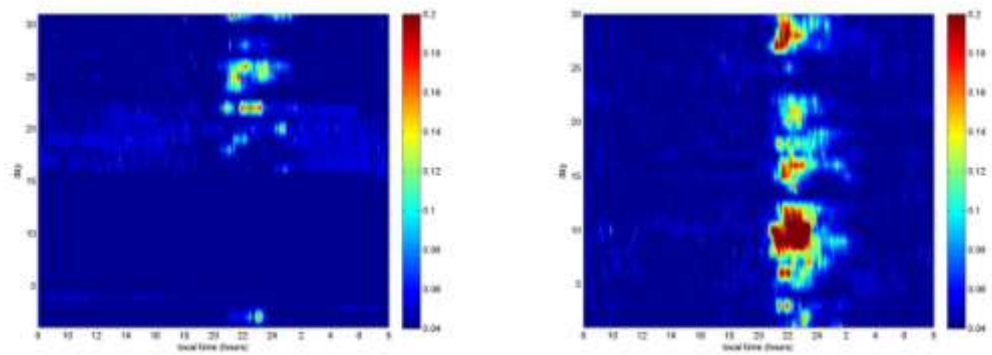

September

October

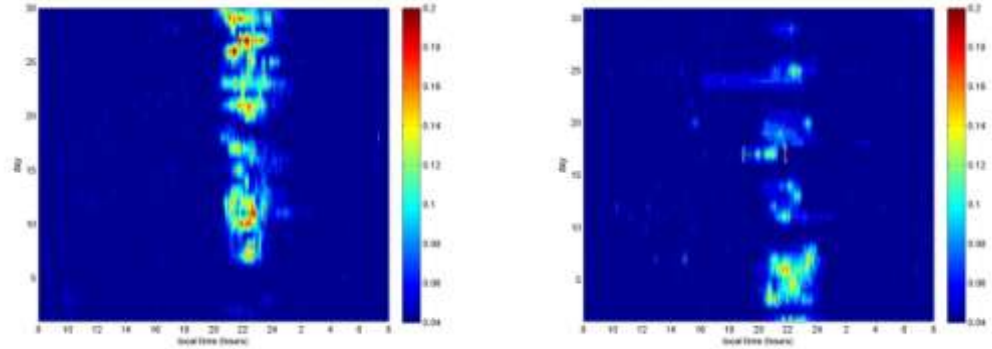

Figure 4-24 Monthly BeiDou Phi60 average during the equinox months of year 2013

March

April

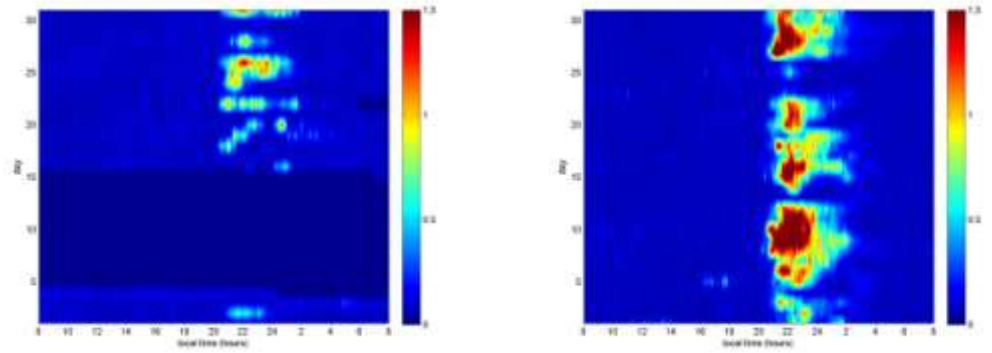

September

October

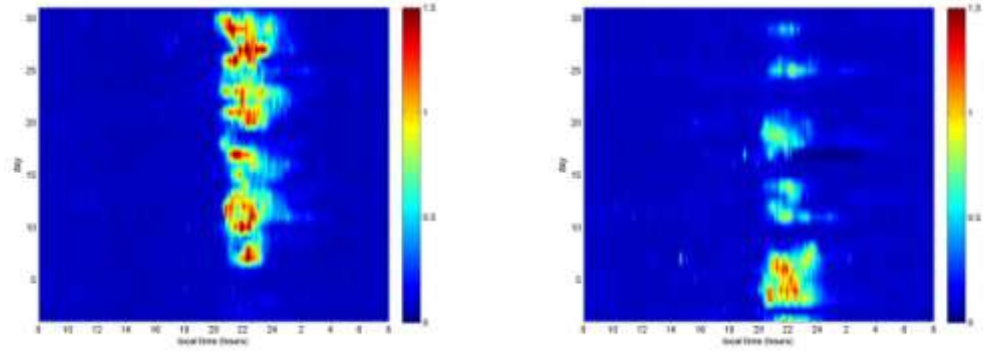

Figure 4-25 Monthly BeiDou ROTI average during the equinox months of year 2013

4.4. L2 Frequencies Analysis

The study of ionospheric scintillation has been done in the earlier section using first frequency (L1 for GPS and GLONASS, B1 for BeiDou) only. In this section the ionospheric scintillation on GNSS second frequency (L2 for GPS and GLONASS, B2 for BeiDou) will be discussed. In this thesis BeiDou B2 frequency is also called L2 for easier naming. Table 4-15 shows the center frequency of various GNSS signal. For GLONASS which is using frequency division multiple access (FDMA), *n* represents the frequency channel. For most GNSS, the third frequency (L3 or L5) is not fully available yet so it is not discussed in this thesis.

Table 4-15 Center frequency of various GNSS signals

Signal Type	Center Frequency (MHz)
GPS L1	1575.42
GPS L2	1227.60
GPS L5	1176.45
GLONASS L1	$1602.00 + n \times 0.5625$
GLONASS L2	$1246.00 + n \times 0.4375$
GLONASS L3	1202.025
BeiDou B1	1561.098
BeiDou B2	1207.14
Galileo L1	1575.42
Galileo E5a	1176.45
Galileo E5b	1207.14
Galileo E5	1191.795

Two scintillation days, 11 and 14 March 2014 are selected to compare the average S4 of L1 and L2 frequencies of GPS, GLONASS, and BeiDou shown in Figure 4-26 to Figure 4-31. Data of GPS L2 is obtained from L2c (civilian) signal which only has 13 satellites available (PRN 1, 5, 6, 7, 12, 15, 17, 24, 25, 27, 29, 30, 31) in year 2014. GLONASS L2 signals are available from all 24 satellites. BeiDou B2 signals are also available from all orbiting BeiDou satellites.

Figure 4-26 and Figure 4-27 show the S4 average obtained from GPS satellites, Figure 4-28 and Figure 4-29 is the S4 average from GLONASS, while Figure 4-30 and Figure 4-31 is from BeiDou. Observation from all of the figures shows that S4 in L2 frequency is consistently higher than S4 in L1. This indicates that ionospheric scintillation is inversely proportional to signal frequency.

The phi60 averages from the same days are also plotted for observation. Figure 4-32 and Figure 4-33 show the phi60 obtained from GPS satellites. It is seen that phi60 from L2 is higher than phi60 from L1 frequency. Figure 4-34 and Figure 4-35 show the phi60 from GLONASS while Figure 4-36 and Figure 4-37 show the phi60 from BeiDou. In GLONASS and BeiDou, the L2 phi60 is seen as slightly higher than L1 frequency during scintillation time. During quiet time, L1 and L2 phi60 show very close magnitude probably due to high noise.

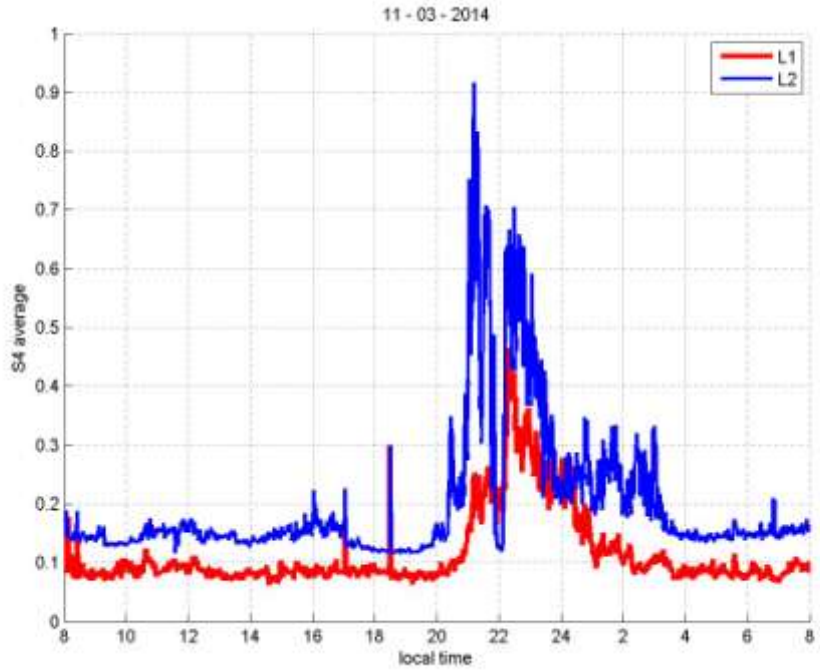

Figure 4-26 GPS L1 and L2 S4 average on 11 March 2014

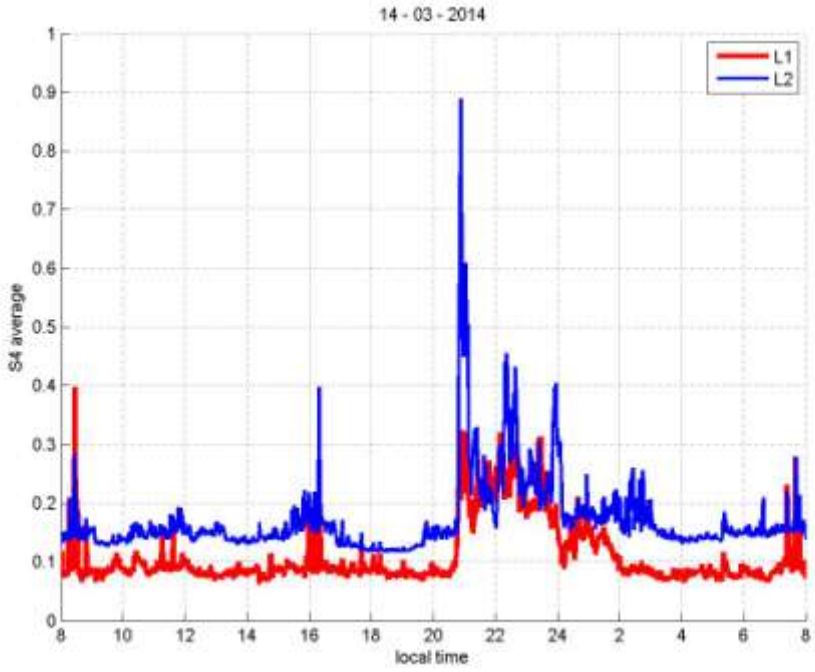

Figure 4-27 GPS L1 and L2 S4 average on 14 March 2014

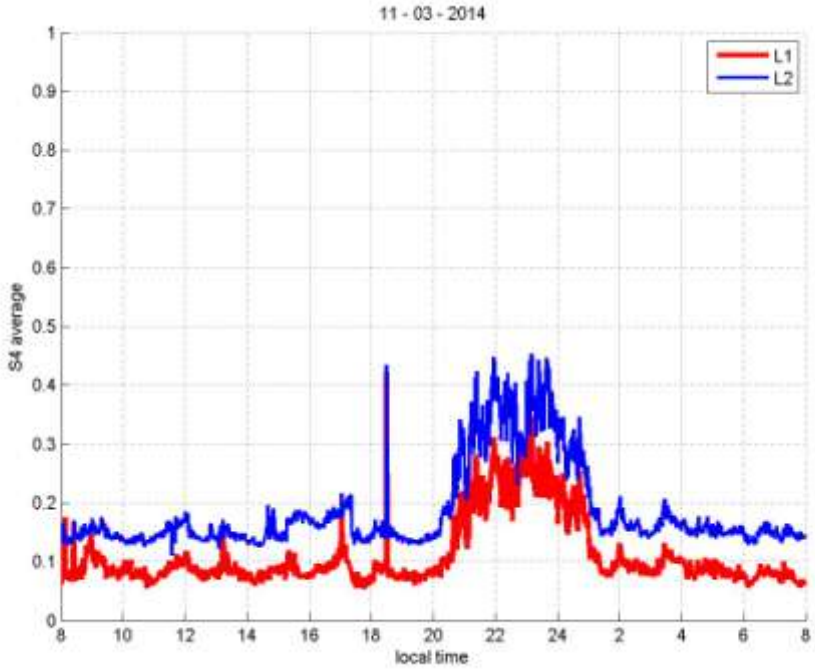

Figure 4-28 GLONASS L1 and L2 S4 average on 11 March 2014

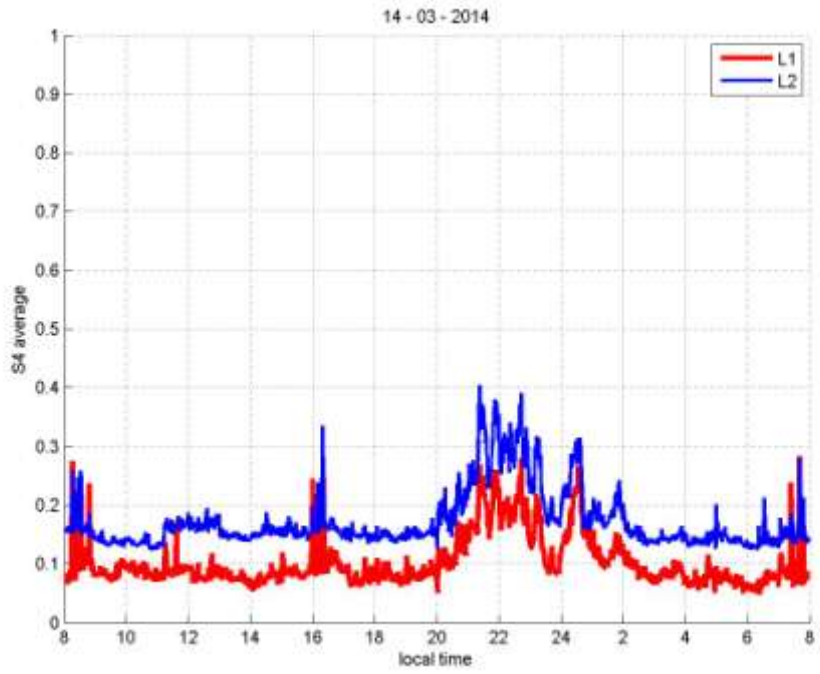

Figure 4-29 GLONASS L1 and L2 S4 average on 14 March 2014

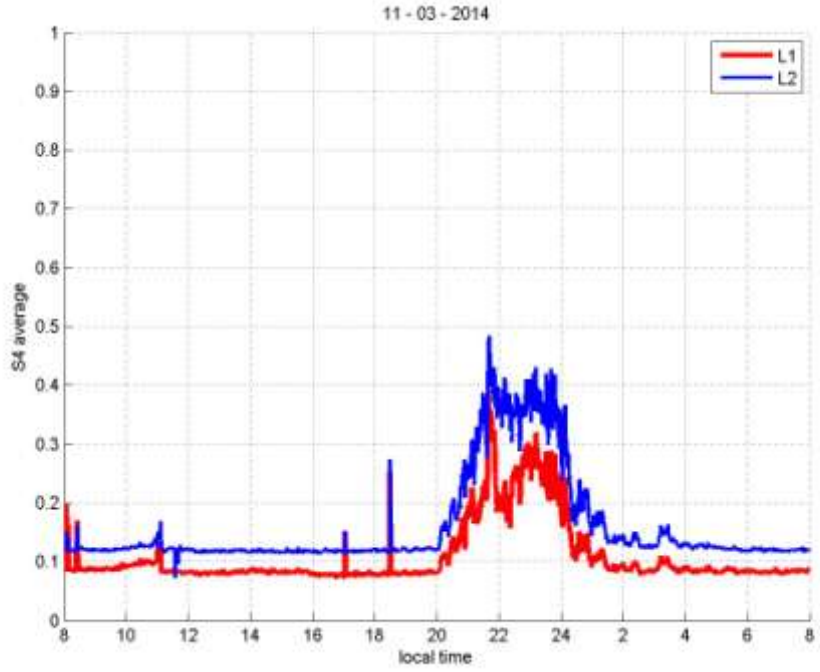

Figure 4-30 BeiDou L1 and L2 S4 average on 11 March 2014

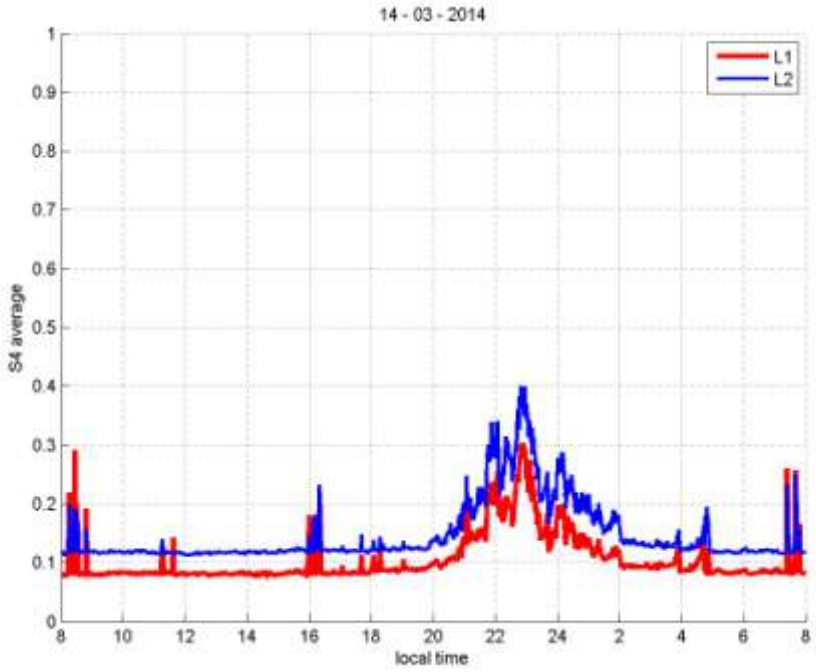

Figure 4-31 BeiDou L1 and L2 S4 average on 14 March 2014

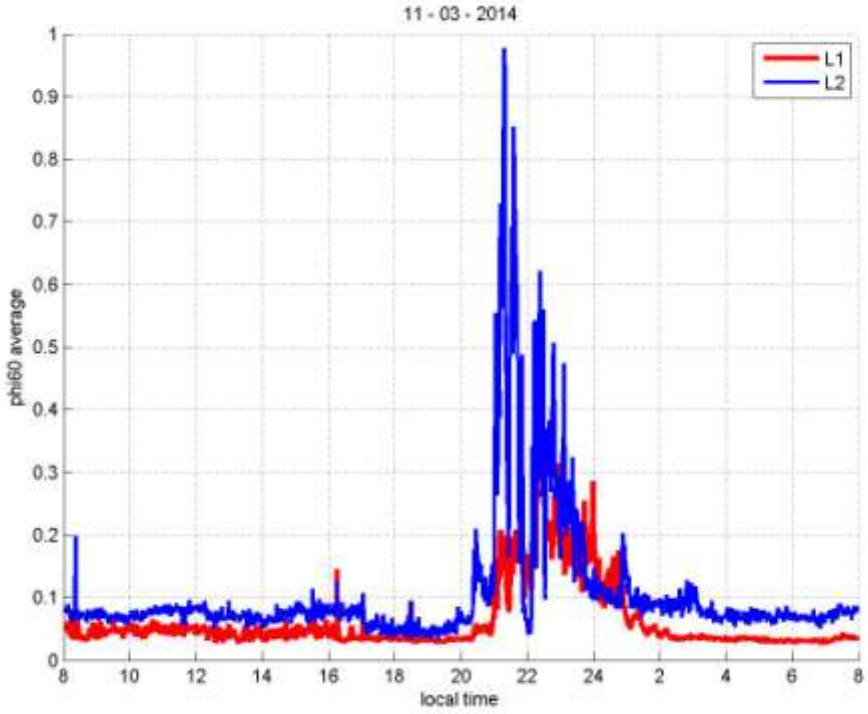

Figure 4-32 GPS L1 and L2 Phi60 average on 11 March 2014

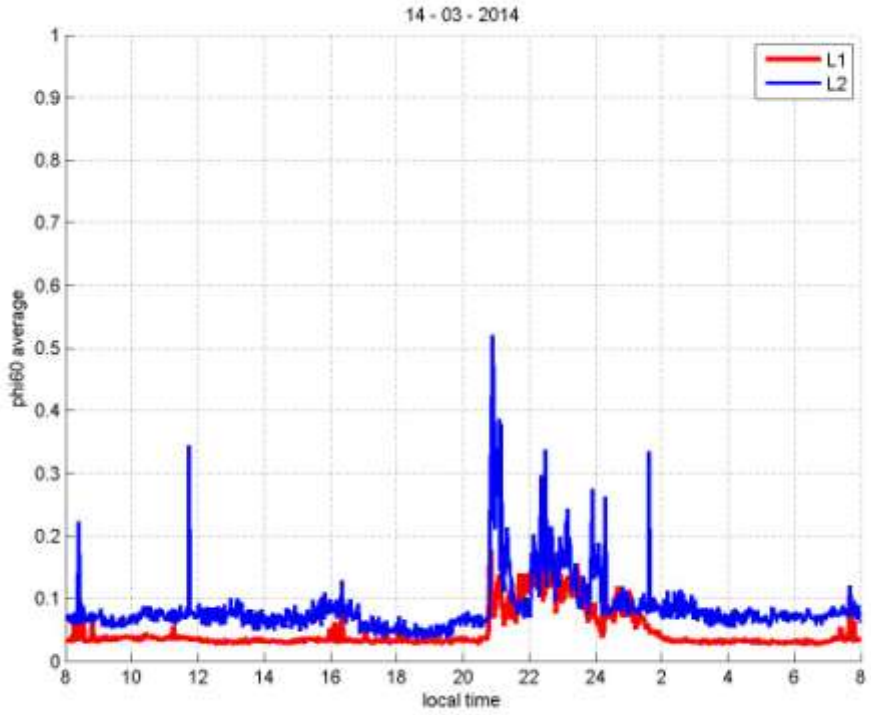

Figure 4-33 GPS L1 and L2 Phi60 average on 14 March 2014

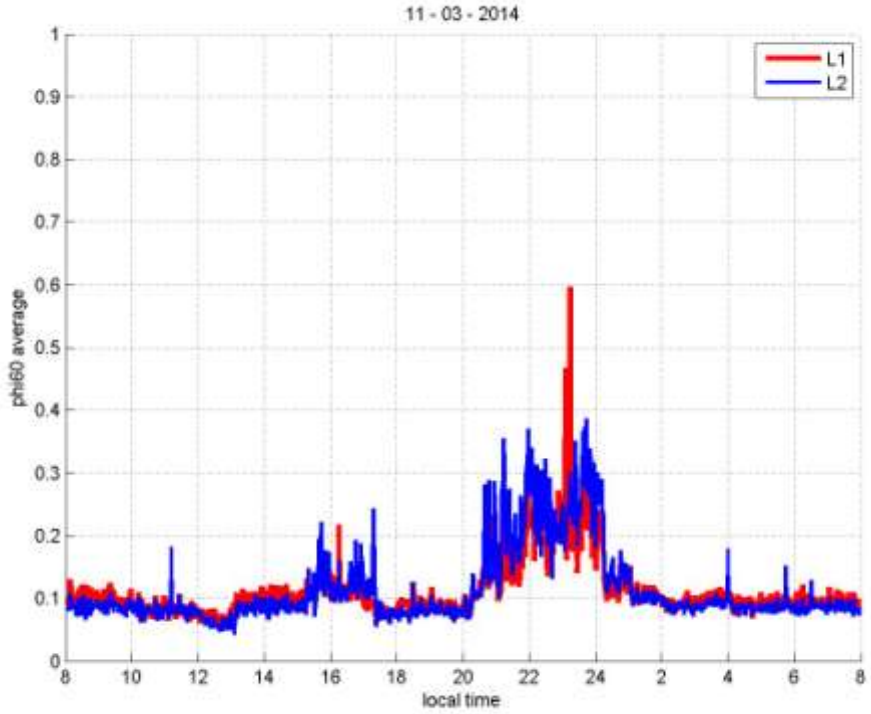

Figure 4-34 GLONASS L1 and L2 Phi60 average on 11 March 2014

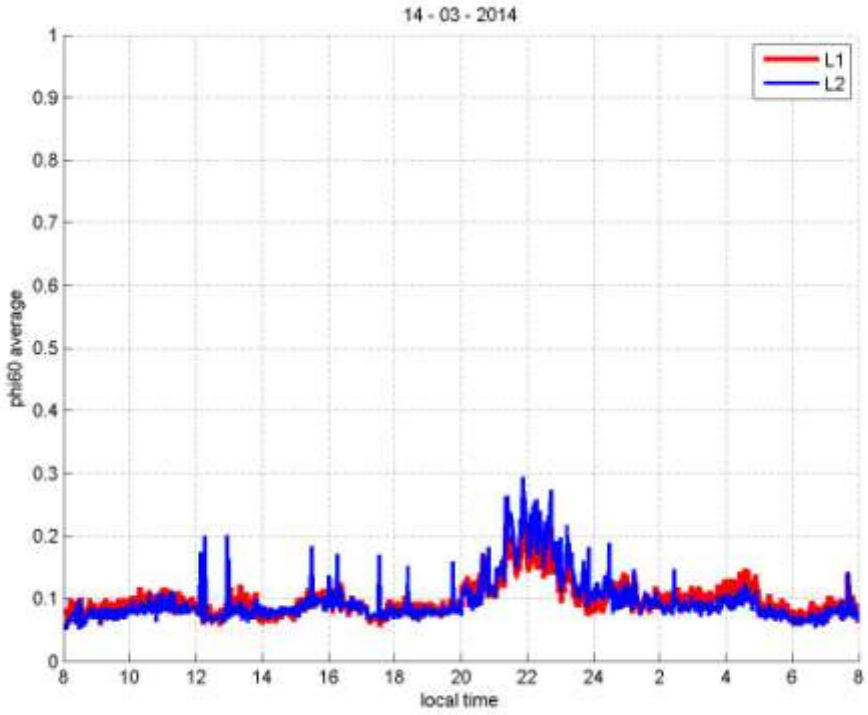

Figure 4-35 GLONASS L1 and L2 Phi60 average on 14 March 2014

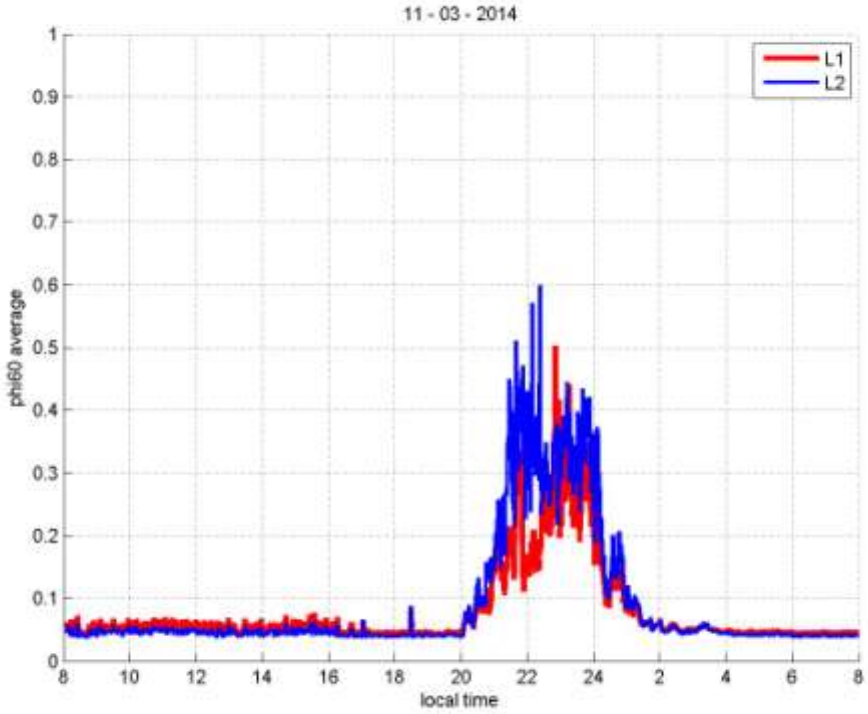

Figure 4-36 BeiDou L1 and L2 Phi60 average on 11 March 2014

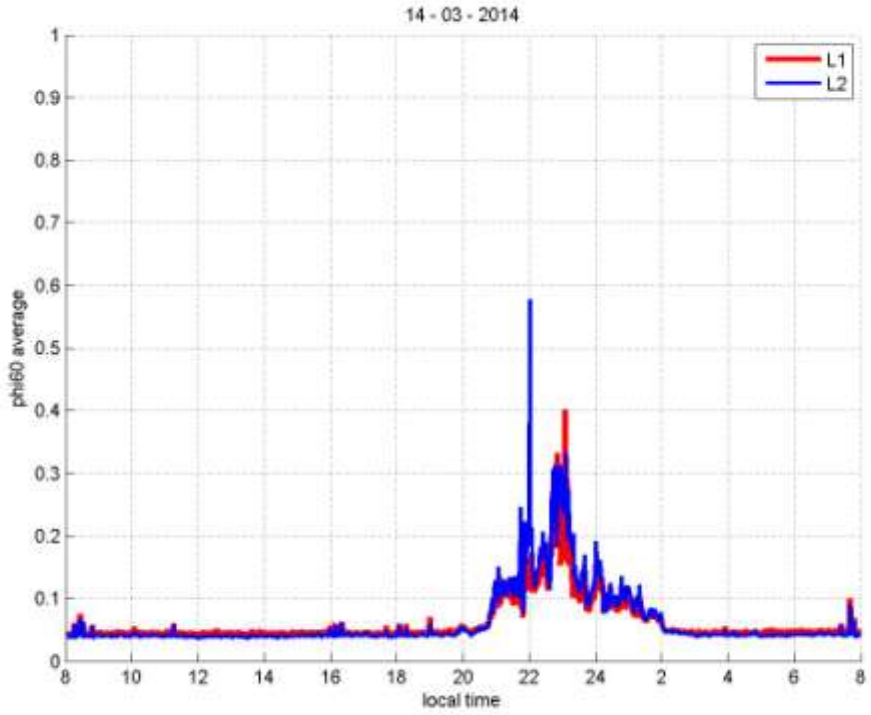

Figure 4-37 BeiDou L1 and L2 Phi60 average on 14 March 2014

To further study the relation between L1 and L2 frequency, S4 of L2 frequency is plotted against S4 of L1 for all satellites in Figure 4-38 to Figure 4-40. The fitted line of each figure is then plotted using robust least square method performed by Matlab which is shown by the green lines. Only S4 higher than 0.2 are used for the fitted line computation to minimize the noise effect. The same method is also done for phi60 in Figure 4-41 to Figure 4-43. For phi60, only those higher than 0.1 are used for the fitted line computation, except that GLONASS uses 0.2 as the limit due to higher phase noise.

Reference [63] predicted the relation of ionospheric scintillation effect in any frequency as follows:

$$S4(f) = S4_{L1}\left(\frac{f_{L1}}{f}\right)^{1.5} \quad (4\text{-}1)$$

$$phi60(f) = phi60_{L1}\frac{f_{L1}}{f} \quad (4\text{-}2)$$

where *f* is any frequency targeted.

These equations are applied to S4 and phi60 of L1 and L2 frequencies and they yield the blue lines that are shown in Figure 4-38 to Figure 4-43. It can be seen that the phi60 fitting lines from GPS, GLONASS, and BeiDou closely follow the aforementioned prediction. However, apparent differences are shown by the obtained S4 fitting lines and the prediction formula. For GPS the following frequency relationship is shown by the fitting line:

$$S4_{L2} = S4_{L1}\left(\frac{f_{L1}}{f_{L2}}\right)^{1.1193} \quad \textbf{(4-3)}$$

For GLONASS the fitted line shows relationship as follows:

$$S4_{L2} = S4_{L1}\left(\frac{f_{L1}}{f_{L2}}\right)^{1.3443} \quad \textbf{(4-4)}$$

For BeiDou the fitted line shows relationship as follows:

$$S4_{L2} = S4_{L1}\left(\frac{f_{L1}}{f_{L2}}\right)^{1.0236} \quad \textbf{(4-5)}$$

In average, the relationship between S4 in L1 and L2 is:

$$S4_{L2} = S4_{L1}\left(\frac{f_{L1}}{f_{L2}}\right)^{1.1624} \quad \textbf{(4-6)}$$

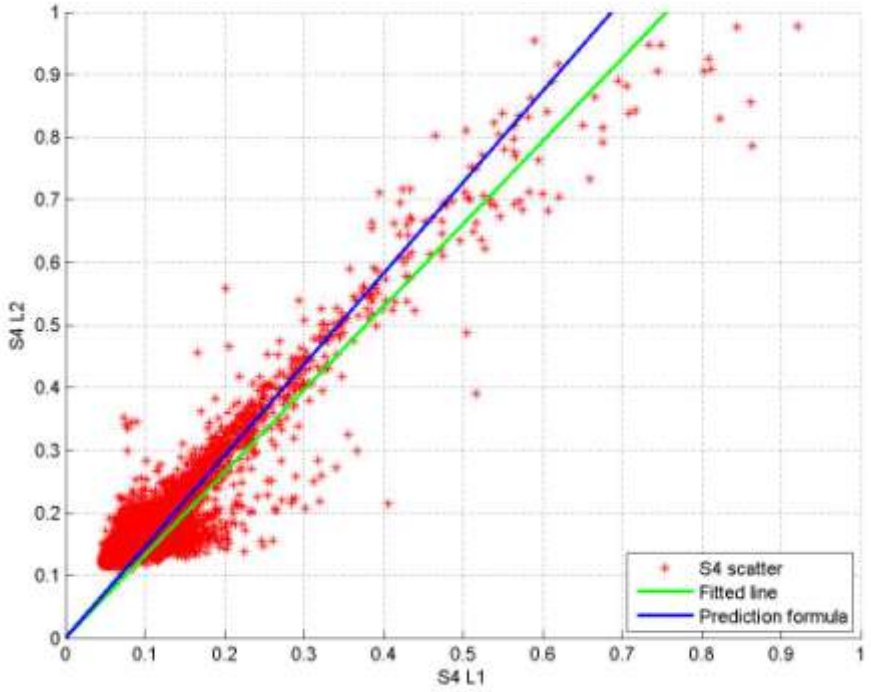

Figure 4-38 Scatter plot of GPS S4 L1 and L2

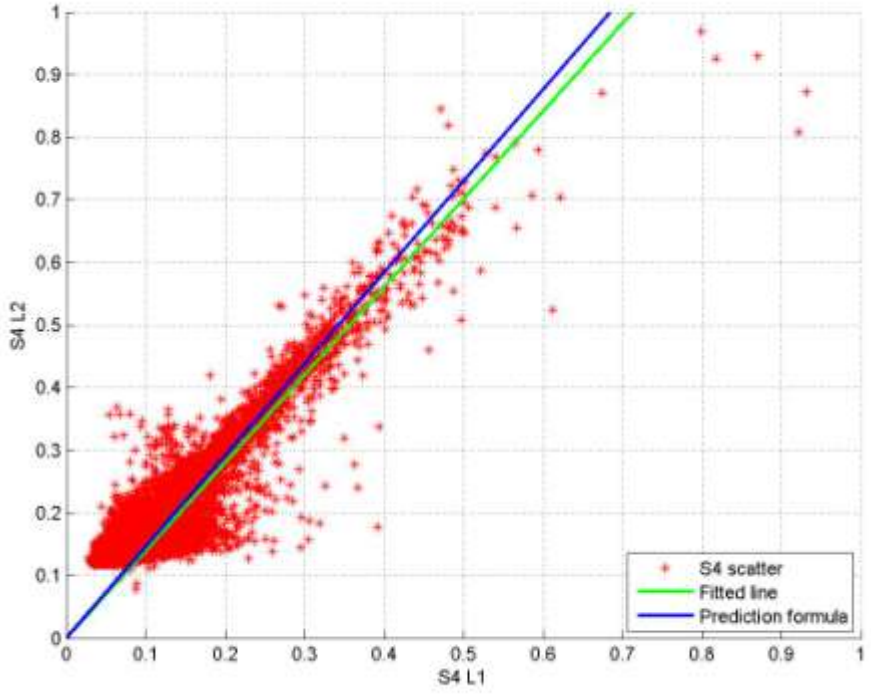

Figure 4-39 Scatter plot of GLONASS S4 L1 and L2

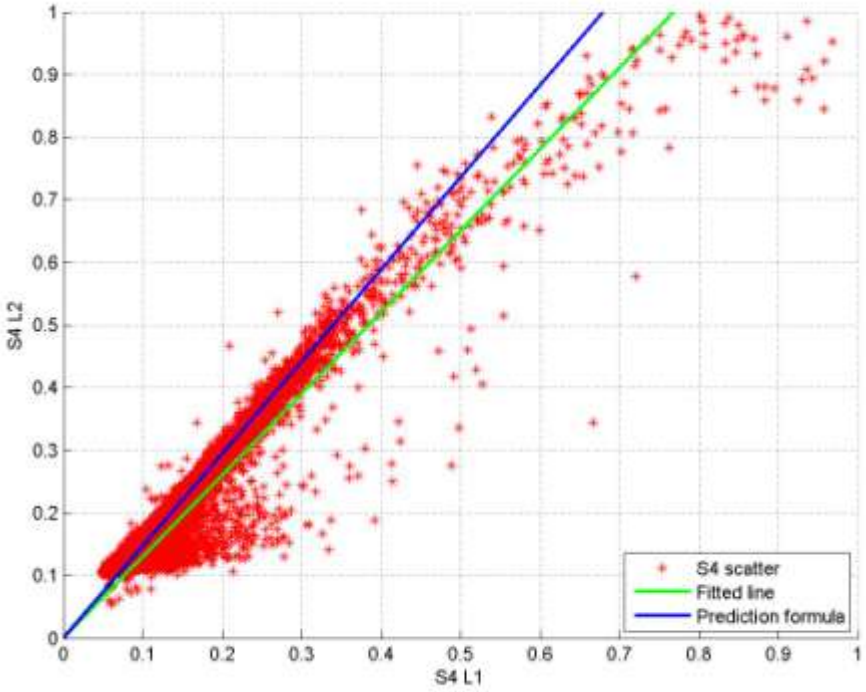

Figure 4-40 Scatter plot of BeiDou S4 L1 and L2

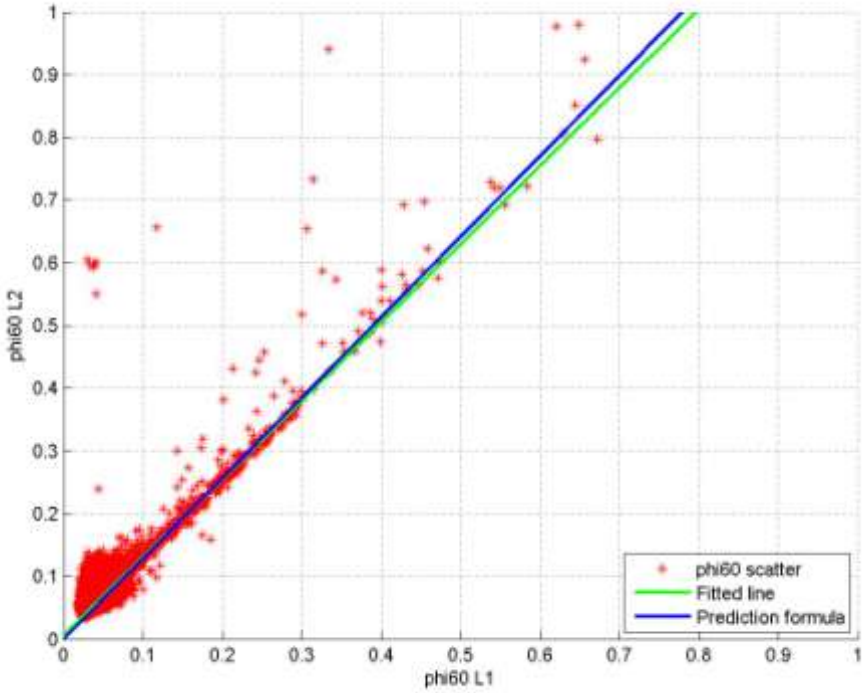

Figure 4-41 Scatter plot of GPS Phi60 L1 and L2

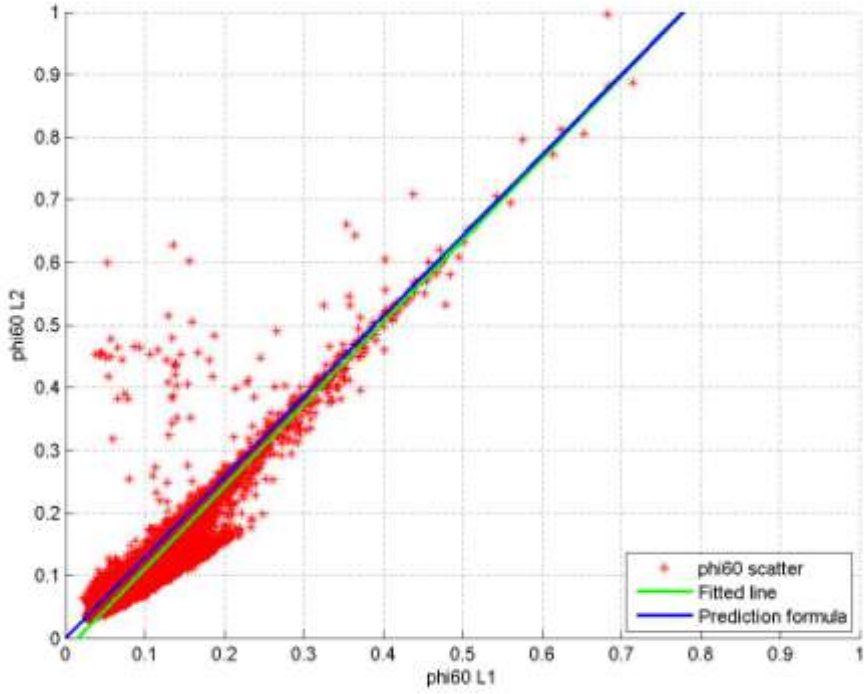

Figure 4-42 Scatter plot of GLONASS Phi60 L1 and L2

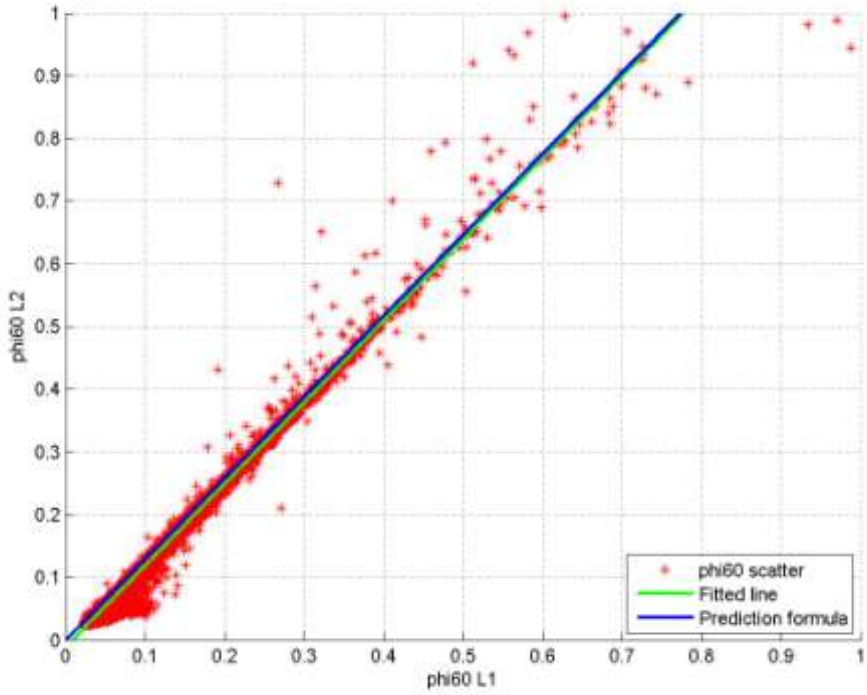

Figure 4-43 Scatter plot of BeiDou Phi60 L1 and L2

5. Raw GPS Signal Processing for Ionospheric Scintillation Studies

The commercial Septentrio PolaRxS receiver only gives processed information of GNSS signal. To observe more closely into the ionospheric scintillation affected signal, raw baseband GNSS signal is needed. By collecting such raw signals, it is possible to process them using fully digital processing by which further analysis on the acquisition, tracking, and positioning can be made. Such digital processing is very powerful and flexible as it is able to process multi frequencies and multi satellite constellations such as GPS, GLONASS, BeiDou, Galileo, and SBAS. We can obtain various ionospheric scintillation related parameters such as S4, phi60, and C/N_0 by our own algorithm which in the case of commercial receiver we cannot fully control. We can also easily test the performance of new receiver design and modify some of the parameters such as tracking bandwidth, phase lock loop (PLL), and delay lock loop (DLL). Testing of new receiver design against ionospheric scintillation can also be done. Finally, it can help to design a smart GNSS receiver which is robust to scintillation, by detecting and adapting to such disturbance.

This section presents an initial stage of raw GNSS data collection and processing. Only GPS L1 data is done in this initial work. Raw baseband GPS L1 C/A signal is recorded using National Instrument (NI) PXI equipment. The antenna used is multi frequency Septentrio PolaNt-x. The recording system is shown in Figure 5-1 and Figure 5-2. To get good comparison, raw signal input to NI PXI and Septentrio receiver is obtained from one antenna which is split into two branches equally by T junction splitter as shown in Figure 5-1. Mini circuit ZFL-2500 amplifier is used to amplify the RF signal before entering the NI PXI equipment. Gain at 1575.42 MHz is around 32 dB. It is powered by 5V DC and 220 mA (maximum) current.

The GPS L1-C/A signal centered at 1575.42 MHz having bandwidth of 2 MHz is recorded with sampling rate of 3.125 MHz using complex sampling. The raw baseband signal is then processed by software defined GPS receiver program that is written in Matlab.

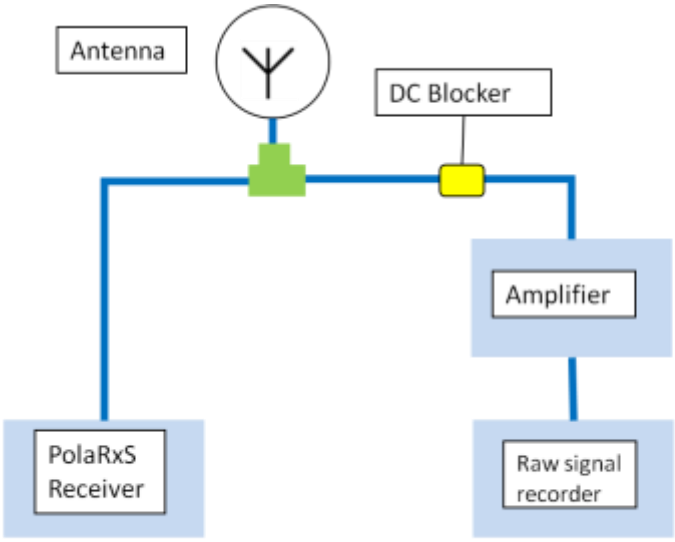

Figure 5-1 Raw baseband signal recording system diagram

Figure 5-2 NI PXI raw baseband signal recording system

5.1. Software Defined GPS Receiver

GPS receiver consists of two parts which are RF front end and digital processing. RF front end used here is the aforementioned baseband signal recorder which includes Septentrio PolaNt-x and NI PXI equipment as the main components. The software

defined GPS receiver is used to do the digital processing of GPS baseband/IF raw signal. The program consists of three parts:

- Signal acquisition
- Signal tracking
- Navigation solution (not presented here)

The Matlab program used to process this raw signal is based on the software defined GPS receiver provided by reference [64]. Some modifications are made to extract certain outputs needed for ionospheric scintillation studies. The flow diagram of the program is shown in Figure 5-3. It starts with checking parameters, plotting raw data, and defining the processing to be done. The subsequent steps are signal acquisition, tracking, and position/navigation solution. Navigation solution is not presented in this report.

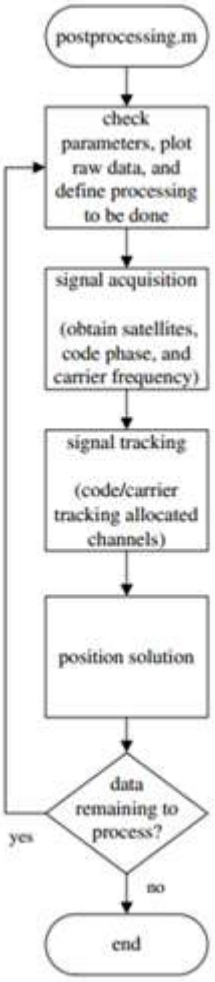

Figure 5-3 GNSS processing flow diagram

5.1.1. Signal Acquisition

This step determines visible satellites and coarse values of carrier frequency and code phase of the satellite signals. There are three methods to get the Doppler shift and code phase:

- Serial Search Acquisition
- Parallel Frequency Space Search Acquisition
- Parallel Code Phase Search Acquisition (used in this software)

The block diagram of Parallel Code Phase Search Acquisition is shown in Figure 5-4 [64]. The incoming signal is multiplied by a locally generated carrier complex signal and then transformed into the frequency domain. The generated PRN code is also transformed into the frequency domain and the result is complex conjugated. Those two signals in frequency domain are then multiplied and transformed back into time domain. The absolute value of the output represents the correlation between the input signal and the replicated PRN code. If a peak is present in the correlation, the index of this peak marks the PRN code phase of the incoming signal. These steps are repeated with other locally generated carrier frequencies until a peak is found.

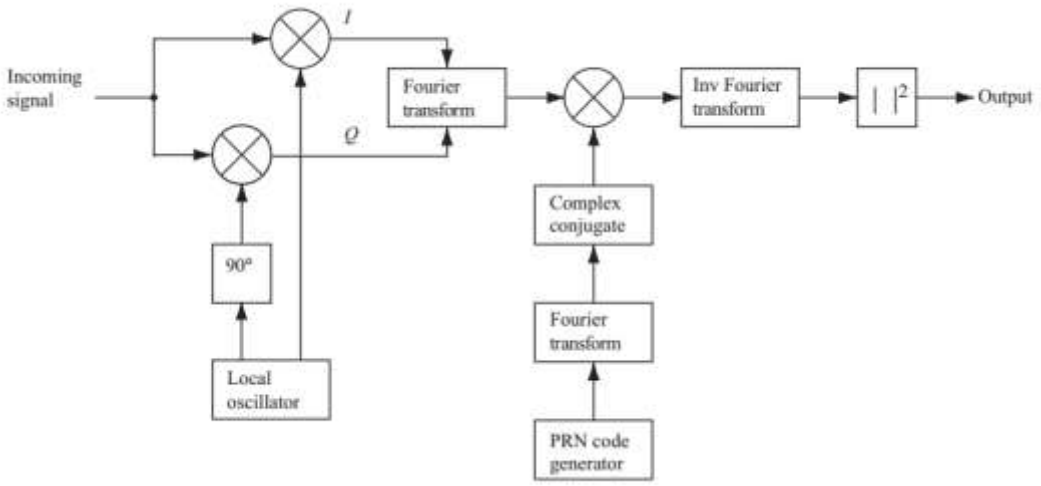

Figure 5-4 Parallel code phase search acquisition

5.1.2. Signal Tracking

This part is the main step to obtain the data needed to calculate the ionospheric scintillation parameters. The acquisition provides only rough estimates of the frequency and code phase parameters. The main purpose of tracking is to refine these values, keep track, and demodulate the navigation data. The output is the correlator output (I_n and Q_n) which is needed to calculate signal intensity, S4, and C/N_0. Another output is carrier phase which is needed to calculate phase scintillation. Tracking consists of two parts:

- Carrier phase tracking
- Code phase tracking

The block diagram of Carrier and Code Phase is shown in Figure 5-5 [64]. Phase locked loop (PLL) and delay locked loop (DLL) are integrated into one system to make sure that both carrier phase and code phase are tracked concurrently. The DLL used here is early-late tracking loop. It correlates the baseband input signal with three replicas of the PRN code generated with a spacing of ±1/2 chip. The three correlation outputs I_E (early), I_P (prompt), and I_L (late) are then used by the discriminator to adjust the phase of the PRN code replicas.

In this thesis, Costas loop is used as PLL. One property of this loop is that it is insensitive for 180^0 phase shifts and hereby it is insensitive for phase transitions due to navigation bits. As shown in Figure 5-5, local carrier wave is multiplied with the input signal to wipe off the carrier frequency. The discriminator is used to find the phase error on the local carrier wave. The output of the discriminator, which is the phase error, is then filtered and used as a feedback to the numerically controlled oscillator (NCO), which adjusts the frequency and phase of the local carrier wave. The goal of the Costas loop is to try to keep all energy in the *I* (in-phase) arm.

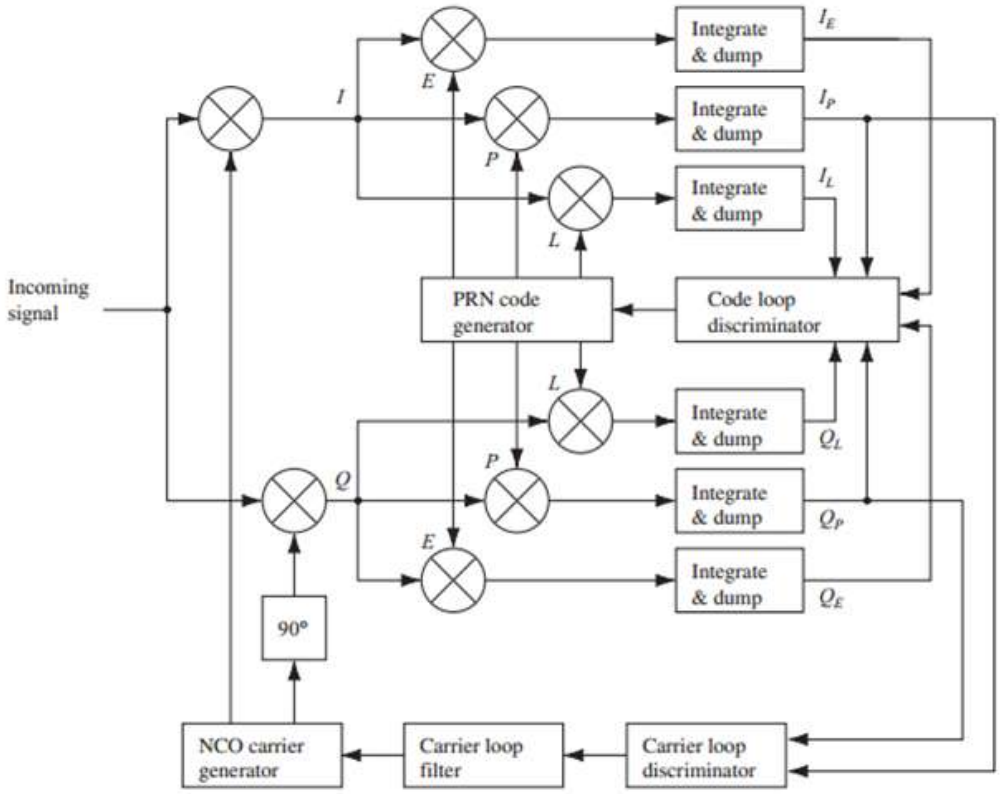

Figure 5-5 Carrier and code phase tracking

5.1.3. Ionospheric Scintillation Parameter from Raw Signal

Some ionospheric scintillation related parameters such as signal intensity (SI) and S4 can be obtained by processing the recorded raw signal. Reference [49] provides a way to calculate SI as shown below:

$$SI_k = \frac{(NBP - WBP)_k}{(NBP - WBP)_{lpf,k}} \qquad \textbf{(5.1)}$$

$$WBP_k = \left[\sum_{n=1}^{M}(I_n^2 + Q_n^2)\right]_k \qquad \textbf{(5.2)}$$

$$NBP_k = \left(\sum_{n=1}^{M} I_n\right)_k^2 + \left(\sum_{n=1}^{M} Q_n\right)_k^2 \qquad (5.3)$$

Usually M=20 which is equal to the number of C/A code periods in a GPS navigation message data bit, and k represents the data bit number. WBK is wide band power and NBP is narrow band power. I_n and Q_n are the output of the correlator (referred by I_p and Q_p in the tracking flow diagram) which is proportional to signal amplitude.

The received power is normally detrended by filtering the intensity measurements with a low-pass filter (sixth-order Butterworth with 0.1Hz cut off frequency) [20][65] and then the normalization is accomplished by dividing the raw signal intensity by the output of the low-pass filter, denoted by subscript *lpf* in (5.1). Not properly chosen detrending cut off frequency (f_c) can lead to distorted scintillation quantification. Too low f_c will lead to overestimation of scintillation index due to the effect of not completely removed satellite's motion. On the other hand, too high f_c will result in underestimated scintillation index because the scintillation component of the signal will be partly removed by the filter. This effect of f_c is more significant on phase scintillation rather than amplitude scintillation, especially at high latitude during geomagnetic storm [43]. Another way of detrending signal intensity is by replacing the low pass filter with average over the 60-second interval [49].

In this thesis some ionospheric scintillation parameters obtained by processing the raw GPS signal are shown and compared with the data processed by commercial Septentrio PolaRxS receiver. The data presented here was collected at block S2.1 on 3th of June 2013, 16.33 – 16.43 LT (time of week around 117200 – 117800).

Figure 5-6 shows the signal intensity (SI) of satellites PRN 23 obtained from Septentrio PolaRxS receiver (top subfigure) and NI PXI raw signal (bottom subfigure). The *x*-axis is time of week (TOW) of GPS in second. TOW is started every Sunday at 12 a.m. and is reset every week. The *y*-axis represents the signal intensity of the signal with arbitrary unit. The trend, which is obtained by passing the SI through low pass filter, is also plotted. It can be seen clearly that the SI from NI PXI shows the same

trend as those from Septentrio. Some dips are seen in the NI PXI data due to saturation in the analog to digital converter.

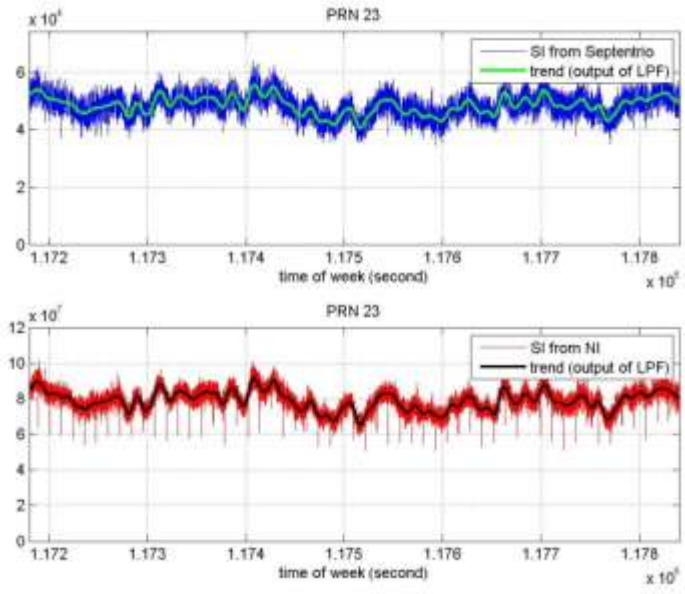

Figure 5-6 Signal Intensity from Septentrio and NI PXI raw signal PRN 23

S4 is calculated from SI by equation (2.1). Figure 5-7 show the amplitude scintillation (S4) of satellites PRN 23 obtained from Septentrio PolaRxS receiver and NI PXI raw signal. The *x*-axis is time of week (TOW) of GPS in second and the *y*-axis is S4. S4 obtained from processed NI PXI raw signal is very close to Septentrio PolaRxS output.

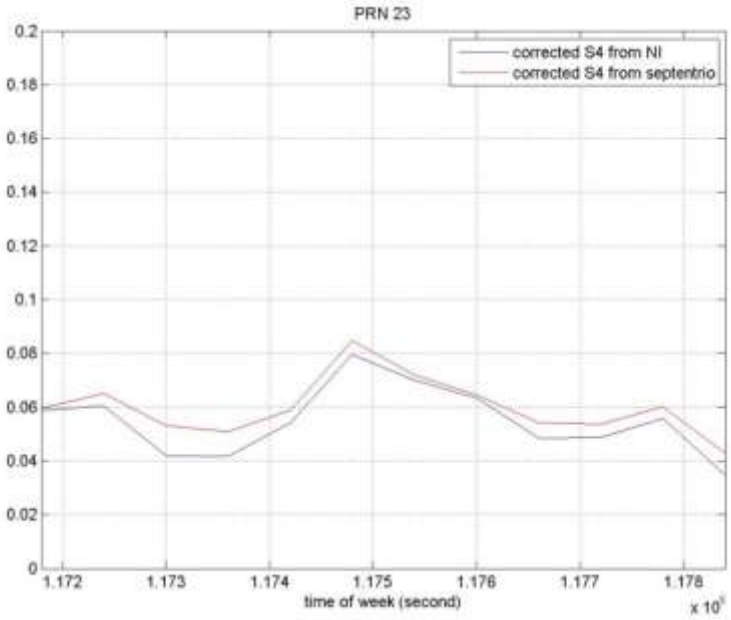

Figure 5-7 S4 from Septentrio and NI PXI raw signal PRN 23

C/N_0 is an indication of signal quality. It is also needed for S4 computation for removing its noise component. Reference [29] shows the following formula to obtain C/N_0:

$$NP_k = \frac{NBP_k}{WBP_k} \quad \textbf{(5.4)}$$

$$\hat{\mu}_{NP} = \frac{1}{K}\sum_{k=1}^{K} NP_k \quad \textbf{(5.5)}$$

$$C/N_0 = 10\log\left(\frac{1}{T}\frac{\hat{\mu}_{NP}-1}{M-\hat{\mu}_{NP}}\right) \quad \textbf{(5.6)}$$

where WBP and NBP are the wideband and narrowband signal power measurements obtained by (5.2) and (5.3), respectively, and T is the correlator integration time. In this work, we uses T=1 ms, M=20, and K=50.

Figure 5-8 shows the carrier to noise ratio (C/N_0) of satellite PRN 23 obtained from Septentrio receiver and NI PXI raw signal. The *x*-axis is time of week (TOW) of GPS in second and the *y*-axis is C/N_0 in dB. C/N_0 obtained from processed NI PXI raw signal is very close to Septentrio output.

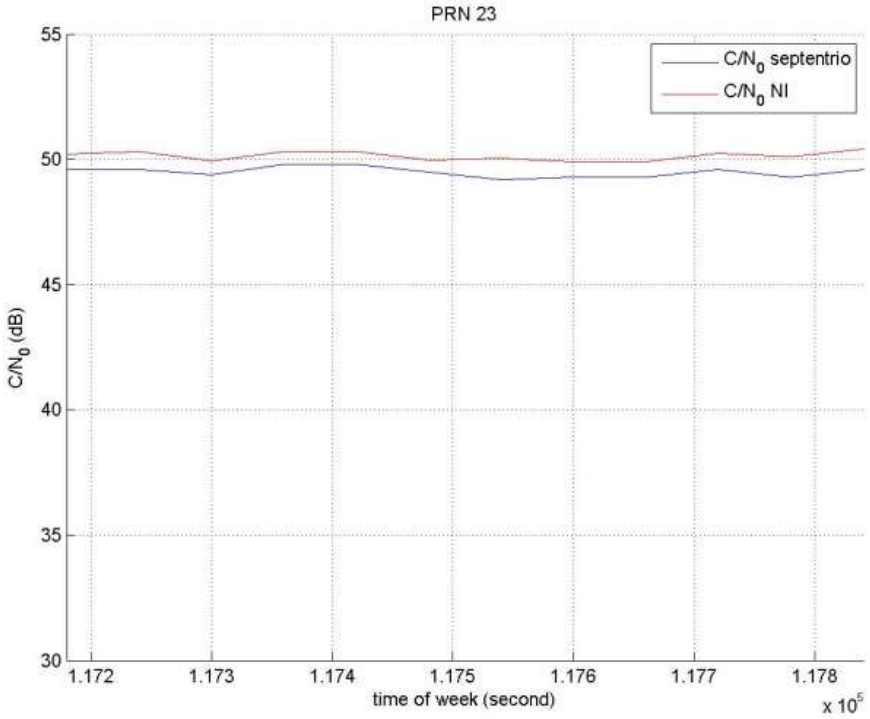

Figure 5-8 C/N0 from Septentrio and NI PXI raw signal PRN 23

5.2. Event Triggered Raw Baseband GPS Signal Recording

Collection of continuous raw baseband/IF samples is difficult to accomplish because of the large amount of data involved. Data collection with NI PXI with 3.125MHz complex sampling rate and 16-bit resolution ADC generates 12.5MB per second or 45GB data per hour. To study scintillation effect on wideband signals such GPS L1-P(Y) and GLONASS signals, this rate will go up by a factor of 10. Therefore, it is important to have a smart data collection system that will only record data when there is scintillation activity. Several works about event driven raw GPS data collection and processing have been done by some researchers [66][67] [68] [69].

In this section, an event triggered raw GPS signal recording section proposed by author for application using Septentrio receiver and NI PXI equipment is presented. Figure 5-9 shows the overall flow chart of the system. It consists of three main parts: RxLogger (by Septentrio) to log SBF file from receiver which is automatically followed by sbf2ismr.exe to calculate S4 which is contained inside ismr file. Next, a Matlab program is used to detect high S4 value and create a trigger file, and lastly labview program to detect the created trigger file and start recording the raw signal using NI PXI.

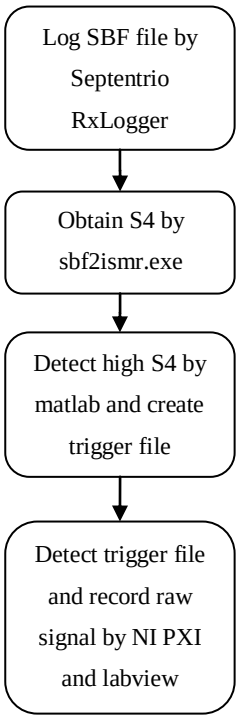

Figure 5-9 Overall event triggered flow chart

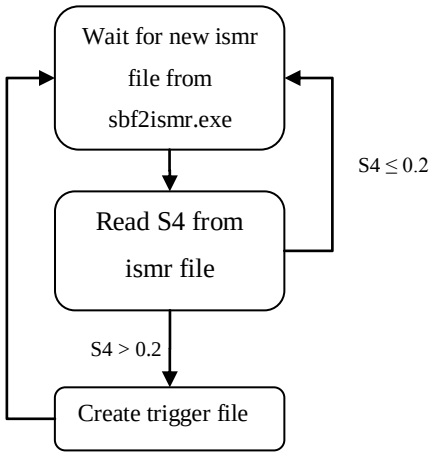

Figure 5-10 Matlab program flow chart

Figure 5-10 shows the Matlab program flow chart in detail (3rd stage in Figure 5-9). It continuously waits for new ismr file to read the S4 value. Once the S4 value is found to be larger than 0.2, the program will generate a trigger file.

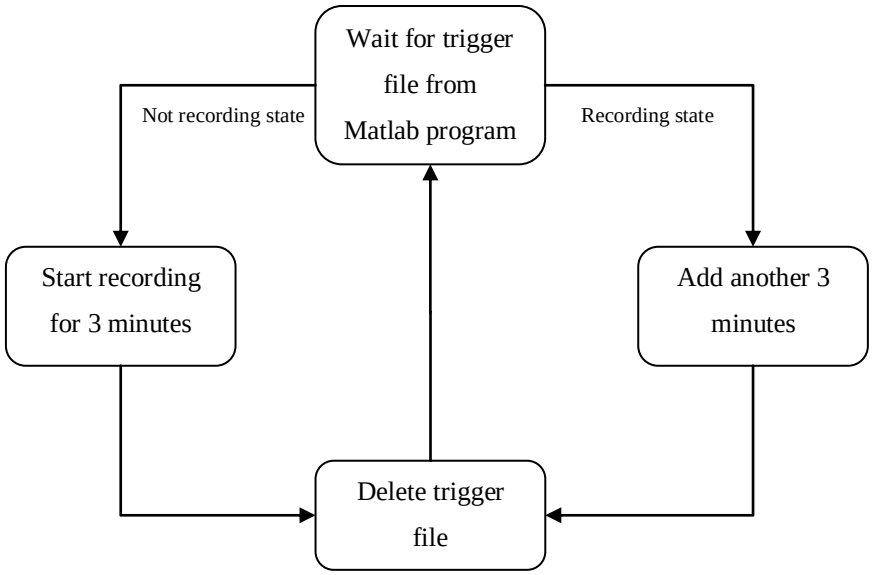

Figure 5-11 Labview program flow chart

Figure 5-11 shows the Labview program flow chart in detail (4th stage in Figure 5-9). It continuously waits for trigger file from the previous Matlab program. If trigger file is detected, the recording will start for duration of 3 minutes. If the NI PXI is already in a recording state, another 3 minutes will be added to the recording time.

Raw GPS signal during ionospheric scintillation has been collected during October 2013, March 2014, and April 2014. Temporarily, antenna is located on the rooftop of S2 building. It is connected with 30 meter long coaxial cable to the laboratory room in level B4 of block S2 where the Septentrio PolaRxS receiver and NI PXI equipments are located. This raw signal will be further processed and investigated.

6. Conclusions and Recommendations

6.1. Conclusions

This thesis has presented the results of GNSS ionospheric scintillation studies in Singapore. Ionospheric scintillation receiver monitoring system has been set up at three locations in NTU: block S2, S2.1, and Nanyang House. Continuous data logging is done by these receivers to collect the ionospheric scintillation information over Singapore. Data from the International GNSS Service (IGS) particularly NTUS station is also used for long term observation and comparison.

Monthly S4 mean obtained from GPS signal during 2013 has been presented. This analysis shows that high ionospheric scintillation happens during equinox months around April and September which is attributed to the close alignment of the solar terminator with magnetic meridian. Ionospheric scintillation happens mostly at night between 8pm to 12am. This is due to the eastward prereversal enhancement (PRE) electric field, which is coupled with the earth's geomagnetic field to produce an upward vertical force derived from $\boldsymbol{E \times B}$. The upward vertical force results in steep gradient of ion and electron densities between upper and lower layer, thereby producing plasma bubble irregularities arising from Rayleigh-Taylor instability process.

Further analysis of selected scintillation events during the equinox months has been done by presenting several selected scintillation events. S4, phio60, and ROTI are shown to occur concurrently. This indicates that both signal intensity and the carrier phase of the GPS signal exhibit fluctuations while propagating through the plasma bubble irregularities of the ionosphere layer during this period.

To study the probability of losing positioning solution due to ionospheric scintillation causing satellites unavailability, the histogram of satellites suffering from scintillation has been presented. It has been shown that the percentage of four or more satellites affected by scintillation is relatively low, less than four percent during equinox months. This result suggests that the probability of GPS receiver unable to get position due to ionospheric scintillation is relatively low.

The spatial correlation of ionospheric scintillation has been analyzed by comparing the logged data at three locations in NTU. Results show a very close scintillation correlation among the 3 receivers, even though the furthest distance is at 1 km apart. This suggests that the plasma irregularities within the ionosphere during the scintillation events are in larger scales of more than 1 km. To analyze further, the signal intensity and carrier phase are then used for cross correlation calculation between those three locations. Significant time lag is obtained between Nanyang House (NH) receiver with those in S2 and S2.1. This concludes that the irregularity bubbles during scintillation drift toward east direction.

We have analyzed the spatial distribution of scintillation occurrences by using sky plot based on the longitude and latitude. Higher scintillation is observed in the south part of the observed ionosphere due to the fact that the crest of EIA is located in the south of Singapore. Scintillation is also higher in the west compared to the east part because generally plasma bubbles are tilted westward as they vertically develop, which is due to vertical shear in the eastward plasma drift in the F region.

High solar activity has been proven to be a factor to increase ionospheric scintillation possibility. Sunspot number and solar radio flux as an indicator of solar activity shows high correlation with S4 in long term during year 2009-2013. However, in daily basis observation, there is no apparent correlation between solar activity and scintillation although high correlation with TEC is shown. This is due to the fact that there are other factors that affect the triggering of scintillation such as geomagnetic activity and also the randomness factor of the ionosphere irregularities initiation.

The effect of geomagnetic activity into ionospheric activity has been studied. It is observed that generally geomagnetic disturbances suppress the occurrence of scintillation activity. During geomagnetic disturbed days, dynamo electric fields opposing the normal ionospheric electric field are generated. This phenomena cause reduction in the post-sunset rise of the F-layer plasma in equatorial region which consequently, reducing the probability of scintillation occurrences. The study of the effect of scintillation on positioning accuracy has been done. It is shown that the pseudorange fluctuation is proportional to S4.

The utilization of GLONASS and BeiDou has been presented here. The scintillation parameters obtained from GLONASS and BeiDou are compared with those from GPS. This comparison shows high correlation coefficients between those different satellite constellations. The usage of L2 frequency of GNSS is also performed which concludes that S4 and phi60 in L2 frequency is consistently higher than those in L1. This indicates that ionospheric scintillation is inversely proportional to signal frequency.

For closer analysis, raw GPS signal has been collected using event triggered method. To effectively obtain useful raw signal, the system will record raw signal only when high S4 detected. Matlab program has been used to process the raw signal to obtain various ionospheric scintillation parameters such as signal intensity, C/N_0, and S4.

6.2. Recommendations for Further Research

More comprehensive study on the effect of ionospheric scintillation to GNSS receiver positioning can be done in the future work. The relation of S4, phi60, or ROTI with the deviation of receiver positioning can be further quantified. The receiver performance on the loss of lock during such disturbance can also be analyzed.

To further analyze the ionospheric scintillation spatial behavior, another monitoring station can be installed in east part of Singapore few kilo meters away from NTU. This will give wider coverage for the observed ionosphere over Singapore. An early work done in Hong Kong showed that 24 km distance can give better observable variation on the scintillation [70]. Another scintillation data source such as GNSS radio occultation can also be used to do more extensive study. Some work using GPS occultation has been done in China [23] and [22] which can be applied in Singapore by utilizing GLONASS and BeiDou also.

Further research can be done on the raw GPS recorded signal to observe the effect of ionosphere scintillation more directly on the RF signal. This smart data collection method can also be extended to GLONASS and BeiDou including L1 and L2 frequencies. This recorded signal can also be used as input to design more robust receiver instead of using simulation signal.

Work can be done to design more robust GNSS receiver that can track during ionosphere scintillation. Design on tracking loop that can adapt to the quality of the signal to maintain the lock is a possible method to solve this challenge. Another possible way is to design better antenna. Reference [71] and [72] show some work to deal with this scintillation problem. This can be applied for other problems also such as multipath effect in urban area and indoor navigation solution which always are potential challenges to do research on. Some works that has been done on mitigating such adverse effects are [73] and [74].

References

[1] M. C. Kelley, The Earth's Ionosphere: Plasma Physics & Electrodynamics, Academic Press, 2009.

[2] T. Walter, "Walter_Briefing_Sept_2008.ppt," 11 September 2008. [Online]. Available: www.ion.org/sections/southcalifornia/Walter_Briefing_Sept_2008.ppt. [Accessed 27 March 2013].

[3] J. A. Klobuchar, "Ionosphere Effect on GPS," in *Global Positioning System: Theory and Applications, Volume 1*, American Institute of Aeronautics and Astronautics, 1996, pp. 485-516.

[4] M. Kelley, The Earth's Ionosphere, London: Academic Press, 1989.

[5] M. Abdu, "Equatorial ionosphere–thermosphere system: Electrodynamics and irregularities," *Advances in Space Research,* vol. 35, no. 5, p. 771–787, 2005.

[6] R. Duncan, "The equatorial F-region of the ionosphere," *Journal of Atmospheric and Terrestrial Physics,* vol. 18, no. 2-3, pp. 89-100, 1960.

[7] "Navipedia: GNSS FUndamental," 1 November 2011. [Online]. Available: http://navipedia.net/index.php/Category:Fundamentals.

[8] "Interface Specification IS-GPS-200," Global Positioning System Directorate System Engineering and Integration, 2013.

[9] "Navipedia :GLONASS," 1 2011. [Online]. Available: http://navipedia.net/index.php/Category:GLONASS.

[10] "GLONASS Interface Control Document," COORDINATION SCIENTIFIC INFORMATION CENTER, Moscow, 1998.

[11] "European GNSS (Galileo) Open Service Signal In Space Interface Control

Document," European Union , 2010.

[12] C. Chong, "Status of COMPASS/BeiDou," 22 October 2009. [Online]. Available: http://scpnt.stanford.edu/pnt/PNT09/presentation_slides/3_Cao_Beidou_Status.pdf.

[13] "BeiDou Navigation Satellite System," China Satellite Navigation Office, 2013.

[14] J. J. S. Jr., "GPS Signal Structure and Theoritical Performance," in *Global Positioning System: Theory and Applications Volume 1*, Washington, DC, American Institute of Aeronautics and Astronautics, 1996, pp. 57-120.

[15] C. H. Elliott D. Kaplan, Understanding GPS: Principles and Applications, Artech House, 2005.

[16] A. El-Rabbany, Introduction to GPS: The Global Positioning System, Artech House, 2006.

[17] Tsui, Fundamentals of Global Positioning System Receivers: A Software Approach, Wiley, 2005.

[18] B. L. H. C. J. Hofmann-Wellenhof, Global Positioning System Theory and Practice, New York: Springer-Verlag Wien, 2001 .

[19] "GPS signals," Wikipedia, [Online]. Available: http://en.wikipedia.org/wiki/GPS_signals. [Accessed August 2014].

[20] A. J. Dierendonck, J. Klobuchar and Q. Hua, "Ionospheric Scintillation Monitoring Using Commercial Single Frequency C/A Code Receivers," in *ION GPS-93*, Salt Lake City, 1993.

[21] A. Seif, M. Abdullaha, A. M. Hasbia and Y. Zou, "Investigation of ionospheric scintillation at UKM station, Malaysia during low solar activity," *Acta Astronautica*, vol. 81, no. 1, p. 92–101, 2012.

[22] Y. Zou and D. Wang, "A study of GPS ionospheric scintillations observed at Guilin," *Journal of Atmospheric and Solar-Terrestrial Physics,* vol. 71, no. 17–18, p. 1948–1958, 2009.

[23] Y. Zou, "Ionospheric scintillations at Guilin detected by GPS ground-based and radio occultation observations," *Advances in Space Research,* vol. 47, no. 6, p. 945–965, 2011.

[24] A. J. Mannucci, B. D. Wilson and C. D. Edwards, "A New Method for Monitoring the Earth's Ionospheric Total Electron Content Using the GPS Global Network," in *Proceedings of the 6th International Technical Meeting of the Satellite Division of The Institute of Navigation*, Salt Lake City, 1993.

[25] X. Pi, A. J. Mannucci, U. J. Lindqwister and C. M. Ho, "Monitoring of global ionospheric irregularities," *Geophysical Research Letters,* vol. 24, no. 18, pp. 2283-2286, 1997.

[26] S. Basu, K. Groves, J. Quinn and P. Doherty, "A comparison of TEC Fuctuations and scintillations at Ascension Island," *Journal of Atmospheric and Solar-Terrestrial Physics,* vol. 61, p. 1219±1226, 1999.

[27] A. J. V. Dierendonck, Q. Hua, P. Fenton and J. Klobuchar, "Commercial Ionospheric Scintillation Monitoring Receiver Development and Test Results," in *Proceedings of the 52nd Annual Meeting of The Institute of Navigation*, Cambridge, 1996.

[28] J.-M. S. L. S. S. V. V. J. G. M. B. Bougard, "CIGALA: Challenging the Solar Maximum in Brazil with PolaRxS," in *Proceedings of the 24th International Technical Meeting of The Satellite Division of the Institute of Navigation*, Portland, Oregon, 2011.

[29] S. Peng and Y. Morton, "A USRP2-Based Multi-Constellation and Multi-Frequency GNSS Software Receiver for Ionosphere Scintillation Studies," in *Proceedings of the 2011 International Technical Meeting of The Institute of Navigation*, San Diego, CA, 2011.

[30] A. Gwal, S. Dubey, R. Wahi and A. Feliziani, "Amplitude and phase scintillation study at Chiang Rai, Thailand," *Advances in Space Research,* vol. 38, no. 11, p. 2361–2365, 2006.

[31] P. Theerapatpaiboon, P. Supnithi, N. Leelaruji and N. Hemmakorn, "The Analysis of Ionospheric Scintillation on the Global Positioning System (GPS) at Bangkok," in *SICE-ICASE International Joint Conference,* Busan, Korea, 2006.

[32] P. Abadi, S. Saito and W. Srigutomo, "Low-latitude scintillation occurrences around the equatorial anomaly crest over Indonesia," *Annales Geophysicae,* vol. 32, no. 1, pp. 7-17, 2014.

[33] P. V. S. R. Rao, S. G. Krishna, K. Niranjan and D. S. V. V. D. Prasad, "Study of spatial and temporal characteristics of L-band scintillations over the Indian low-latitude region and their possible effects on GPS navigation," *Annales Geophysicae,* vol. 24, pp. 1567-1580, 2006.

[34] M. T. A. H. Muella, E. R. d. Paula and A. A. Monteiro, "Ionospheric Scintillation and Dynamics of Fresnel-Scale Irregularities in the Inner Region of the Equatorial Ionization Anomaly," *Surveys in Geophysics,* vol. 34, no. 2, pp. 233-251, 2013.

[35] L. Spogli, L. Alfonsi, G. de Franceschi, V. Romano, M. H. O. Aquino and A. Dodson, "Climatology of GPS ionospheric scintillations over high and mid-latitude European regions," *Annales Geophysicae,* vol. 27, no. 9, pp. 3429-3437, 2009.

[36] V. Sreeja and M. Aquino, "Statistics of ionospheric scintillation occurrence over European high latitudes," *Journal of Atmospheric and Solar-Terrestrial Physics,* vol. 120, p. 96–101, 2014.

[37] L. Alfonsi, L. Spogli, G. D. Franceschi, V. Romano, M. Aquino, A. Dodson and C. N. Mitchell, "Bipolar climatology of GPS ionospheric scintillation at solar minimum," *Radio Science,* vol. 46, no. 3, 2011.

[38] *SBF Reference Guide,* Leuven, Belgium: Septentrio Satellite Navigation, 2010.

[39] *PolaRxS Application Manual,* Leuven, Belgium: Septentrio Satellite Navigation, 2010.

[40] "Transformation of Coordinate Geographic <=> Geomagnetic (IGRF-11)," World Data Center for Geomagnetism, Kyoto, [Online]. Available: http://wdc.kugi.kyoto-u.ac.jp/igrf/gggm/.

[41] S. P. P. T. R. G. A. Bhattacharya, "Study of GPS based ionospheric scintillation and its effects on dual frequency receiver," *Journal of Engineering, Science and Management Education,* vol. 1, pp. 55-61, 2010.

[42] S. K. K. P. H.J. Tanna, "A study of L band scintillations during the initial phase of rising solar activity at an Indian low latitude station," *Advances in Space Research,* vol. 52, no. 3, p. 412–421, 2013.

[43] B. Forte and S. M. Radicella, "Problems in data treatment for ionospheric scintillation measurements," *RADIO SCIENCE,* vol. 37, no. 6, pp. 8-1–8-5, 2002.

[44] G. Ma and T. Maruyama, "A super bubble detected by dense GPS network at east Asian longitudes," *Geophys. Res. Lett.,* vol. 33, no. 21, 2006.

[45] J. S. Xu, J. Zhu and L. Li, "Effects of a major storm on GPS amplitude scintillations and phase fluctuations at Wuhan in China," *Advances in Space Research,* vol. 39, no. 8, p. 1318–1324, 2007.

[46] B. G. Fejer, E. R. d. Paula, S. A. González and R. F. Woodman, "Average vertical and zonal F region plasma drifts over Jicamarca," *Journal of Geophysical Research: Space Physics,* vol. 96, no. A8, p. 13901–13906, 1991.

[47] B. G. Fejer, D. T. Farley, C. A. Gonzales, R. F. Woodman and C. Calderon, "F region east-west drifts at Jicamarca," *Journal of Geophysical Research: Space Physics* , vol. 86, no. A1, p. 215–218, 1981.

[48] B. M. Air Force Cambridge Research Laboratories, J. Aarons, H. Whitney and R. Allen, "Global morphology of ionospheric scintillations," in *Proceedings of the IEEE* , 1971.

[49] A. J. V. Dierendonck and B. Arbesser-Rastburg, "Measuring Ionospheric Scintillation in the Equatorial Region Over Africa, Including Measurements From SBAS Geostationary Satellite Signals," in *Proceedings of the 17th International Technical Meeting of the Satellite Division of The Institute of Navigation (ION GNSS 2004)*, Long Beach, CA, 2004.

[50] V. Romano, L. Spogli, M. Aquino, A. Dodson, C. Hancock and B. Fortec, "GNSS station characterisation for ionospheric scintillation applications," *Advances in Space Research*, vol. 52, no. 7, p. 1237–1246, 2013.

[51] S. Basu, E. MacKenzie and S. Basu, "Ionospheric constraints on VHF-UHF communications links during solar maximum and minimum periods," *Radio Science*, vol. 23, no. 3, p. 363–378, 1988.

[52] S. T. Zalesak, S. L. Ossakow and P. K. Chaturvedi, "Nonlinear equatorial spread F: The effect of neutral winds and background Pedersen conductivity," *Journal of Geophysical Research: Space Physics* , vol. 87, no. A1, p. 151–166, 1982.

[53] P. A. Bernhardt, "Quasi-analytic models for density bubbles and plasma clouds in the equatorial ionosphere: 2. A simple Lagrangian transport model," *Journal of Geophysical Research*, vol. 112, no. A11, 2007.

[54] B. H. Briggs and I. A. Parkin, "On the variation of radio star and satellite scintillations with zenith angle," *Journal of Atmospheric and Terrestrial Physics*, vol. 25, no. 6, pp. 339-366, 1963.

[55] National Geophysical Data Center, "Readme: Sunspot Numbers," 1 September 2013. [Online]. Available: http://www.ngdc.noaa.gov/stp/space-weather/solar-data/solar-indices/sunspot-numbers/documentation/readme_sunspot-numbers.pdf. [Accessed 2014].

[56] B. H. Briggs, "Observations of radio star scintillations and spread-F echoes over a solar cycle," *Journal of Atmospheric and Terrestrial Physics,* vol. 26, no. 1, pp. 1-23, 1964.

[57] S. Alex and R. Rastogi, "Geomagnetic disturbance effects on equatorial spread F," *Ann. Geophys.* , vol. 5, p. 83–88, 1987.

[58] B. Mathew, B. M. Pathan, K. N. Iyer and D. R. K. Rao, "Comparative study of scintillations at the magnetic equator and at the crest region of the equatorial anomaly in Indian zone," in *Proceedings of the Indian Academy of Sciences - Earth and Planetary Sciences*, 1991.

[59] B. D. Wilson and A. J. Mannucci, "Instrumental Biases in Ionospheric Measurements Derived from GPS Data," in *Proceedings of the 6th International Technical Meeting of the Satellite Division of The Institute of Navigation (ION GPS 1993)*, Salt Lake, 1993.

[60] E. Sardón, A. Rius and N. Zarraoa, "Estimation of the transmitter and receiver differential biases and the ionospheric total electron content from Global Positioning System observations," *Radio Science,* vol. 29, no. 3, p. 577–586, 1994.

[61] A. J. Mannucci, B. D. Wilson and C. D. Edwards, "A New Method for Monitoring the Earth's Ionospheric Total Electron Content Using the GPS Global Network," in *Proceedings of the 6th International Technical Meeting of the Satellite Division of The Institute of Navigation (ION GPS 1993)*, Salt Lake, 1993.

[62] B. Choi, J. Cho and S. Lee, "Estimation and analysis of GPS receiver differential code biases using KGN in Korean Peninsula," *Advances in Space Research,* vol. 47, no. 9, p. 1590–1599, 2011.

[63] E. J. Fremouw, R. L. Leadabrand, R. C. Livingston, M. D. Cousins, C. L. Rino, B. C. Fair and R. A. Long, "Early results from the DNA Wideband satellite experiment—Complex-signal scintillation," *Radio Science,* vol. 13, no. 1, p.

167–187, 1978.

[64] K. Borre, D. M. Akos, N. Bertelsen, P. Rinder and S. H. Jensen, A Software Defined GPS and Galileo Receiver, New York: Birkhauser Boston, 2007.

[65] E. J. Fremouw, R. L. Leadabrand, R. C. Livingston, M. D. Cousins, C. L. Rino, B. C. Fair and R. A. Long, "Early results from the DNA Wideband satellite experiment—Complex-signal scintillation," *Radio Science,* vol. 13, no. 1, p. 167–187, 1978.

[66] Y. M. W. P. Praveen Vikram, "An Event Driven GPS Data Collection System for Studying Ionospheric Scintillation," in *Proceedings of the 24th International Technical Meeting of The Satellite Division of the Institute of Navigation*, Portland, Oregon, 2011.

[67] Y. M. Senlin Peng, "A USRP2-based reconfigurable multi-constellation multi-frequency GNSS software receiver front end," *GPS Solutions* , vol. 17, no. 1, pp. 89-102 , 2013.

[68] V. Praveen, "Event driven gps data collection system for studying ionospheric scintillation," Miami University, Ohio, 2011.

[69] Y. M. Y. J. J. T. W. P. S. Taylor, "An Improved Ionosphere Scintillation Event Detection and Automatic Trigger for GNSS Data Collection Systems," in *Proceedings of the 2012 International Technical Meeting of The Institute of Navigation*, Newport Beach, CA, 2012.

[70] Z. Liu, R. Xu, J. Morton, J. Xu, W. Pelgrum, S. Taylor, W. Chen and X. Ding, "A Comparison of GNSS-based Ionospheric Scintillation Observations in North and South Hong Kong," in *Proceedings of the ION 2013 Pacific PNT Meeting*, Honolulu, Hawaii, 694 - 705.

[71] S. Peng, Y. Morton and R. Di, "A multiple-frequency GPS software receiver design based on a Vector tracking loop," in *Position Location and Navigation Symposium (PLANS), 2012 IEEE/ION*, Myrtle Beach, SC, 2012.

[72] S. Ganguly, A. Jovancevic, A. Brown, M. Kirchner and S. Zigic, "Ionospheric scintillation monitoring and mitigation using a software GPS receiver," *Radio Science*, vol. 39, no. 1, 2004.

[73] M. Brenneman, J. Morton, C. Yang and F. v. Graas, "Mitigation of GPS Multipath Using Polarization and Spatial Diversities," in *Proceedings of the 20th International Technical Meeting of the Satellite Division of The Institute of Navigation (ION GNSS 2007)*, Fort Worth, TX, 2007.

[74] D. Aloi and F. Van Graas, "Ground-multi path mitigation via polarization steering of GPS signal," *Aerospace and Electronic Systems, IEEE Transactions*, vol. 40, no. 2, pp. 536 - 552, 2004.

[75] S. Peng, "A Multi-constellation Multi-Frequency GNSS Software," Virginia Polytechnic Institute and State University, Virginia, 2012.

[76] W. Pelgrum, J. Morton, F. v. Graas, S. Gunawardena, M. Bakich, D. Chemey, S. Peng, J. Triplett, A. Vermuru and P. Vikram, "Measurement and Analysis of Artificially-Generated and Natural Ionosphere Scintillations Effects on GNSS Signals," 2011.

[77] "Real-time (Quicklook) Dst index," World Data Center for Geomagnetism, 2014. [Online]. Available: http://wdc.kugi.kyoto-u.ac.jp/dst_realtime/.